

REPORT DOCUMENTATION PAGE			Form Approved OMB NO. 0704-0188		
<p>The public reporting burden for this collection of information is estimated to average 1 hour per response, including the time for reviewing instructions, searching existing data sources, gathering and maintaining the data needed, and completing and reviewing the collection of information. Send comments regarding this burden estimate or any other aspect of this collection of information, including suggestions for reducing this burden, to Washington Headquarters Services, Directorate for Information Operations and Reports, 1215 Jefferson Davis Highway, Suite 1204, Arlington VA, 22202-4302. Respondents should be aware that notwithstanding any other provision of law, no person shall be subject to any penalty for failing to comply with a collection of information if it does not display a currently valid OMB control number.</p> <p>PLEASE DO NOT RETURN YOUR FORM TO THE ABOVE ADDRESS.</p>					
1. REPORT DATE (DD-MM-YYYY) 03-05-2011		2. REPORT TYPE Final Report		3. DATES COVERED (From - To) 1-Aug-2004 - 31-Jul-2008	
4. TITLE AND SUBTITLE Final Report for Eolian Modeling System (EMS): Predicting Windblown Sand and Dust Hazards in Battlefield Environments			5a. CONTRACT NUMBER W911NF-04-1-0266		
			5b. GRANT NUMBER		
			5c. PROGRAM ELEMENT NUMBER 611102		
6. AUTHORS Jon D. Pelletier			5d. PROJECT NUMBER		
			5e. TASK NUMBER		
			5f. WORK UNIT NUMBER		
7. PERFORMING ORGANIZATION NAMES AND ADDRESSES University of Arizona Sponsored Project Services PO Box 3308 Tucson, AZ 85722 -3308			8. PERFORMING ORGANIZATION REPORT NUMBER		
9. SPONSORING/MONITORING AGENCY NAME(S) AND ADDRESS(ES) U.S. Army Research Office P.O. Box 12211 Research Triangle Park, NC 27709-2211			10. SPONSOR/MONITOR'S ACRONYM(S) ARO		
			11. SPONSOR/MONITOR'S REPORT NUMBER(S) 45628-EV.1		
12. DISTRIBUTION AVAILABILITY STATEMENT Approved for Public Release; Distribution Unlimited					
13. SUPPLEMENTARY NOTES The views, opinions and/or findings contained in this report are those of the author(s) and should not be construed as an official Department of the Army position, policy or decision, unless so designated by other documentation.					
14. ABSTRACT This final report describes activities performed as part of the ARO-funded project entitled "Eolian Modeling System (EMS): Predicting Windblown Sand and Dust Hazards in Battlefield Environments." The objectives of the research were to 1) develop numerical models for the atmospheric transport of windblown sand and dust and validate those models using thicknesses of dust deposits measured downwind of dust sources, 2) develop numerical models for the relationship between surface moisture and vegetation and the transport of sand and dust from					
15. SUBJECT TERMS terrain sciences, wind erosion, geomorphology					
16. SECURITY CLASSIFICATION OF:			17. LIMITATION OF ABSTRACT UU	15. NUMBER OF PAGES	19a. NAME OF RESPONSIBLE PERSON Jon Pelletier
a. REPORT UU	b. ABSTRACT UU	c. THIS PAGE UU			19b. TELEPHONE NUMBER 520-626-2126

Report Title

Final Report for Eolian Modeling System (EMS): Predicting Windblown Sand and Dust Hazards in Battlefield Environments

ABSTRACT

This final report describes activities performed as part of the ARO-funded project entitled "Eolian Modeling System (EMS): Predicting Windblown Sand and Dust Hazards in Battlefield Environments." The objectives of the research were to 1) develop numerical models for the atmospheric transport of windblown sand and dust and validate those models using thicknesses of dust deposits measured downwind of dust sources, 2) develop numerical models for the relationship between surface moisture and vegetation and the transport of sand and dust from surfaces. These models will be validated using field measurements collected by the U.S. Geological Survey, and 3) understand the climatic and meteorological conditions responsible for triggering windblown sand and dust events in study areas of the southwestern U.S.

List of papers submitted or published that acknowledge ARO support during this reporting period. List the papers, including journal references, in the following categories:

(a) Papers published in peer-reviewed journals (N/A for none)

Pelletier, J.D., H. Mitasova, R.S. Harmon, and M. Overton, The effects of interdune vegetation changes on eolian dune field evolution: A numerical-modeling case study at Jockey's Ridge, North Carolina, USA, Earth Surface Processes and Landforms, 34, 1245-1254, 2009.

Pelletier, J.D., Controls on the height and spacing of eolian ripples and transverse dunes: A numerical modeling investigation, Geomorphology, 105, 322-333, 2009.

Pelletier, J.D., M. Cline, and S. DeLong, Desert pavement dynamics: Numerical modeling and field-based calibration, Earth Surface Processes and Landforms, 32, 1913-1927, 2007.

Cook, J.P., and J.D. Pelletier, Relief threshold for eolian transport across alluvial fans, Journal of Geophysical Research, 112, F02026, doi:10.1029/2006JF000610, 2007.

Pelletier, J.D., A Cantor set model of eolian dust accumulation on desert alluvial fan terraces, Geology, 35, 439-442, 2007.

Pelletier, J.D., Sensitivity of playa windblown-dust emissions to climatic and anthropogenic change, Journal of Arid Environments, 66, 62-75, 2006.

Pelletier, J.D., and J.P. Cook, Deposition of playa windblown dust over geologic time scales, Geology, 33, 909-912, 2005.

Kohfield, K.E., R.L. Reynolds, J.D. Pelletier, and W. Nickling, Linking the scales of dust emissions: A workshop report, EOS, Transactions of the American Geophysical Union, 86, 113-114, 2005.

Number of Papers published in peer-reviewed journals: 8.00

(b) Papers published in non-peer-reviewed journals or in conference proceedings (N/A for none)

Number of Papers published in non peer-reviewed journals: 0.00

(c) Presentations

Number of Presentations: 0.00

Non Peer-Reviewed Conference Proceeding publications (other than abstracts):

Number of Non Peer-Reviewed Conference Proceeding publications (other than abstracts): 0

Peer-Reviewed Conference Proceeding publications (other than abstracts):

(d) Manuscripts

Cook, J.P., and J.D. Pelletier, Frequency-magnitude distribution of eolian transport and the geomorphically most-effective windstorm, submitted but not accepted to Geophysical Research Letters.

Number of Manuscripts:1.00

Patents Submitted

Patents Awarded

Awards

Graduate Students

<u>NAME</u>	<u>PERCENT SUPPORTED</u>
Joseph Cook	1.00
Stephen DeLong	0.20
Michael Cline	0.20
FTE Equivalent:	1.40
Total Number:	3

Names of Post Doctorates

<u>NAME</u>	<u>PERCENT SUPPORTED</u>
FTE Equivalent:	
Total Number:	

Names of Faculty Supported

<u>NAME</u>	<u>PERCENT SUPPORTED</u>	National Academy Member
Jon Pelletier	0.10	No
FTE Equivalent:	0.10	
Total Number:	1	

Names of Under Graduate students supported

<u>NAME</u>	<u>PERCENT SUPPORTED</u>
FTE Equivalent:	
Total Number:	

Student Metrics

This section only applies to graduating undergraduates supported by this agreement in this reporting period

The number of undergraduates funded by this agreement who graduated during this period: 0.00

The number of undergraduates funded by this agreement who graduated during this period with a degree in science, mathematics, engineering, or technology fields:..... 0.00

The number of undergraduates funded by your agreement who graduated during this period and will continue to pursue a graduate or Ph.D. degree in science, mathematics, engineering, or technology fields:..... 0.00

Number of graduating undergraduates who achieved a 3.5 GPA to 4.0 (4.0 max scale):..... 0.00

Number of graduating undergraduates funded by a DoD funded Center of Excellence grant for Education, Research and Engineering:..... 0.00

The number of undergraduates funded by your agreement who graduated during this period and intend to work for the Department of Defense 0.00

The number of undergraduates funded by your agreement who graduated during this period and will receive scholarships or fellowships for further studies in science, mathematics, engineering or technology fields: 0.00

Names of Personnel receiving masters degrees

NAME

Joseph Cook

Michael Cline (partial support from this gr

Total Number:

2

Names of personnel receiving PhDs

NAME

Stephen DeLong (partial support from this

Total Number:

1

Names of other research staff

NAME

PERCENT SUPPORTED

FTE Equivalent:

Total Number:

Sub Contractors (DD882)

Inventions (DD882)

Scientific Progress

This project made fundamental advances in our ability to model sand and dust transport in complex terrain over geologic time scales and compare those models to geologic records. The project made significant advances on our understanding of all components of the dust cycle in arid environments, including dust emission from playas and dust deposition on alluvial fans. Finally, the project made important progress in our understanding of eolian bedforms, including what controls their size and how they interact with vegetation.

Technology Transfer

Final Report

**Eolian Modeling System: Predicting windblown dust hazards in battlefield environments
Project Number 45628-EV**

Jon D. Pelletier
Geosciences Department
University of Arizona

Table of Contents

Summary of Completed Work	:	Pages 3-4
Appendices:		6-
Curriculum Vita for PI Jon D. Pelletier		
Published manuscripts		

Objectives

This project sought to quantify the transport and fate of wind-blown sand and dust in desert environments and to understand the implications of eolian transport for environmental processes such as soil and desert pavement formation. The primary aims of the project were to:

- Develop numerical models for the atmospheric transport of windblown sand and dust and validate those models using thicknesses of dust deposits measured downwind of dust sources.
- Develop numerical models for the relationship between surface moisture and vegetation and the transport of sand and dust from surfaces. These models will be validated using field measurements collected by the U.S. Geological Survey.
- Understand the climatic and meteorological conditions responsible for triggering windblown sand and dust events in study areas of the southwestern U.S.

Approach

Our approach used a combination of process-based numerical models, field measurement, and numerical data analysis to attain its objectives. The approaches are too varied to be properly summarized here. Please see the seven published papers reprinted in the Appendices.

Significance and Army Value

Windblown sand and dust presents several challenges to Army soldiers and equipment. Sand and dust may obscure visibility, cause equipment malfunction, and threaten the health of soldiers. In order for the Army to be fully prepared for ground campaigns in desert environments, tools for the assessment and prediction of blowing sand and dust are necessary. In the testing environment (e.g. Yuma Proving Ground), better modeling of blowing sand and dust conditions can enable testers to better evaluate equipment performance.

Our results are highly significant for the Army. For example, we developed a numerical model for the transport of sand in areas of complex terrain. Specifically, we documented a relationship between topographic relief and eolian transport across distal alluvial fans. These results can be used to predict trafficability. For example, distal alluvial fans that appear light in color on false-color LANDSAT imagery are associated with eolian causeways. These causeways are susceptible to saltation during high winds (which can impair trafficability), but have along-strike relief less than approximately 1 m (improving trafficability in the absence of saltation).

Technology Transfer

- No technology transfer was accomplished beyond annual briefings at Army Installations (Waterways Experiment Station and Ft. Carson, as hosted by the Program Manager).

Student Support

Funds supported the Master's Thesis of Joe Cook, portions of the theses of Stephen Delong and Michael Cline, and 1 month of summer support for the PI for each of the years of the project. The project also supported field-work expenses for multiple field trips totaling approximately 20 days.

Publications (in the Appendices)

Pelletier, J.D., H. Mitsova, R.S. Harmon, and M. Overton, The effects of interdune vegetation changes on eolian dune field evolution: A numerical-modeling case study at Jockey's Ridge, North Carolina, USA, *Earth Surface Processes and Landforms*, **34**, 1245-1254, 2009.

Pelletier, J.D., Controls on the height and spacing of eolian ripples and transverse dunes: A numerical modeling investigation, *Geomorphology*, **105**, 322-333, 2009.

- Pelletier, J.D., M. Cline, and S. DeLong, Desert pavement dynamics: Numerical modeling and field-based calibration, *Earth Surface Processes and Landforms*, **32**, 1913-1927, 2007.
- Cook, J.P., and J.D. Pelletier, Relief threshold for eolian transport across alluvial fans, *Journal of Geophysical Research*, **112**, F02026doi:10.1029/2006JF000610, 2007.
- Pelletier, J.D., A Cantor set model of eolian dust accumulation on desert alluvial fan terraces, *Geology*, **35**, 439-442, 2007.
- Pelletier, J.D., Sensitivity of playa windblown-dust emissions to climatic and anthropogenic change, *Journal of Arid Environments*, **66**, 62-75, 2006.
- Kohfield, K.E., R.L. Reynolds, J.D. Pelletier, and W. Nickling, Linking the scales of dust emissions: A workshop report, *EOS, Transactions of the American Geophysical Union*, **86**, 113-114, 2005.
- Pelletier, J.D., and J.P. Cook, Deposition of playa windblown dust over geologic time scales, *Geology*, **33**, 909-912, 2005.

Appendix

Curriculum Vita for Jon D. Pelletier

Current Address

Geosciences Department, 1040 E. Fourth St., Tucson, AZ 85721

Phone: 520-626-2126; Fax: 520-621-2672

Electronic Mail: jdpellet@email.arizona.edu

Education

1997 Ph.D., Geological Sciences, Cornell University, Ithaca, NY

Research advisor: Donald L. Turcotte

1992 B.S. with honors, Physics, California Institute of Technology, Pasadena, CA

Research advisor: Thomas A. Tombrello

Employment

2010-present Professor, Geosciences Department, University of Arizona

2005-2010 Associate Professor, Geosciences Department, University of Arizona

1999-2005 Assistant Professor, Geosciences Department, University of Arizona

1997-1999 O.K. Earl Prize Postdoctoral Scholar, California Institute of Technology

1995-1997 Graduate Research Assistant, Geosciences Department, Cornell University

1993-1995 Graduate Teaching Assistant, Physics Department, Cornell University

1992-1993 Research Scientist, Nuclear Physics Department, Schlumberger-Doll Research

Additional Professional Activities and Affiliations

2008-present Coeditor, GSA journal *Lithosphere*

2007-present Adjunct faculty member, Planetary Sciences Department, University of Arizona.

2004-2007 Consulting geomorphologist, Yucca Mountain Project, Department of Energy.

2002-present Affiliate faculty member, Applied Mathematics Program, University of Arizona

2001-present Affiliate faculty member, Institute for the Study of Planet Earth, University of Arizona

Honors/Awards

O.K. Earl Prize Postdoctoral Scholar, California Institute of Technology, 1997-1999

Texaco Graduate Fellowship, Geosciences Department, Cornell University, 1995

Chevron Graduate Fellowship, Geosciences Department, Cornell University, 1996

Green Prize for Undergraduate Research, Physics Department, Caltech, 1992

Barry M. Goldwater Scholarship, 1990-1992

Caltech Merit Scholarship, 1990-1992

Books

Pelletier, J.D., *Quantitative Modeling of Earth Surface Processes*, Cambridge University Press, 2008.

Publications (published and accepted for publication)

Pelletier, J.D., *Fundamental Principles and Techniques of Landform Evolution Modelling*, in Schroder, J., ed., *Treatise on Geomorphology*, Elsevier.

DeLong, S.B., L.J. Arnold, and J.D. Pelletier, Late Holocene alluvial history of the Cuyama River, California, USA, *Geological Society of America Bulletin*.

- Pelletier, J.D., Fluvial and slope-wash erosion of soil-mantled landscapes: detachment- or transport-limited? *Earth Surface Processes and Landforms*.
- Pelletier, J.D., J. Quade, R.J. Goble, and M.S. Aldenderfer, Widespread hillslope gullying on the southeastern Tibetan Plateau: Human or climate-change induced? *Geological Society of America Bulletin*.
- Kapp, P., J.D. Pelletier, A Rohrmann, R. Heermance, and J. Russell, Wind erosion in the Qaidam Basin, central Asia: Implications for tectonics, paleoclimate, and the source of the Loess Plateau, *GSA Today*, **21**, 4-10, 2011.
- Rasmussen, C., P. Brooks, J. Chorover, T. Huxman, P.A. Troch, and J.D. Pelletier, An open system framework for integrating critical zone structure and function, *Biogeochemistry*, **102**, 15-29.
- Pelletier, J.D., How do pediments form? A numerical modeling investigation with comparison to pediments in southern Arizona, USA, *Geological Society of America Bulletin*, **122**, 1815-1829, 2010.
- Pelletier, J.D., Minimizing the grid-resolution dependence of flow-routing algorithms for geomorphic applications, *Geomorphology*, **122**, 91-98, 2010.
- Kolb, K.J., A.S. McEwen, and J.D. Pelletier, Investigating gully flow emplacement mechanisms using apex slopes, *Icarus*, **208**, 132-142, 2010.
- Pelletier, J.D., Numerical modeling of the late Cenozoic geomorphic evolution of Grand Canyon, Arizona, *Geological Society of America Bulletin*, **122**, 595-608, 2010.
- Kolb, K.J., J.D. Pelletier, and A.S. McEwen, Modeling the formation of bright slope deposits associated with gullies in Hale Crater, Mars: Implications for recent liquid water, *Icarus*, **205**, 113-137, 2010.
- Pelletier, J.D., D. Comeau, and J. Kargel, Controls on glacial valley spacing on Earth and Mars, *Geomorphology*, **116**, 189-201, 2010.
- Pelletier, J.D., P.G. DeCelles, and G. Zandt, Relationships among climate, erosion, topography, and delamination in the Andes: A numerical modeling investigation, *Geology*, **38**, 259-262, 2010.
- Pelletier, J.D., and C. Rasmussen, Geomorphically-based predictive mapping of soil thickness in upland watersheds, *Water Resources Research*, **45**, W09417, doi:10.1029/2008WR007319, 2009.
- Banks, M., and seven coauthors, An Analysis of Sinuous Ridges in the Southern Argyre Planitia, Mars using HiRISE and CTX Images and MOLA Data, *Journal of Geophysical Research*, **114**, E09003, doi:10.1029/2008JE003244, 2009.
- Pelletier, J.D., H. Mitasova, R.S. Harmon, and M. Overton, The effects of interdune vegetation changes on eolian dune field evolution: A numerical-modeling case study at Jockey's Ridge, North Carolina, USA, *Earth Surface Processes and Landforms*, **34**, 1245-1254, 2009.
- Pelletier, J.D., Engelder, T.M., Comeau, D., Hudson, A., Leclerc, M., Youberg, A., and S. Diniega, Tectonic and structural control of fluvial channel morphology in metamorphic core complexes: The example of the Catalina-Rincon core complex, Arizona, *Geosphere*, **5**, 363-384, 2009.
- Pelletier, J.D., The impact of snowmelt on the late Cenozoic landscape of the southern Rocky Mountains, USA, *GSA Today*, **19**(7), 4-10, 2009.
- Pelletier, J.D., and C. Rasmussen, Quantifying the climatic and tectonic controls on hillslope steepness and erosion rates, *Lithosphere*, **1**, 73-80, 2009.
- Huxman, T., and 7 coauthors, The Hills are Alive: Interdisciplinary Earth science at Biosphere 2, *EOS*, **90**, 120, 2009.
- Pelletier, J.D., Controls on the height and spacing of eolian ripples and transverse dunes: A numerical modeling investigation, *Geomorphology*, **105**, 322-333, 2009.
- Banks, M., and ten coauthors, HiRISE Observations of Glacial and Periglacial Morphologies in the Circum-Argyre Planitia Highlands, Mars, *Journal of Geophysical Research*, **113**, E12015, doi:10.1029/2007JE002994, 2009.

- Murray, A.B., and eleven coauthors, Geomorphology, complexity, and the emerging science of the Earth's surface, *Geomorphology*, **103**, 496-505, 2009.
- Pelletier, J.D., A.L. Leier, and J.R. Steidtmann, Wind-driven reorganization of coarse clasts on the surface of Mars, *Geology*, **37**, 55-58, 2009.
- Moore, J.E., J.D. Pelletier, and P.H. Smith, Crack propagation by differential insolation on desert surface clasts, *Geomorphology*, **102**, 472-481, 2008.
- Keating, G., J.D. Pelletier, G. Valentine, and W. Statham, Evaluating Suitability of a Tephra Dispersal Model as Part of a Risk Assessment Framework, *Journal of Volcanology and Geothermal Research*, **177**, 397-404, 2008.
- Blainey, J., and J.D. Pelletier, Infiltration on alluvial fans in arid environments: Influence of fan morphology, *Journal of Geophysical Research*, **113**, F03008, doi:10.1029/2007JF000792, 2008.
- DeLong, S.B., J.D. Pelletier, and L.J. Arnold, Climate-change-triggered sedimentation and progressive tectonic uplift in a coupled piedmont-axial system: Cuyama Valley, California, USA, *Earth Surface Processes and Landforms*, **33**, 1033-1046, 2008.
- Pelletier, J.D., Research focus: Glacial erosion and mountain building, *Geology*, **36**, 591-592, 2008.
- Pelletier, J.D., K.J. Kolb, A.S. McEwen, and R.L. Kirk, Recent gully deposits on Mars: Wet or dry flow?, *Geology*, **36**, 211-214, 2008.
- Pelletier, J.D., M.L. Cline, S.B. DeLong, C.D. Harrington, and G.N. Keating, Dispersion of channel-sediment contaminants in fluvial systems: Application to tephra redistribution following a potential volcanic eruption at Yucca Mountain, *Geomorphology*, **94**, 226-246, 2008.
- Banks, M., and J.D. Pelletier, Numerical modeling of ice-cap geometry over cratered terrain: Application to the south polar region of Mars, *Journal of Geophysical Research*, **113**, doi:10.1029/2007JE002895, 2008.
- Pelletier, J.D., Fractal behavior in space and time in a simplified model of fluvial landscape evolution, *Geomorphology*, **91**, 291-301, 2007.
- Pelletier, J.D., M. Cline, and S. DeLong, Desert pavement dynamics: Numerical modeling and field-based calibration, *Earth Surface Processes and Landforms*, **32**, 1913-1927, 2007.
- Pelletier, J.D., and M.L. Cline, Nonlinear slope-dependent transport in cinder cone evolution, *Geology*, **35**, 1067, 2007.
- Pelletier, J.D., Numerical modeling of the Cenozoic fluvial evolution of the southern Sierra Nevada, California, *Earth and Planetary Science Letters*, **259**, 85-96, 2007.
- Cook, J.P., and J.D. Pelletier, Relief threshold for eolian transport across alluvial fans, *Journal of Geophysical Research*, **112**, F02026, doi:10.1029/2006JF000610, 2007.
- Pelletier, J.D., A Cantor set model of eolian dust accumulation on desert alluvial fan terraces, *Geology*, **35**, 439-442, 2007.
- DeLong, S.B., J.D. Pelletier, and L. Arnold, Bedrock landscape evolution modeling: Calibration using geochronology and DEM analysis, *Geological Society of America Bulletin*, **119**, 157-173, 2007.
- Pelletier, J.D., Erosion-rate determination from foreland basin geometry, *Geology*, **35**, 5-8, 2007.
- Barnes, J.B., T.A. Ehlers, N. MacQuarrie, P.B. Sullivan, and J.D. Pelletier, Eocene to recent variations in erosion across the central Andean fold-thrust belt, northern Bolivia: Implications for plateau evolution, *Earth and Planetary Science Letters*, **248**, 118-133, 2006.
- Barnes, J.B., and J.D. Pelletier, Latitudinal variation of denudation in the evolution of the Bolivian Andes, *American Journal of Science*, **306**, 1-31, 2006.
- Pelletier, J.D., Sensitivity of playa windblown-dust emissions to climatic and anthropogenic change, *Journal of Arid Environments*, **66**, 62-75, 2006.

- Pelletier, J.D., S. DeLong, A.H. Al Suwaidi, M.L. Cline, Y. Lewis, J.L. Psillas, and B. Yanites, Evolution of the Bonneville shoreline scarp in west-central Utah: Comparison of scarp-analysis methods and implications for the diffusion model of hillslope evolution, *Geomorphology*, **74**, 257-270, 2006.
- Pelletier, J.D., C.D. Harrington, J.W. Whitney, M.L. Cline, S.B. DeLong, K.T. Ebert, Geomorphic control of radionuclide diffusion in desert soils, *Geophysical Research Letters*, **32**, L23401, doi:10.1029/2005GL024347, 2005.
- Pelletier, J.D., and J.P. Cook, Deposition of playa windblown dust over geologic time scales, *Geology*, **33**, 909-912, 2005.
- Pelletier, J.D., L. Mayer, P.A. Pearthree, P.K. House, J. Klawon, K. Demsey, and K.R. Vincent, An integrated approach to alluvial-fan flood hazard assessment with numerical modeling, field mapping, and remote sensing, *Geological Society of America Bulletin*, **117**, 1167-1180, 2005.
- Pelletier, J.D., Formation of oriented thaw lakes by thaw slumping, *Journal of Geophysical Research*, **110**, doi:10.1029/2004JF000158, 2005.
- Kohfield, K.E., R.L. Reynolds, J.D. Pelletier, and W. Nickling, Linking the scales of dust emissions: A workshop report, *EOS, Transactions of the American Geophysical Union*, **86**, 113-114, 2005.
- Leier, A.L, P.G. DeCelles, and J.D. Pelletier, Mountains, monsoons, and megafans, *Geology*, **33**, 289-292, 2005.
- Pelletier, J.D., Persistent drainage migration in a numerical landform evolution model, *Geophysical Research Letters*, **31**, doi:10.1029/2004GL020802, 2004.
- Pelletier, J.D., The influence of piedmont deposition on time scales of mountain-belt denudation, *Geophysical Research Letters*, **31**, doi:10.1019/2004GL020052, 2004.
- Pelletier, J.D., and S. DeLong, Oscillations in arid alluvial channels, *Geology*, **32**, 713-716, 2004.
- Hsu, L., and J.D. Pelletier, Correlation and dating of Quaternary alluvial fan surfaces using scarp diffusion, *Geomorphology*, **60**, 319-335, 2004.
- Pelletier, J.D., How do spiral troughs form on Mars?, *Geology*, **32**, 365-367, 2004.
- Pelletier, J.D., Estimation of three-dimensional flexural-isostatic response to unloading: Rock uplift due to Late Cenozoic glacial erosion in the western U.S., *Geology*, **32**, 161-164, 2004.
- Pelletier, J.D., Drainage network evolution in the Rainfall Erosion Facility: Dependence on initial conditions, *Geomorphology*, **53**, 183-196, 2003.
- Pelletier, J.D., Coherence resonance and ice ages, *Journal of Geophysical Research*, **108**, doi:10.1029/2002JD003120, 2003.
- Pelletier, J.D., Natural variability of atmospheric temperatures and geomagnetic intensity over a wide range of time scales, *Proceedings of the National Academy of Sciences of the U.S.A.*, **99**, 2546-2553, 2002.
- Pelletier, J.D., Spring-block models of seismicity: Review and analysis of a structurally-heterogeneous model coupled to a viscous asthenosphere, *Geophysical Monographs*, **120**, 27-42, 2000.
- Pelletier, J.D., Are large complex ecosystems more unstable? A theoretical reassessment with predator switching, *Mathematical Biosciences*, **163**, 91-96, 2000.
- Pelletier, J.D., Model assessments of the optimal design of nature reserves for maximizing species longevity, *Journal of Theoretical Biology*, **202**, 25-32, 2000.
- Pelletier, J.D., Statistical self-similarity of magmatism and volcanism, *Journal of Geophysical Research*, **104**, 15425-15438, 1999.
- Pelletier, J.D., and D.L. Turcotte, Self-affine time series: II. *Applications and models*, *Advances in Geophysics*, **40**, 91-166, 1999.
- Pelletier, J.D., The self-organization and scaling relationships of evolving river networks, *Journal of Geophysical Research*, **104**, 7359-7375, 1999.

- Pelletier, J.D., The species-area effect and self-affine dynamics in a biogeographical model of speciation and extinction, *Physical Review Letters*, **82**, 1983-1987, 1999.
- Pelletier, J.D., and D.L. Turcotte, Shapes of river networks and leaves: Are they statistically similar?, *Philosophical Transactions of the Royal Society: Biological Sciences*, **354**, 1-5, 1999.
- Pelletier, J.D., Paleointensity variations of Earth's magnetic field and their relationship with polarity reversals, *Physics of the Earth and Planetary Interiors*, **110**, 115-128, 1999.
- Turcotte, D.L., J.D. Pelletier, and W.I. Newman, Networks with side-branching in biology, *Journal of Theoretical Biology*, **193**, 577-592, 1998.
- Pelletier, J.D. and D.L. Turcotte, Application of a stochastic deposition and erosion model to reservoir heterogeneity and stratigraphic data, Numerical Experiments in Stratigraphy: Recent Advances in Stratigraphic/Sedimentologic Computer Simulation, *SEPM Special Publications*, **62**, 253-264, 1998.
- Pelletier, J.D., The power-spectral density of atmospheric temperature from time scales of 10^{-2} to 10^6 yr, *Earth and Planetary Science Letters*, **158**, 157-164, 1998.
- Pelletier, J.D. and D.L. Turcotte, Long-range persistence in climatological and hydrological time series: analysis, modeling, and application to drought hazard assessment, *Journal of Hydrology*, **203**, 198-208, 1997.
- Pelletier, J.D., B.D. Malamud, T. Blodgett, and D.L. Turcotte, Scale-invariance of soil moisture variability and its implications for the frequency-size distribution of landslides, *Engineering Geology*, **48**, 255-268, 1997.
- Pelletier, J.D. and D.L. Turcotte, Synthetic stratigraphy with a stochastic diffusion model of sedimentation, *Journal of Sedimentary Research*, **67**, 1060-1067, 1997.
- Pelletier, J.D., Analysis and modeling of the natural variability of climate, *Journal of Climate*, **10**, 1331-1342, 1997.
- Pelletier, J.D., Kardar-Parisi-Zhang scaling of the top of the convective boundary layer and the fractal structure of cumulus cloud fields, *Physical Review Letters*, **78**, 2672-2675, 1997.
- Pelletier, J.D. and D.L. Turcotte, Scale-invariant topography and porosity variations in fluvial sedimentary basins, *Journal of Geophysical Research*, **101**, 28,165-28,175, 1996.
- Pelletier, J.D., Variations in solar luminosity from time scales of minutes to months, *Astrophysical Journal*, **463**, L41-L45, 1996.
- Pelletier, J.D., M.H. Shapiro, and T.A. Tombrello, Molecular dynamics simulations of low-energy cluster deposition on metallic targets, *Nuclear Instruments and Methods in Physics Research B*, **67**, 296-300, 1992.

Major grant awards last 5 years as PI or co-PI

- *National Science Foundation Earth Surface Processes Program, Transformative Behavior of Water, Energy and Carbon in the Critical Zone: An Observatory to Quantify Linkages among Ecohydrology, Biogeochemistry, and Landscape Evolution (with 11 co-PIs), \$4.3M over five years; 7/1/09-6/30/14.
- *Army Research Office Terrestrial Sciences Program, Predictive mapping of soil thickness and erosion rates in semi-arid regions (with Craig Rasmussen, \$210,000 over three years, 7/1/04-6/30/07)
- *NASA Mars Data Analysis Program, Evaluating hypotheses for glaciation on Mars: A multi-instrument and numerical modeling approach (with Jeff Kargel, \$200,000 over three years; 7/1/07-6/30/10).
- State of Arizona Water Sustainability Competitive Grants Program, Integrated surface and subsurface response of alluvial basins to ephemeral stream channel recharge and urban-focused recharge (with Ty Ferre, \$180,000 over three years; 7/1/05-6/30/08).

NASA Mars Fundamental Research Program, Formation and evolution of the Martian spiral troughs (sole-PI, \$120,000 over three years; 7/1/05-6/30/08).

Army Research Office Terrestrial Sciences Program, Eolian Modeling System: Predicting windblown dust hazards in battlefield environments (sole-PI, \$166,000 over three years, 7/1/04-6/30/07)

National Science Foundation Geology and Paleontology Program, Fluvial systems and climate in the southwestern U.S. (sole-PI, \$170,000 over two years, 6/1/03-5/31/06).

*denotes active grant

Grant awards last 5 years as co-I or collaborator

**ExxonMobil Corporation*, Convergent Orogen Systems Analysis (COSA) (PI: Peter DeCelles, 7/1/07-present)

**NASA Mars Data Analysis Program*, Geologic studies of the Martian midlatitudes (PI: Alfred McEwen, 7/1/07-6/30/10)

**NASA Office of Earth Science*, Satellite, airborne, and ground-based assessment of cryospheric changes in the Copper River/Chitina basins, and adjoining ranges (Alaska) from Late Glacial Maximum to now (PI: Jeff Kargel, 7/1/07-6/30/10)

National Science Foundation Human and Social Dynamics Program, Paleoclimatic Change, Landscape Evolution, and Cultural Transformation In Far Western Tibet, 2500 bp-present (with PI Mark Aldenderfer, 7/1/05-6/30/08).

Courses taught (for period of current rank)

Course	Level	Aver. Size	Years Taught	Web Site/Description
<i>Introduction to Geomorphology</i>	Sr-Grad	25	4	geomorphology.geo.arizona.edu //geos450/geos450.html lectures, labs, field trips
<i>Introduction to Natural Science</i>	Fr	120	1	nats101.geo.arizona.edu lectures, labs, for nonmajors
<i>Analytical and Num. Modeling</i>	Grad	6	1	modeling geologic processes
<i>Field Geomorphology</i>	Grad	6-8	2	field mapping/soils/dating in the Sonoran/Mojave Deserts
<i>Fluvial Seminar</i>	Grad	15	1 (w/ Baker)	current topics/literature review

Deposition of playa windblown dust over geologic time scales

Jon D. Pelletier*
Joseph P. Cook

Department of Geosciences, University of Arizona, Gould-Simpson Building, 1040 East Fourth Street,
Tucson, Arizona 85721-0077, USA

ABSTRACT

Thick eolian deposits are commonly observed beneath desert pavements downwind of dust-emitting playas. These deposits play an important role in piedmont-surface evolution, controlling surface hydrologic conductivity and rates of pedogenesis. To better understand the factors controlling the spatial distribution of eolian deposition, we developed a numerical model that treats deposition from spatially distributed playa sources using analytic point-source solutions for deposition from a Gaussian plume. The model also accounts for complex downwind topography. As a test case, model predictions were compared to eolian deposit thicknesses on Eagle Mountain piedmont, southern Amargosa Valley, California, which receives dust from nearby Franklin Lake playa. The close relationship between the model predictions and mapped thicknesses suggests that eolian transport and deposition can be modeled from basin to regional scales within this framework. These results have important implications for hydrologic, pedogenic, and air-quality problems.

Keywords: eolian, playa, Quaternary, numerical model, Gaussian plume.

INTRODUCTION

The dust cycle in arid environments is characterized by a net eolian transfer of dust from playas to piedmonts (Pye, 1987). Understanding the processes and rates of this transfer is important for many basic and applied geologic problems. For example, since windblown dust is a human health hazard and a visibility problem (e.g., Samet et al., 2000; Watson, 2002), rates of dust transport must be constrained over geologic time scales to identify significant trends and anthropogenic controls in modern dust records. Climatically, eolian dust contributes to global climate change by modifying Earth's albedo (Harrison et al., 2001). Geomorphically, dust deposition plays a fundamental role in the evolution of piedmont surfaces and soils (Yaalon and Ganor, 1973; McFadden et al., 1987; Reheis et al., 1995; Wells et al., 1995). Hydrologically, eolian deposits control surface conductivity (Yaalon and Ganor, 1973). Predicting recharge pathways to subsurface aquifers therefore requires accurate predictive models for eolian deposition on piedmont surfaces at basin to regional scales over geologic time.

Dust deposition rates exhibit strong variability over a wide range of spatial and temporal scales, reflecting variations in source location, regional topography, climatic change, and other factors. Increased pedogenic rates in the Holocene, for example, are associated with increased aridity and higher dust fluxes (Chadwick and Davis, 1990; Reheis et al., 1995). Spatial variability in dust transport and deposition has also been quantified, but available data are of limited resolution (Reheis et al., 1995; Reheis, 2003). Moreover, although dust transport is inherently a multiscale problem, many aspects of dust research focus on either microscale (e.g., crust formation and disturbance) or macroscale (e.g., global numerical modeling) processes, with few studies aimed squarely at intermediate scales (Kohfeld et al., 2005). Kohfeld et al. recommended bridging this gap by integrating regional-scale numerical modeling and field-based geologic studies. This study adopts that approach with a combination of basin-scale numerical modeling, Quaternary surficial geologic mapping, and field-based measurements to quantify dust deposition at spatial scales ranging from 10^1 to 10^5 m over several Quaternary time scales.

FIELD OBSERVATIONS

Our study area is located in southern Amargosa Valley, California, where Franklin Lake playa abuts the Eagle Mountain piedmont (Fig. 1A). The water table in Franklin Lake playa is <3 m below the surface (Czarnecki, 1997). Vapor discharge from this shallow aquifer creates a "soft, puffy, porous" surface responsible for unusually high dust fluxes (Czarnecki, 1997, p. 5). Czarnecki identified several distinct geomorphic surfaces on Franklin Lake playa that can be readily identified in LANDSAT imagery (Fig. 1A). For the purposes of numerical modeling, the active portion of the playa was mapped based on Czarnecki's map of playa surfaces with significant dust-emitting potential (Fig. 1A).

The Eagle Mountain piedmont acts as the depositional substrate for dust emitted from Franklin Lake playa under northerly wind conditions (see wind-rose diagram in Fig. 1A). Silt-rich eolian deposits occur directly underneath the desert pavements of Eagle Mountain piedmont, varying in thickness from 0 to 80 cm based on soil-pit measurements (Data Repository Appendix DR1¹). The technical term for these deposits is cumelic eolian epipedons (McFadden et al., 2005), but we refer to them as eolian or silt layers for simplicity. These layers are predominantly composed of silt but also include some fine sand and soluble salts. The homogeneity of these deposits, combined with their rapid transition to gravelly alluvial fan deposits below, makes the layer thickness a reasonable proxy for the total dust content of the soil.

Alluvial fan terraces on Eagle Mountain piedmont have a range of ages, enabling a temporal as well as a spatial record of dust deposition to be reconstructed. Eagle Mountain piedmont exhibits the classic sequence of Quaternary alluvial fan terraces widely recognized in the southwestern United States (Bull, 1991). This terrace sequence is significant for this study because each surface represents a distinct time interval over which dust has been accumulating. Silt layers were observed on all Eagle Mountain terraces that were late Pleistocene in age or older, with maximum values for each terrace unit located closest to the playa. Mapping and correlation of the units to the regional chronology of Whitney et al. (2004) are described in Appendix DR1.

In this study we focus on silt thicknesses of the Qa3 terrace unit (middle to late Pleistocene) because of its extensive preservation and limited evidence of hillslope erosion. Silt thicknesses were measured at locations with undisturbed planar terrace remnants to the greatest extent possible. Repeat measurements of silt thickness within a local area generally yielded the same values to within 3 cm. A color map of silt layer thickness for this surface (obtained by spherical kriging in ArcGIS 9.0) is shown in Figure 1B, draped over the U.S. Geological Survey 30 m digital elevation model and an orthophotograph of the area. Silt thickness is observed to decrease by a factor of ~ 2 for every 1 km of distance from the playa. Several kilometers downwind, a background thickness of 15–20 cm was observed on Qa3 surfaces. The strongly localized nature of downwind deposition in this area suggests that Franklin Lake playa is the source for nearly all of the eolian deposition on Eagle Mountain piedmont. Localized deposition also implies that dust deposition rates may vary regionally by an order of magnitude or more, down to spatial scales of 1 km or less, with important implications for desert surface and soil evolution.

Figure 2A illustrates plots of silt thickness as a function of downwind distance, for comparison with two-dimensional model results

¹GSA Data Repository item 2005177, Appendix DR1, further discussion of dust deposition and field-based measurements, is available online at www.geosociety.org/pubs/ft2005.htm, or on request from editing@geosociety.org or Documents Secretary, GSA, P.O. Box 9140, Boulder, CO 80301-9140, USA.

*E-mail: jon@geo.arizona.edu.

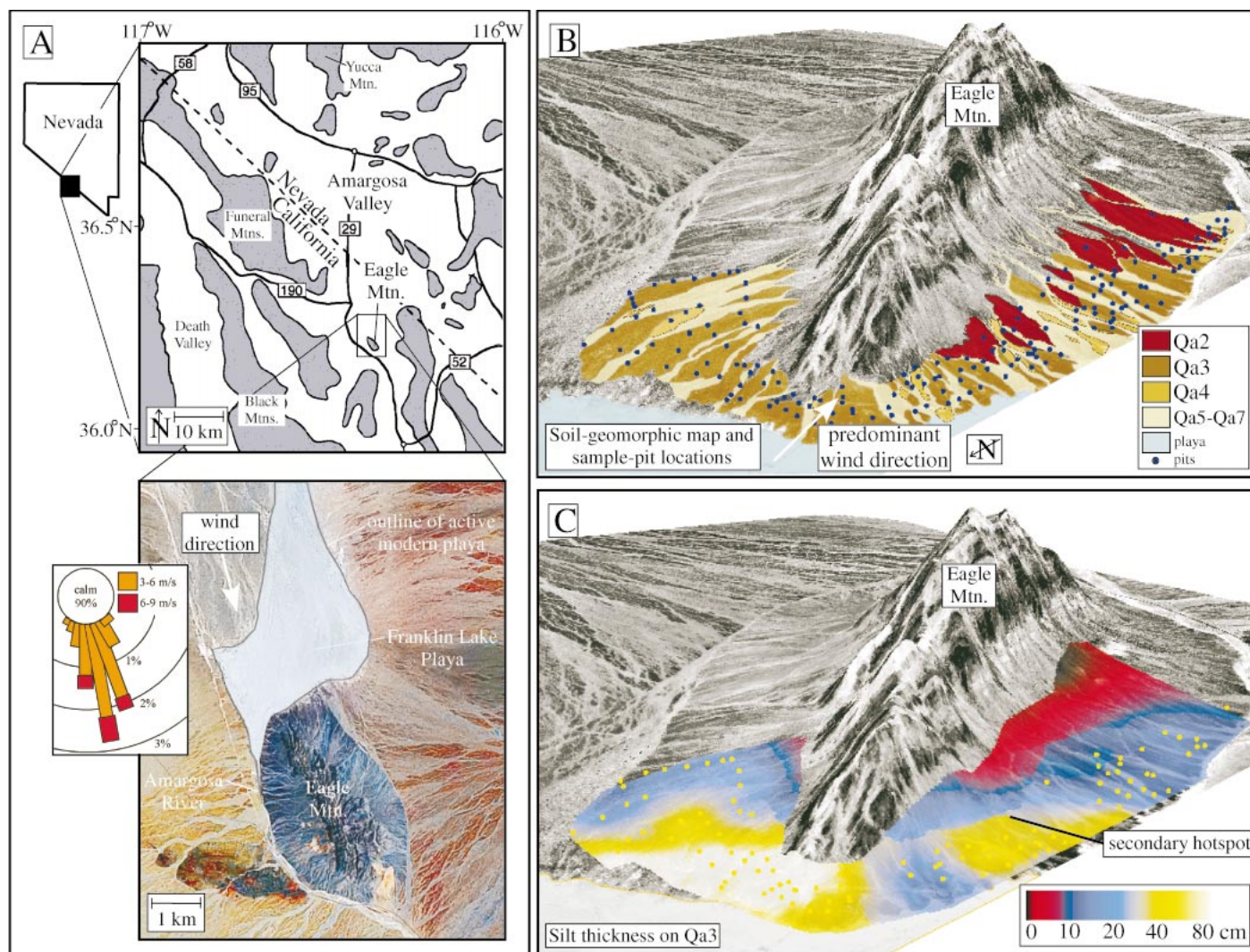


Figure 1. A: Location map and Landsat image of Eagle Mountain piedmont and adjacent Franklin Lake playa, southern Amargosa Valley, California. Predominant wind direction is SSE, as shown by wind-rose diagram (adapted from January 2003–January 2005 data from Western Regional Climate Center, 2005). Calm winds are defined to be <3 m/s. B: Soil-geomorphic map and oblique aerial perspective of Eagle Mountain piedmont, looking southeast. Terrace map units are based on regional classification by Whitney et al. (2004), discussed in Appendix DR1 (see footnote 1). Approximate ages: Qa2—middle Pleistocene, Qa3—middle to late Pleistocene, Qa4—late Pleistocene, Qa5–Qa7—latest Pleistocene to active. C: Color map of eolian silt thickness on Qa3 (middle to late Pleistocene) surface, showing maximum thicknesses of 80 cm close to playa source, decreasing by factor of ~2 for each 1 km of distance downwind. Far from playa, background values of ~20 cm were observed.

(Appendix DR1). This plot includes all measurements collected from terrace units late Pleistocene in age or older (Qa4–Qa2) within a 1-km-wide swath of western Eagle Mountain piedmont. Data from the Qa4 and Qa2 units show a similarly rapid downwind decrease in silt thickness, illustrating that the Qa3 pattern is robust. Silt thicknesses were relatively similar on the three terrace units at comparable distances from the playa. This similarity was not expected, given the great differences in age between the three surfaces. This may be partly explained by the fact that Qa2 surfaces have undergone extensive hill-slope erosion (and hence preserve only a portion of the total eolian material deposited over time) and that Qa4 surfaces have received a higher average dust flux because they have existed primarily during the warm dry Holocene. The Qa5 unit (latest Pleistocene) exhibited uniformly thin deposits underlying a weak pavement, independent of distance from the playa, suggesting that the trapping ability of young surfaces is limited by weak pavement development.

NUMERICAL MODEL

Atmospheric transport of particulate matter can be modeled as a combination of turbulent diffusion, downwind advection, and gravita-

tional settling (terms one, two, and three from left to right in equation 1). The steady-state equation describing these processes is given by

$$K \left(\frac{\partial^2 c}{\partial x^2} + \frac{\partial^2 c}{\partial y^2} + \frac{\partial^2 c}{\partial z^2} \right) - u \frac{\partial c}{\partial x} + q \frac{\partial c}{\partial z} = 0, \quad (1)$$

where K is the turbulent diffusivity, c is the particle concentration, x is the downwind distance, y is the crosswind distance, z is the vertical distance from the ground, u is the mean wind velocity, and q is the settling velocity (model geometry shown in Fig. 2B). Solutions to equation 1 are known as Gaussian plumes. This version of the advection-diffusion-settling equation assumes that K and u are uniform. More complex models are also available in which K and u vary with height to better represent transport processes close to the ground (e.g., Koch, 1989; Huang, 1999).

Deposition from a Gaussian plume is modeled by treating the ground as a “sink” for particles. Deposition in this model is characterized by a deposition velocity, p , defined as the fraction of the particle concentration just above the ground that undergoes deposition per unit time. In this model framework, deposition at the ground surface is

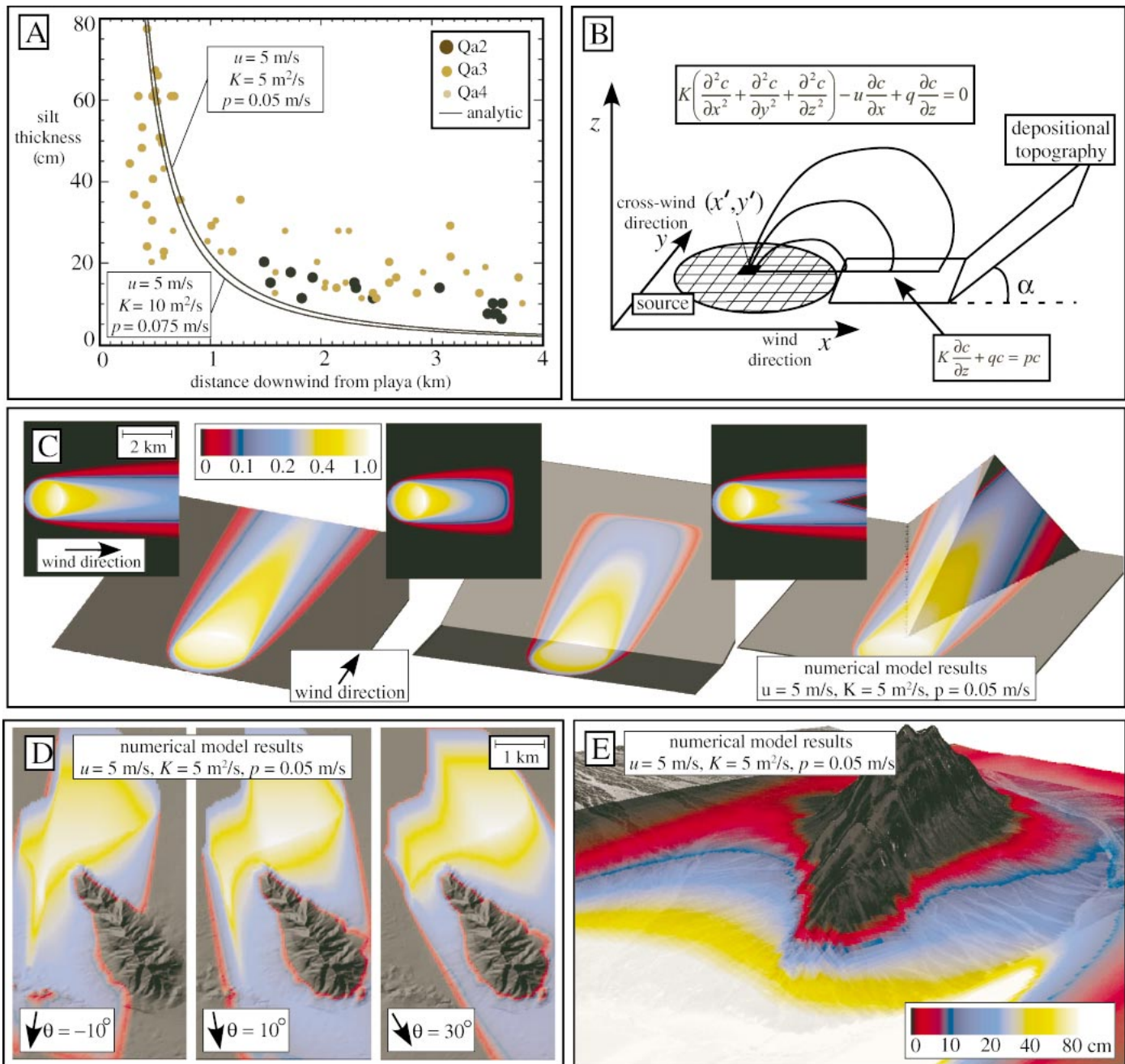


Figure 2. A: Plot of eolian silt thickness vs. downwind distance, with analytic solutions for two-dimensional model (equation DR1; see footnote 1) for representative values of model parameters. B: Schematic diagram of model geometry. Depositional topography shown in this example is inclined plane located downwind of source (but model can accept any downwind topography). C: Color maps of three-dimensional model results, illustrating role of variable downwind topography. In each case, model parameters are $u = 5$ m/s, $K = 5$ m²/s, and $p = 0.05$ m/s (see text). Downwind topography is, from left to right, flat plane, inclined plane, and triangular ridge. Width and depth of model domain are both 6 km. D: Color maps of three-dimensional model results for deposition downwind of Franklin Lake playa, illustrating role of variable wind direction. From left to right, wind direction is $\theta = -10^\circ$ (0° is due south), 10° , and 30° . E: Color map of three-dimensional model results obtained by integrating model results over range of wind conditions, weighted by wind-rose data in Figure 1A.

equal to the downward flux due to turbulent diffusion and particle settling. This balance provides a flux boundary condition at $z = 0$:

$$K \frac{\partial c}{\partial z} \bigg|_{z=0} + qc(x, y, 0) = pc(x, y, 0). \quad (2)$$

Physically, the deposition velocity represents the trapping ability of the surface, independent of whether the particles are falling under gravity. Silt, for example, has a negligible settling velocity but a finite depo-

sition velocity because silt particles are deposited as they fall or lodge between the crags of a rough surface (e.g., clasts in a desert pavement).

The three-dimensional concentration field for a point source located at $(x', y', 0)$, obtained by solving equation 1 and 2, is given by

$$c_p(x, y, z, x', y') = \frac{Q}{\sqrt{\frac{4\pi K(x - x')^2}{u}}} \exp \left[-\frac{u(y - y')^2}{4K(x - x')} \right]$$

$$\times \left\{ \frac{\exp \left[-\frac{uz}{4K(x-x')} \right]}{\sqrt{\pi u K(x-x')}} - \frac{p}{uK} \exp \left[\frac{pz}{K} + \frac{p^2(x-x')}{Ku} \right] \right. \\ \left. \cdot \operatorname{erfc} \left[\sqrt{\frac{u}{4K(x-x')}} z + p \sqrt{\frac{x-x'}{Ku}} \right] \right\}, \quad (3)$$

where Q is the source emission rate and erfc is the complementary error function. Equation 3 combines the two-dimensional solution of Smith (1962) with an additional term required to describe crosswind transport (Huang, 1999). Equation 3 assumes that the settling velocity q is small compared with the deposition velocity p . Stokes' Law (Allen, 1997) implies a settling velocity of <1 cm/s for silt particles (i.e., particles <0.05 mm) in air. Deposition velocities consistent with the spatial distribution of deposition on Eagle Mountain piedmont, however, are ~ 5 cm/s, or at least 5 times greater than q .

For nonpoint sources, equation 3 can be integrated to give

$$c(x, y, z) = \int_{-\infty}^{\infty} \int_{-\infty}^{\infty} c_p(x', y') dx' dy'. \quad (4)$$

Using equations 3 and equations 4, the deposition rate on a flat surface is given by $pc(x, y, 0)$. Deposition on a complex downwind surface can be estimated as $pc[x, y, h(x, y)]$, where $h(x, y)$ is the elevation of the downwind topography. This approach is only an approximation of the effects of complex topography because mass loss from the plume is still assumed to occur along a horizontal plane in equation 3. However, by using the elevated plume concentration—i.e., $c[x, y, h(x, y)]$ —to estimate the deposition term pc , the model approximates the spatially variable deposition that occurs as the plume intersects with complex topography. Further model details are discussed in Appendix DR1 (see footnote 1).

Model results are shown in Figure 2C to illustrate the role of complex downwind topography in controlling deposition patterns. In each case, a circular source with uniform Q was considered with model parameters $u = 5$ m/s, $K = 5$ m²/s, and $p = 0.05$ m/s. From left to right, the downwind topography was considered to be flat, an inclined plane, and a triangular ridge. Relative to flat topography, the inclined plane leads to a short plume, and the triangular ridge diverts and bisects the plume.

Long-term dust transport does not correspond to a single wind direction as assumed in the simplified cases of Figure 2C. The effects of multiple wind directions can be incorporated into the model by integrating a series of model runs with a range of wind directions, each weighted by the frequency of that wind direction in the wind-rose diagram. Figure 2D illustrates model results for the Eagle Mountain region with wind directions from $\theta = -10^\circ$ to $+30^\circ$ ($\theta = 0^\circ$ is due south). Figure 2E illustrates the integrated model corresponding to the wind-rose diagram of Figure 1A. The thickness values mapped in Figure 2E correspond to a uniform Q value of 1.0 m/k.y. (assuming a Qa3 surface age of 50 ka), obtained by scaling the model results for different values of Q to match the maximum thickness values between the model and observed data. The modeled and observed deposition patterns match each other in most respects. However, the secondary hot spot located on the western piedmont of the study area is not reproduced by the model. This feature could result from more westerly paleowinds transporting more dust eastward from the Amargosa River relative to modern conditions. Alternatively, it could result from enhanced hillslope erosion of Qa3 surfaces in this area.

CONCLUSIONS

Numerical modeling of dust transport and deposition holds great promise for integration with classic methods in dust research. The model may be calibrated, for example, using point data from modern dust

traps in order to provide a physically based regional reconstruction of dust deposition over interannual time scales (e.g., Reheis, 2003). In addition, the modeling framework may be useful for modeling sub-grid-scale processes within global-scale numerical dust-transport models.

ACKNOWLEDGMENTS

We thank Dave Miller for introducing us to this problem. Rich Reynolds, Marith Reheis, and Chris Menges provided helpful conversations on the geology of southern Amargosa Valley and dust transport in general. Peter Haff, Marith Reheis, and an anonymous reviewer provided very helpful reviews. We gratefully acknowledge support by the Army Research Office Terrestrial Sciences Program grant W911NF-04-1-0266.

REFERENCES CITED

- Allen, P.A., 1997, *Earth surface processes*: New York, Oxford University Press, 404 p.
- Bull, W.B., 1991, *Geomorphic responses to climatic change*: New York, Oxford University Press, 326 p.
- Chadwick, O.A., and Davis, J.O., 1990, Soil-forming intervals caused by eolian sediment pulses in the Lahontan basin, northwestern Nevada: *Geology*, v. 18, p. 243–246, doi: 10.1130/0091-7613(1990)018<0243:SFICBE>2.3.CO;2.
- Czarnecki, J.B., 1997, *Geohydrology and evapotranspiration at Franklin Lake playa, Inyo County, California*: U.S. Geological Survey Water-Supply Paper 2377, 75 p.
- Harrison, S.P., Kohfeld, K.E., Roelandt, C., and Claquin, T., 2001, The role of dust in climate changes today, at the last glacial maximum, and in the future: *Earth Science Reviews*, v. 54, p. 43–80, doi: 10.1016/S0012-8252(01)00041-1.
- Huang, C.H., 1999, On solutions of the diffusion-deposition equation for point sources in turbulent shear flow: *Journal of Applied Meteorology*, v. 38, p. 250–254, doi: 10.1175/1520-0450(1999)038<0250:OSOTDD>2.0.CO;2.
- Koch, W., 1989, A solution of the two-dimensional atmospheric diffusion equation with height-dependent diffusion coefficient including ground level absorption: *Atmospheric Environment*, v. 23, p. 1729–1732, doi: 10.1016/0004-6981(89)90057-7.
- Kohfeld, K.E., Reynolds, R.L., Pelletier, J.D., and Nickling, W., 2005, Linking the scales of process, observation, and modeling of dust emissions: *Eos (Transactions, American Geophysical Union)*, v. 86, p. 113–114.
- McFadden, L.D., Wells, S.G., and Jercinovich, M.J., 1987, Influences of eolian and pedogenic processes on the origin and evolution of desert pavements: *Geology*, v. 15, p. 504–508, doi: 10.1130/0091-7613(1987)15<504:IOEAPP>2.0.CO;2.
- McFadden, L.D., Eppes, M.C., Gillespie, A.R., and Hallet, B., 2005, Physical weathering in arid landscapes due to diurnal variation in the direction of solar heating: *Geological Society of America Bulletin*, v. 117, p. 161–173, doi: 10.1130/B25508.1.
- Pye, K., 1987, *Aeolian dust and dust deposits*: London, Academic Press, 334 p.
- Reheis, M.C., 2003, *Dust deposition in Nevada, California, and Utah, 1984–2002*: U.S. Geological Survey Open-File Report 03–138, 11p.
- Reheis, M.C., Goodmacher, J.C., Harden, J.W., McFadden, L.D., Rockwell, T.K., Shroba, R.R., Sowers, J.M., and Taylor, E.M., 1995, Quaternary soils and dust deposition in southern Nevada and California: *Geological Society of America Bulletin*, v. 107, p. 1003–1022, doi: 10.1130/0016-7606(1995)107<1003:QSADDI>2.3.CO;2.
- Samet, J.M., Dominici, F., Curriero, F.C., Cousac, I., and Zeger, S.L., 2000, Fine particulate air pollution and mortality in 20 U.S. cities, 1987–1994: *New England Journal of Medicine*, v. 343, p. 1742–1749, doi: 10.1056/NEJM200012143432401.
- Smith, F.B., 1962, The problem of deposition in atmospheric diffusion of particulate matter: *Journal of Atmospheric Sciences*, v. 19, p. 429–434, doi: 10.1175/1520-0469(1962)019<0429:TPODIA>2.0.CO;2.
- Watson, J.G., 2002, *Visibility: Science and regulation*: Air and Waste Management Association Journal, v. 52, p. 628–713.
- Wells, S.G., McFadden, L.D., Poths, J., and Olinger, C.T., 1995, Cosmogenic ³He surface-exposure dating of stone pavements: Implications for landscape evolution in deserts: *Geology*, v. 23, p. 613–616, doi: 10.1130/0091-7613(1995)023<0613:CHSEDO>2.3.CO;2.
- Western Regional Climate Center, 2005, *Station Wind Rose: Amargosa Valley Nevada: Desert Research Institute*, <http://www.wrcc.dri.edu/cgi-bin/wea.windrose.pl?nvamar> (July, 2005).
- Whitney, J.W., Taylor, E.M., and Wesling, J.R., 2004, Quaternary stratigraphy and mapping in the Yucca Mountain area, in Keefer, W.R., et al., eds., *Quaternary paleoseismology and stratigraphy of the Yucca Mountain area, Nevada*: U.S. Geological Survey Professional Paper 1689, p. 11–23.
- Yaalon, D.H., and Ganor, E., 1973, The influence of dust on soils in the Quaternary: *Soil Science*, v. 116, p. 146–155.

Manuscript received 12 July 2005

Revised manuscript received 22 July 2005

Manuscript accepted 25 July 2005

Printed in USA

Sensitivity of playa windblown-dust emissions to climatic and anthropogenic change

J.D. Pelletier*

Department of Geosciences, The University of Arizona, 1040 E. Fourth St., Tucson, Arizona, 85721, USA

Received 31 March 2005; received in revised form 1 July 2005; accepted 13 October 2005

Available online 1 December 2005

Abstract

Windblown dust is a significant component of atmospheric PM (particulate matter) in arid regions worldwide, with adverse effects on human health and visibility. In the future, windblown dust emissions are likely to increase if water tables drop as a result of climatic or anthropogenic changes. To manage this hazard, air quality managers need quantitative models that predict the impact of climatic and anthropogenic change on dust emissions. To meet this need, we constructed a process based numerical model that includes Richards' equation for vertical moisture flow in the unsaturated zone, Chepil's model for the effect of surface soil moisture on threshold wind speed, and the saltation equation, which also predicts the rate of dust emission from the surface to within a multiplicative factor. This model is solved analytically for a Weibull distribution of wind speeds under steady state moisture conditions, providing a single predictive equation for the long term average saltation flux based on local meteorological and hydrological parameters. The model equations are used to predict the increase in saltation flux and dust emissions resulting from the dessication of a wet playa by climatic change, stream diversion, or groundwater withdrawal. The model is calibrated using CLIM MET station data collected near Soda (dry) Lake, California. The model results identify a critical range of water table depths between 3 and 10 m (depending on hydrological parameters) in which small increases in water table depth cause large, nonlinear increases in windblown dust emissions. For water tables deeper than 10 m, dust emissions are close to their maximum value and are largely independent of water table depth. This analysis highlights the importance of preserving the hydrological balance of wet playas in order to minimize windblown dust emissions. Future climatic changes may also influence dust emissions through changes in the mean or variability of wind speeds.

*Tel.: +1 520 626 2126.

E mail address: jon@geo.arizona.edu.

For representative model parameters, 10% increases in the mean and variability of wind speeds, for example, are predicted to increase dust emissions by 80% and 20% within this model framework. © 2005 Elsevier Ltd. All rights reserved.

Keywords: Unsaturated flow; Modeling; Saltation; Playa

1. Introduction

Particulate matter (PM) is a significant human health hazard capable of causing long-term respiratory ailments and even sudden death (Vedal, 1997; Samet et al., 2000). Windblown dust is a significant component of PM, especially at its highest and most dangerous levels (Claiborne et al., 2000). Windblown dust also impacts visibility, contributing to vehicle accidents and a loss of scenic quality. Air-quality managers in the western US are now developing source-emission protocols to manage PM concentrations up to 50 years into the future (Watson, 2002). Few quantitative models, however, are currently available to predict the impacts of climatic and anthropogenic changes on future windblown-dust emissions.

Windblown dust is a hazard in many areas worldwide, but to motivate this discussion we consider the western US in particular. Most major population centers in the western US have been designated serious nonattainment areas for PM standards (US EPA, 2004). The western US is a dust-hazard hotspot for several reasons. First, population growth is among the highest in the nation (Liverman and Meredith, 2002). Urban growth, especially sprawl, puts more people at risk for dust-related health problems and generates more disturbed land to act as windblown-dust sources. Second, the low vegetation cover and fine-grained texture of many western US playas cause especially high rates of dust emission. Owens (dry) Lake, for example, has the highest long-term dust flux of any area in the US. Dust from Owens Lake is a regional problem, with transport distances of up to 400 km (Reheis et al., 2002). Owens Lake became a primary regional dust source starting only in 1913 with the diversion of water to metropolitan Los Angeles. Shallow water tables in many western US playas mitigate their dust-production potential. In the future, however, climate change, stream diversion, and/or groundwater withdrawal could eliminate this mitigating influence, creating many new dust sources comparable to Owens Lake.

Previous studies have identified wind speed and soil moisture as important controlling factors of windblown-dust activity. Soil moisture is rarely measured directly, but precipitation totals for periods between 2 months and 2 years prior to dust events are correlated with dust event frequency (e.g., Brazel and Nickling, 1987; Littmann, 1991; Yu et al., 1993; Bach et al., 1996; Holcombe et al., 1997; Lancaster and Helm, 2000; Okin and Reheis, 2002). Empirical relationships between dust events and climate have been found to be inaccurate for prediction unless soil moisture is explicitly modeled (McTainsh et al., 1998).

Soil moisture affects dust emissions in two primary ways: first, as a direct influence on threshold wind speed through its effects on soil cohesion, and second, as an indirect control through its effect on vegetation cover. Vegetation cover controls the aerodynamic roughness of the surface, which, in turn, controls the turbulent shear stresses imparted to the surface. The second of these factors is the most difficult to quantify because the relationships between soil moisture, vegetation cover, and turbulent shear stresses are difficult to quantify. In this paper, we focus only on the primary role of soil moisture as a

cohesive agent. As a result, our model is most appropriate for the bare ground or sparse vegetation of playas. The model we constructed can address both steady-state and transient effects of soil moisture, but here we consider only the steady-state case. Under conditions of steady-state capillary rise from a shallow water table, analytical solutions for surface soil moisture and saltation flux can be obtained. These solutions can be used to predict the increase in dust emissions resulting from a water-table drop and/or an increase in the mean or variability of wind speeds. Temporal variations in microsurficial characteristics (i.e. the formation and disturbance of protective crusts) are included in the model implicitly using a stochastic variable for threshold wind speed.

2. Model description

The model of this paper employs several important assumptions. First, since the model is one-dimensional model, different components of the playa system are not resolved. In nature, dust storms often originate when coarse sand from the playa margin enters into saltation. As sand blows across the playa surface, the crust is disturbed, releasing both sand and fine-grained sediments (silt and clay). Sand from the playa surface becomes part of a self-sustaining saltation “cloud” that drives dust production from the surface. The model of this paper assumes that flux of blowing sand along the playa margin can be used as a proxy for dust emission from the playa. This assumption is supported by data showing a strong correlation between horizontal saltation flux and the vertical dust flux (Gillette et al., 2003). However, the model is not applicable to playas with no upwind sand available for transport. In future work, the one-dimensional model framework presented here may be integrated into a spatially distributed model that includes the complexities of different playa types.

A second key assumption is that moisture transport occurs within the liquid phase only (i.e. by capillary rise). In fact, moisture transport from deeper water tables takes place by a combination of liquid and vapor-phase transport. Vapor-phase transport is a second-order effect that is neglected in this model. Finally, the effects of temperature and moisture on the surface resistance to erosion (e.g. formation of salt crusts) are not considered but are an important avenue for future research.

First we consider the physics of steady-state capillary rise from a water table. This model component is designed to predict the volumetric soil moisture profile using water-table depth and soil-hydrologic parameters. For a shallow water table, capillary rise leads to a moist surface that suppresses dust emissions under all but the most extreme wind conditions. For a deep water table, the dry surface is at or near its maximum dust-producing potential and changes in subsurface moisture have little or no effect on dust emissions. Our model aims to quantify the range of water-table depths over which this transition from a wet to dry playa takes place. An important assumption in this analysis is that precipitation events are rare enough that the surface is near its steady-state moisture value most of the time. That assumption is later verified using Soda Lake CLIM-MET station data.

The vertical transport of moisture in an unsaturated soil is governed by Richards' equation

$$\frac{\partial \psi}{\partial t} = \frac{\partial}{\partial z} \left(K_{\psi} \frac{\partial \psi}{\partial z} - 1 \right), \quad (1)$$

where ψ is the suction, t is time, z is height above the water table, and K_ψ is the hydraulic conductivity. For steady upward flow, Eq. (1) can be written as

$$E = \frac{\partial}{\partial z} \left(K_\psi \frac{\partial \psi}{\partial z} - 1 \right), \quad (2)$$

where E is the steady-state evaporation rate. Gardner (1958) proposed the following relationship between K_ψ and ψ to solve Eq. (2):

$$K_\psi = \frac{a}{\psi^n + b}, \quad (3)$$

where a and b are empirical constants for each soil. Gardner (1958) provided analytical solutions for suction profiles at several values of n . Most soils have n values between 2 and 3 (Gardner and Fireman, 1958). Here we assume $n = 2$, the most appropriate value for fine-grained playa sediments according to Gardner (1958). The solution to Eq. (2) for $n = 2$ and with boundary condition $\psi = 0$ at $z = 0$ is (Gardner, 1958)

$$z = \frac{1}{\sqrt{(E/a)((E/a)b + 1)}} \tan^{-1} \left(\sqrt{\frac{E/a}{(E/a)b + 1}} \psi \right). \quad (4)$$

The value of E is determined by the maximum soil moisture flux within the profile, given by Gardner (1958) and Warrick (1988) as

$$\frac{E}{a} = \left(\frac{\pi}{2d} \right)^2, \quad (5)$$

where d is the water-table depth. Substituting Eq. (5) into Eq. (4) and solving for the suction at $z = d$ gives

$$\psi_{z=d} = \sqrt{b + \left(\frac{2d}{\pi} \right)^2 \tan^2 \left(\sqrt{\left(\frac{\pi}{2} \right)^2 \left(\left(\frac{\pi}{2d} \right)^2 b + 1 \right)} \right)}. \quad (6)$$

Van Genuchten's model (Van Genuchten, 1980) predicts the surface soil moisture from the suction to be

$$\frac{\theta_{z=d} - \theta_r}{\theta_s - \theta_r} = (1 + (\alpha \psi_{z=d})^{1+\lambda})^{\lambda/(\lambda+1)}, \quad (7)$$

where θ_r is the residual soil moisture, θ_s is the saturated soil moisture, α is the inverse of the bubbling pressure, and λ is the pore-size distribution parameter. Eqs. (6) and (7) provide an analytical solution for the surface soil moisture as a function of water-table depth and soil-hydrologic parameters.

The second model component relates the surface soil moisture to the threshold friction velocity. Chepil (1956) developed the first empirical relationship between these variables. He obtained

$$u_{*t} = \left(u_{*td}^2 + \frac{0.6}{\rho} \left(\frac{\theta_{z=d}}{\theta_w} \right)^2 \right)^{1/2}, \quad (8)$$

where u_{*td} is the dry threshold friction velocity, ρ is the density of air (1.1 kg/m^3), and θ_w is the wilting-point moisture content (typically 0.2–0.3 for fine-grained soils (Rawls et al., 1992)). Although more sophisticated models have since been developed for the role of soil

Relative changes in saltation flux, given by Eq. (13), are also expected to apply to dust emissions because of the proportionality between saltation and dust emissions observed in many areas (Gillette et al., 2003). Dust emissions can also be explicitly calculated using Eq. (13) if an estimate is available for the K factor, or the ratio of the vertical dust flux to the horizontal saltation flux. The value of K depends primarily on the surface texture and must be determined empirically.

3. Model calibration and example application

Three sites at the margins of Soda (dry) Lake, California (Fig. 1), were selected for model calibration based on the availability of CLIM-MET data collected from 1999–present by a team from the US Geological Survey (see US Geological Survey, 2004a) for raw data and further information on measurement techniques). Soda Lake is located at the western edge of the Mojave National Preserve just south of Baker, California. Three CLIM-MET stations are available on the northern, southwestern, and southeastern margins of the playa. The Balch and Crucero stations are particularly important because they measure saltation activity near Kelso and Mojave River washes. Sand from these washes can initiate dust entrainment from the floor of Soda (dry) Lake under southerly winds.

The water table beneath Soda Lake is at or near the ground surface along the western edge of the playa, deepening to the east to 20 m and lower beneath the alluvial fans on the

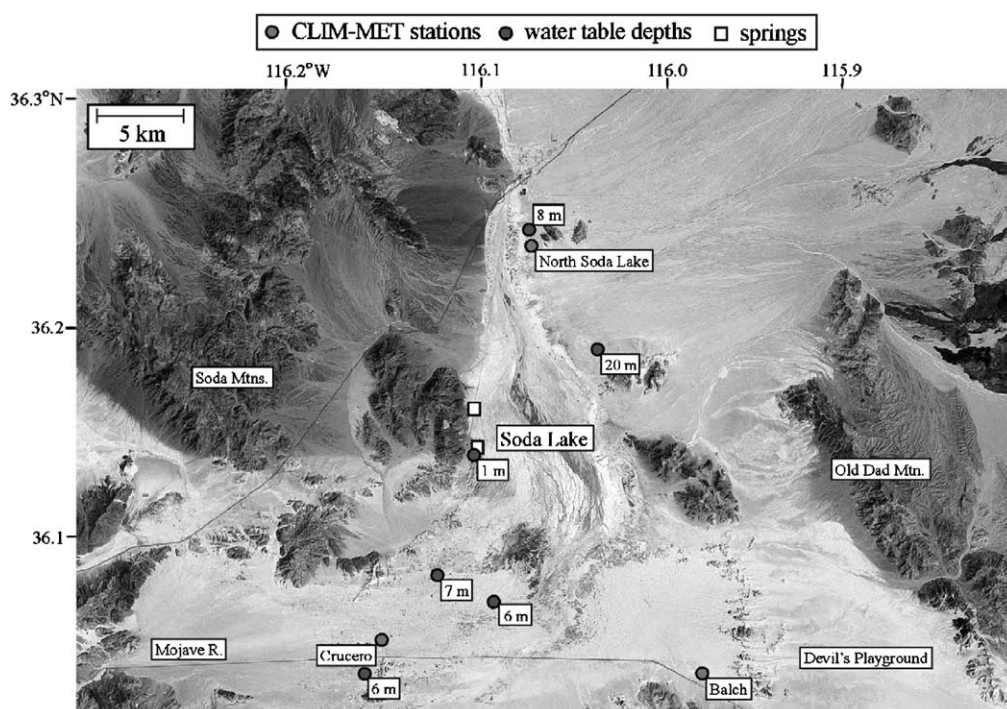


Fig. 1. LANDSAT image of Soda (dry) Lake study site, with locations of CLIM MET stations and water table depths indicated.

eastern side of the basin. Water-table depths indicated in Fig. 1 were obtained from the US Geological Survey National Groundwater Database (US Geological Survey, 2004b).

Fig. 2 illustrates the CLIM-MET station data for hourly rainfall, soil moisture, peak wind speed, and the number of particles in saltation measured at the Balch and Crucero stations. Figs. 2B and E illustrate that the soil moisture at both sites has a residual value of $\theta_r = 0.05$ (Table 1), and that the soil moisture is within a few percent of that value most of the time. For this reason, the steady-state approximation is an appropriate estimate for long-term-average moisture conditions, although it does not represent transient effects of moisture in the days to weeks following rare precipitation events.

Wind speeds measured 2 m above the ground were converted to friction velocities using Eq. (10) with $z_0 = 0.005$ m. This value was obtained from Marticorena et al.’s (1997) relationship $z_0 = 0.005h_c$, together with a canopy height of $h_c = 1$ m. Friction velocities inferred from the measured wind speed data were fit to the two-parameter Weibull distribution. The best-fit parameters obtained for the Balch and Crucero stations are $\beta = 0.398$ and 0.405 , and $\gamma = 2.17$ and 2.15 , respectively. Based on these numbers, we chose $\beta = 0.40$ and $\gamma = 2.15$ as representative values for the meteorological conditions at Soda Lake (Table 1). The dry threshold friction velocities varied from 0.5 to 0.8 m/s at the three CLIM-MET stations. We chose a value of $u_{*td} = 0.5$ for our calculations, but clearly a spatially-distributed model that resolves variations in threshold friction velocity would be the most accurate approach for characterizing the playa basin as a whole.

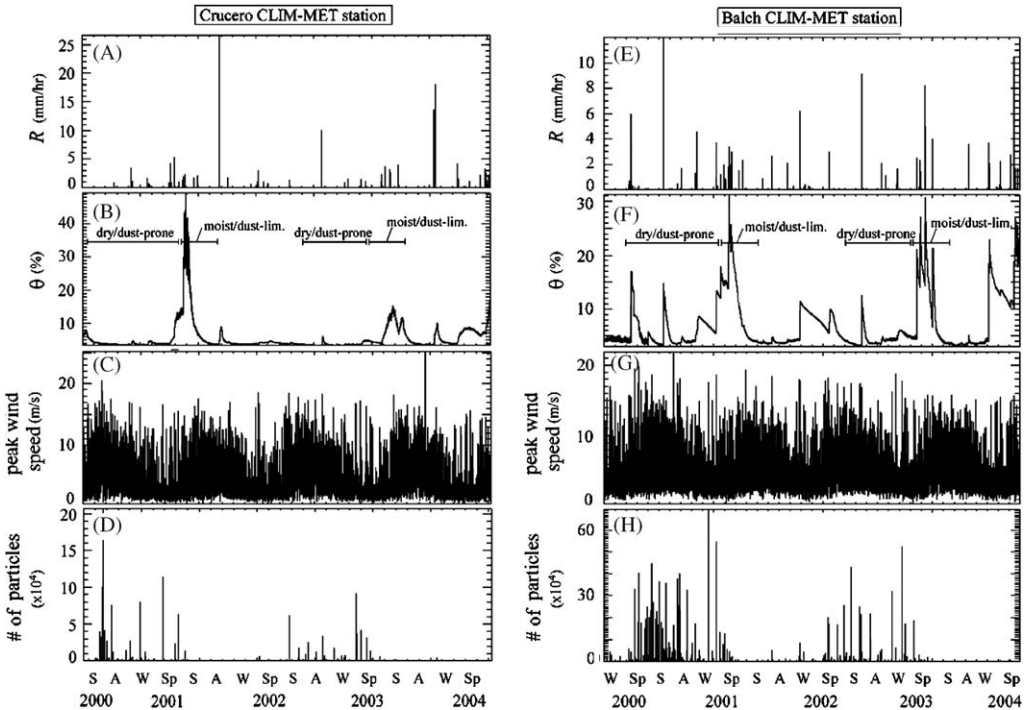


Fig. 2. Hourly CLIM MET data from (A)–(D) Crucero and (E)–(H) Balch stations. (A) and (E) Rainfall, (B) and (F) volumetric soil moisture, (C) and (G) peak wind speed at 2 m above ground, (D) and (H) number of particles in saltation, as measured by SENSIT instruments.

Table 1
Reference hydrological and meteorological parameters for Soda Lake

	Soda lake
b (m ²)	0.05
α (1/m)	0.3
λ	0.2
θ_s	0.5
θ_r	0.05
θ_w	0.2
γ	2.15
β (m/s)	0.40
u_{*td} (m/s)	0.5
$u_{*td,min}$ (m/s)	0.5
$u_{*td,max}$ (m/s)	0.8
z_0 (m)	0.005

Soil-hydrologic parameters were estimated from values given in Gardner and Fireman (1958) and Rawls et al. (1992). Gardner and Fireman (1958) studied soils with fine sandy loam and clay textures, and obtained b values of 0.04 and 0.055 m², respectively. Rawls et al. (1992) provided estimates of α and λ appropriate for fine-grained soils. Representative values of $\alpha = 0.3/\text{m}$, $\lambda = 0.2$, and $\theta_w = 0.2$ were chosen.

Figs. 3A–C illustrate the solution to Eqs. (6), (13), and (12), respectively, for a range of water-table depths up to 10 m, using the model parameters in Table 1. Fig. 3C indicates that saltation (and hence dust emissions) is essentially absent for water tables within 4 m of the surface for this set of parameters. As the water-table depth increases, saltation flux also increases, asymptotically approaching a maximum value of nearly 6 g/m²/s. For water tables deeper than 10 m, the surface is dry enough that soil moisture plays a relatively minor role. The shape of the saltation curve depends primarily on the value of the wilting point moisture θ_w . Fig. 3D, for example, illustrates flux curves for representative end-member values of 0.2 and 0.3. A larger wilting-point moisture means a smaller role for soil moisture in suppressing emissions. The $\theta_w = 0.3$ case, therefore, has saltation initiated at a shallower water-table depth (2 m instead of 4 m), and rises more rapidly to its asymptotic value as a function of water-table depth. In contrast, saltation curves are relatively insensitive to the values of b , α and λ . Varying each of these parameters by 10%, for example, results in flux changes of only a few percent for any particular water-table depth.

Fig. 4 illustrates the sensitivity of the saltation curve to changes in the dry threshold friction velocity and the mean and variability of wind speeds. Although likely future changes in regional wind speeds cannot be easily quantified, many global climate models suggest that wind speeds will become more variable in the future (IPCC, 2001). This type of scenario should be considered as a possibility within future air-quality management plans. Fig. 4A illustrates the saltation flux as a function of water-table depth corresponding to a 10% decrease in the dry threshold friction velocity. This 10% decrease causes a proportionate increase in saltation flux for all water-table depths. A 10% increase in the Weibull scale factor β (closely related to mean wind speed), shown in Fig. 4B, results in a near doubling of saltation flux for most water-table depths. This result is not surprising given the nonlinear, threshold dependence on saltation flux on friction velocity

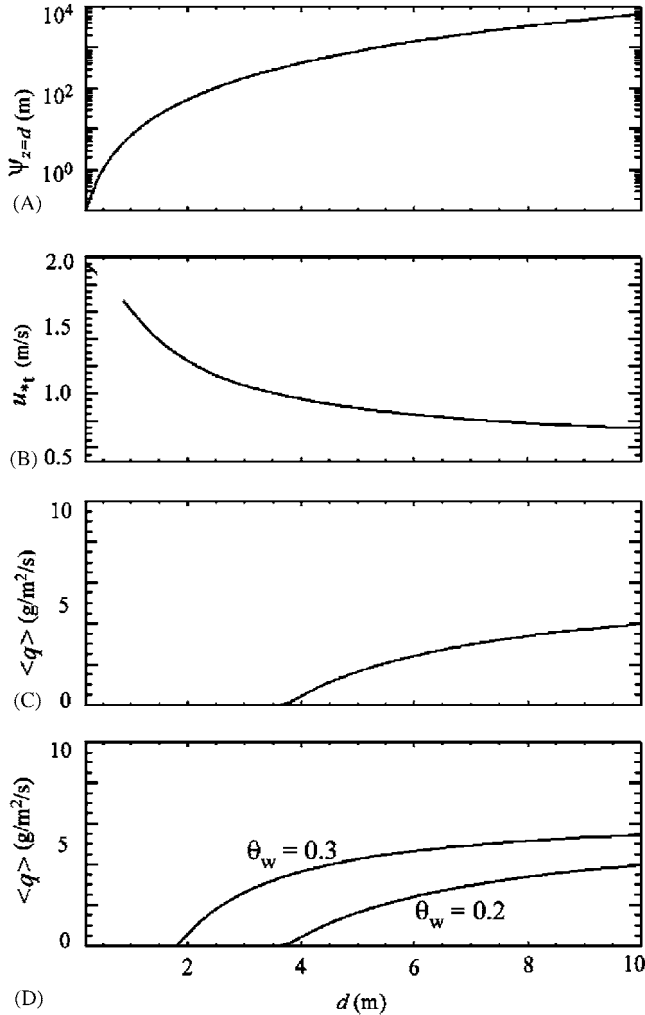


Fig. 3. Solutions to (A) Eq. (6), (B) Eq. (13), and (C) Eq. (12) for the model parameters in Table 1. (D) Sensitivity to the value of the wilting point moisture.

in Eq. (9). A 10% change in the Weibull shape factor γ leads to a small but significant flux response ($\approx 20\%$) for deep water tables.

4. Including microsurficial variability and a range of threshold wind velocity

Field measurements of saltation activity indicate that threshold friction velocities are variable in time (e.g. Gillette et al., 1980, 1997; Chavez et al., 2002). This variability can occur for many reasons, including limited availability in transportable material, short-term bursts in near-surface turbulence, temporal changes in microsurficial characteristics (i.e. formation and disturbance of protective crusts), and the selective entrainment of fine particles and subsequent surface armoring with coarse lag deposits. In the absence of

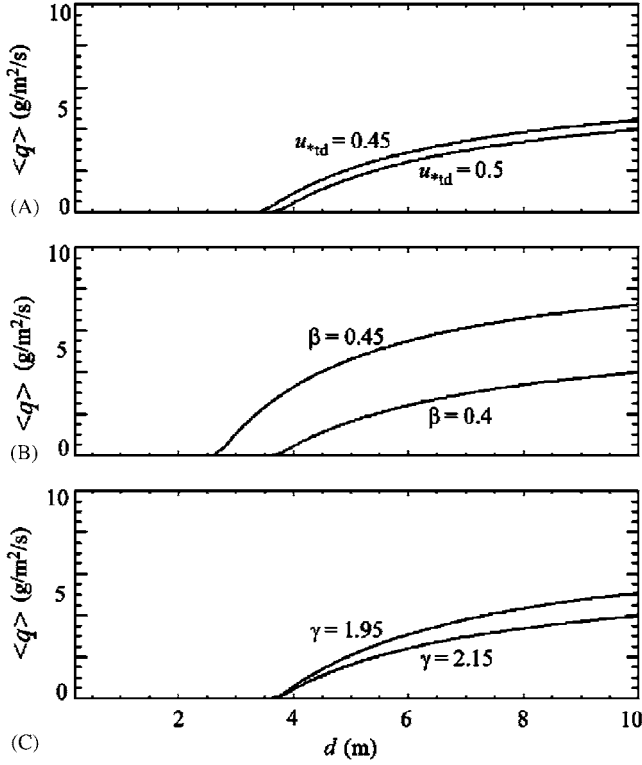


Fig. 4. Sensitivity of saltation fluxes to changes in (A) dry threshold friction velocity, (B) Weibull scale factor, and (C) Weibull shape factor, for a range of water table depths.

detailed quantitative observations of controlling surficial characteristics, a stochastic model component is necessary to represent this variability. In this final section of the paper, we generalize the model equations to include a range in threshold wind velocities, while maintaining the ability of the model to yield closed-form analytic solutions.

Figs. 5A–C illustrates the variability in threshold velocities in the CLIM-MET station data. In this figure, soil moisture is plotted as function of wind speed, with saltating conditions indicated by black dots and non-saltating conditions indicated by gray dots. These data illustrate that high wind speeds occasionally fail to produce saltating conditions. Conversely, low wind speeds can sometimes trigger saltation. Subsetting the CLIM-MET data at time intervals of a few months does not significantly reduce this overlap. The range of threshold friction velocities at these locations, therefore, appears to be related to microsurficial changes that occur over intra-annual time scales.

The CLIM-MET station data support a linear relationship between excess friction velocity and the probability of saltation, as shown in Figs. 5D–F. Mathematically, this can be expressed as a linear increase in the probability of saltation p from a minimum value of 0 at $u = u_{*td,min}$ to a maximum value of 1 at $u_{*td,max}$

$$p = \frac{u_* - u_{*td,min}}{u_{*td,max} - u_{*td,min}}, \quad (16)$$

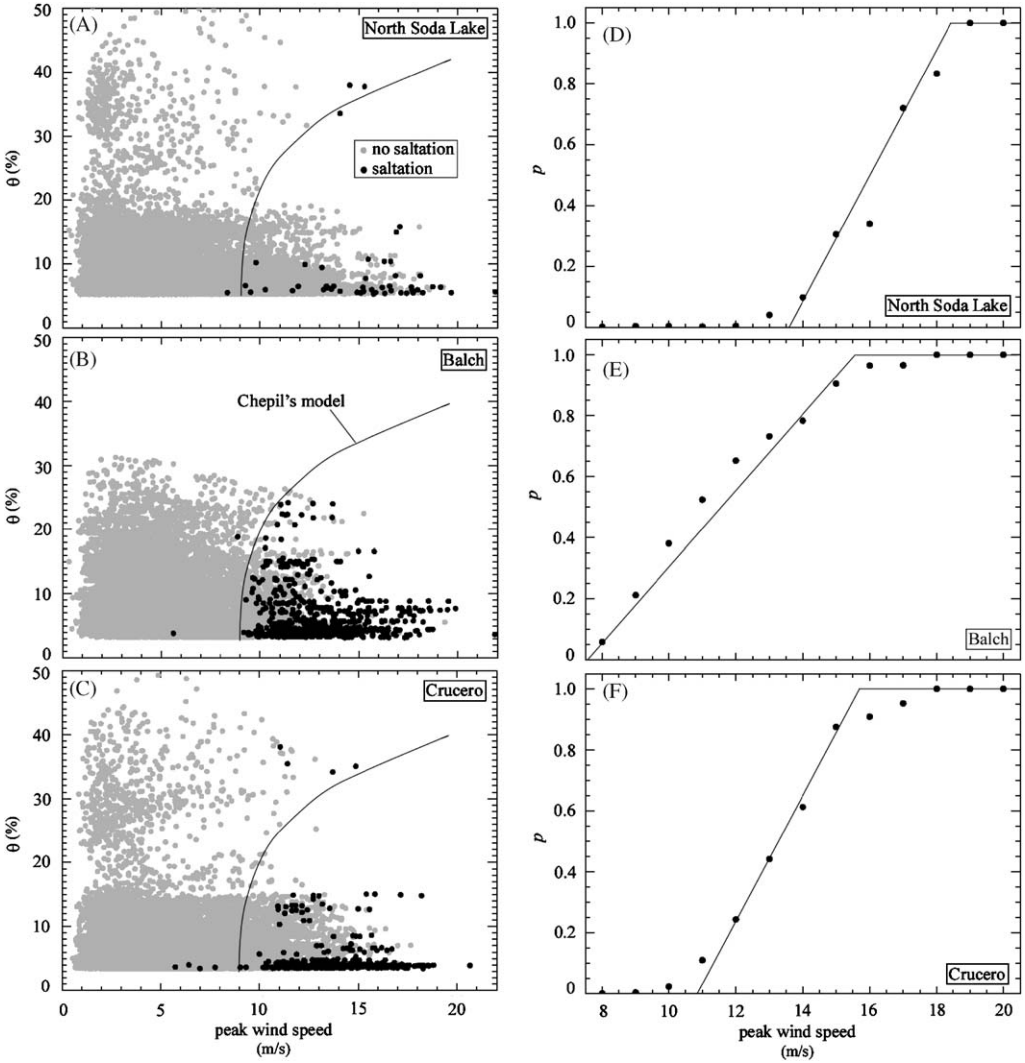


Fig. 5. (A) (C): control on saltation activity by wind speed and soil moisture at (A) North Soda Lake, (B) Balch, and (C) Crucero CLIM MET stations. Saltation activity is indicated with black dots; gray dots indicate no saltation. Chepil's quadratic relationship between soil moisture and threshold friction velocity is also shown. (D) (F): the frequency of saltation activity at a given wind speed shows a linear increase from a minimum threshold velocity to a maximum threshold velocity.

where $u_{*td,min}$ and $u_{*td,max}$ define a range of threshold friction velocities. For a surface that experiences minor microsurficial variability through time, the difference between $u_{*td,min}$ and $u_{*td,max}$ will be small. Conversely, large surficial changes will result in a correspondingly large range of values. Among the three CLIM-MET stations, North Soda Lake and Crucero (Figs. 5D and F) exhibit a relatively small range of threshold velocities, while Balch (Fig. 5E) exhibits a relatively large range.

The range of threshold friction velocities can be included in the model by integrating Eq. (9) in a piece-wise manner

$$\langle q \rangle = \frac{\rho}{g} \left(\int_{u_{*t,\min}}^{u_{*t,\max}} du_* p(u_*) f_w(u_*) u_* (u_*^2 - u_{*t}^2) + \int_{u_{*t,\max}}^{\infty} du_* f_w(u_*) u_* (u_*^2 - u_{*t}^2) \right), \quad (17)$$

to obtain

$$\langle q \rangle \approx \frac{\rho}{g} \frac{\beta}{\gamma^2} (6\beta^2 - u_{*t,\max}^2 + 2(u_{*t,\max} - u_{*t,\min})^2). \quad (18)$$

The incomplete gamma functions have been approximated as unity in Eq. (18) to yield an expression analogous to Eq. (15). The additional terms in Eq. (18) were found to have a minor effect on the dependence of saltation on water-table depth (e.g. Figs. 3 and 4) because the additional terms in Eq. (18) are related directly to wind speed rather than soil moisture. Eq. (18) does, however, provide a more accurate estimation for the absolute value of the saltation flux than Eq. (15), because it explicitly represents the range of threshold wind velocities observed in CLIM-MET station data.

5. Summary and conclusions

We constructed a process-based numerical model to couple soil moisture in the unsaturated zone with saltation activity and dust emissions at the surface. Under steady-state conditions, analytical solutions to this model illustrate that water-table depths of 3–10 m represent a critical range over which small variations in the water-table depth may lead to large, nonlinear changes in saltation activity and dust emissions. Our model is designed as a practical tool for determining the impact of climatic and anthropogenic changes on dust activity in playa basins. Future work will focus on the dynamic effect of soil moisture following individual precipitation events and seasonal cycles, and the influence of vapor-phase transport on the surface soil moisture.

Acknowledgments

Pelletier gratefully acknowledges funding from the US Army Research Office Terrestrial Science Program, Grant no. W911NF-04-1-0266, and the US Geological Survey Earth Surface Processes Program. Ty Ferre, David Thomas, and an anonymous reviewer provided helpful reviews.

References

- Bach, A.J., Brazel, A.J., Lancaster, N., 1996. Temporal and spatial aspects of blowing dust in the Mojave and Colorado deserts of southern California, 1973–1994. *Physical Geography* 17, 329–353.
- Bowden, G.J., Barker, P.R., Shestopal, V.O., Twidell, J.W., 1983. The Weibull distribution and wind power statistics. *Wind Energy* 7, 85–98.
- Brazel, A.J., Nickling, W.G., 1987. Dust storms and their relation to moisture in the Sonoran Mojave Desert region of the Southwestern United States. *Journal of Environmental Management* 24, 279–291.

- Chavez, P.S., MacKinnon, D.J., Clow, G., Tigges, R., Urban, F., Fulton, R., Reheis, M., Miller, D., Bultman, M., Reynolds, R.L., 2002. Monitoring dust emission in the southwest US – interannual differences related to climatic variability. *Geological Society of America Programs with Abstracts* 34, 246.
- Chepil, W.S., 1956. Influence of moisture on erodibility of soil by wind. *Proceedings of the Soil Science Society of America* 20, 288–292.
- Claiborne, C.S., Finn, D., Larson, T.V., Koenig, J.Q., 2000. Windblown dust contributes to high PM_{2.5} concentrations. *Journal of the Air & Waste Management Association* 50, 1440–1445.
- Cornelius, W.M., Gabriels, D., 2003. The effect of surface moisture on the entrainment of dune sand by wind: an evaluation of selected models. *Sedimentology* 50, 771–790.
- Gardner, W.R., 1958. Some steady state solutions of the unsaturated moisture flow equations with application to evaporation from a water table. *Soil Science* 85, 228–232.
- Gardner, W.R., Fireman, M., 1958. Laboratory studies of evaporation from soil columns in the presence of a water table. *Soil Science* 85, 244–249.
- Gillette, D.A., Adams, J.B., Endo, A., Smith, D., Kihl, R., 1980. Threshold velocities for input of soil particles into the air by desert soils. *Journal of Geophysical Research* 85, 5621–5630.
- Gillette, D.A., Hardebeck, E., Parker, J., 1997. Large scale variability of wind erosion mass flux rates at Owens Lake 2. Role of roughness change, particle limitation, change of threshold friction velocity, and the Owen effect. *Journal of Geophysical Research* 102, 25,989–25,998.
- Gillette, D.A., Ono, D., Richmond, K., 2003. A combined modeling and measurement technique for estimating windblown dust emissions at Owens (dry) Lake, California. *Journal of Geophysical Research* 109, doi: 10.1029/2003JF000025.
- Holcombe, T.L., Ley, T., Gillette, D.A., 1997. Effects of prior precipitation and source area characteristics on threshold wind velocities for blowing dust episodes, Sonoran Desert 1948–1978. *Journal of Applied Meteorology* 36, 1160–1177.
- Intergovernmental Panel on Climate Change (IPCC), 2001. *Climate Change 2001: The Scientific Basis*. Cambridge University Press, New York.
- Lancaster, N., Helm, P., 2000. A test of a climatic index of dune mobility using measurements from the southwestern United States. *Earth Surface Processes and Landforms* 25, 197–207.
- Littmann, T.J., 1991. Dust storm frequency in Asia: climatic control and variability. *International Journal of Climatology* 11, 393–412.
- Liverman, D., Meredith, R., 2002. Climate and society in the US Southwest: the context for a regional assessment. *Climate Research* 21, 199–218.
- Marticorena, B., Bergametti, G., Gillette, D., Belnap, J., 1997. Factors controlling threshold friction velocity in semiarid and arid areas of the United States. *Journal of Geophysical Research* 102, 23,277–23,287.
- McTainsh, G.H., Lynch, A.W., Tews, E.K., 1998. Climatic controls upon dust storm occurrence in eastern Australia. *Journal of Arid Environments* 39, 457–466.
- Okin, G., Reheis, M., 2002. An ENSO predictor of desertification in the southwestern United States. *Geophysical Research Letters* 29, doi: 10.1029/2001GL014494.
- Rawls, W.J., Ahuja, L.R., Brakensiek, D.L., Sirmohammadi, A., 1992. Infiltration and soil water movement. In: Maidment, D.R. (Ed.), *Handbook of Hydrology*. McGraw Hill, New York, NY, pp. 5.1–5.62.
- Reheis, M.C., Budahn, J.R., Lamothe, P., 2002. Geochemical evidence for diversity of dust sources in the southwestern United States. *Geochimica et Cosmochimica Acta* 66, 1569–1587.
- Samet, J.M., Dominici, F., Currier, F.C., Cousac, I., Zeger, S.L., 2000. Fine particulate air pollution and mortality in 20 US cities, 1987–1994. *New England Journal of Medicine* 343, 1742–1749.
- Shao, Y., Raupach, M.R., 1993. Effect of saltation bombardment on the entrainment of dust by wind. *Journal of Geophysical Research* 98, 12,719–12,726.
- Takle, E.S., Brown, J.M., 1978. Note on use of Weibull statistics to characterize wind speed data. *Journal of Applied Meteorology* 17, 556–559.
- U.S. Environmental Protection Agency, 2004. Particulate matter (PM₁₀) attainment designations in region 9. <http://www.epa.gov/region09/air/maps/r9_pm10.html>.
- U.S. Geological Survey, 2004a. Earth surface dynamics program CLIM MET data. <http://climweb.cr.usgs.gov/info/sw/clim_met>.
- U.S. Geological Survey, 2004b. National water information system. <<http://waterdata.usgs.gov/ca/nwis/gw>>.
- Van Genuchten, M.Th., 1980. A closed form equation for predicting the hydraulic conductivity of unsaturated soils. *Soil Science Society of America Journal* 44, 892–898.

- Vedal, S., 1997. Ambient particles and health: lines that divide. *Journal of the Air & Waste Management Association* 47, 551–581.
- Warrick, A.W., 1988. Additional solutions for steady state evaporation from a shallow water table. *Soil Science* 146, 63–66.
- Watson, J.G., 2002. Visibility: science and regulation. *Journal of the Air & Waste Management Association* 52, 628–713.
- Yu, B., Hesse, P.P., Neil, D.T., 1993. The relationship between antecedent regional rainfall conditions and the occurrence of dust events at Mildura, Australia. *Journal of Arid Environments* 24, 109–124.

Relief threshold for eolian sand transport on alluvial fans

Joseph P. Cook¹ and Jon D. Pelletier¹

Received 29 June 2006; revised 23 November 2006; accepted 15 February 2007; published 30 May 2007.

[1] Many arid alluvial-fan terraces downwind from eolian sand sources exhibit an abrupt increase in eolian epipedon thickness and sand content below a critical elevation which varies from fan to fan. Above this elevation, sand accumulates locally and is not transported across the fan. Below this elevation eolian sand from nearby playa and channel sources is readily transported across the distal fan. Here we test the hypothesis that these distal-fan eolian “corridors” are controlled by a threshold fan-surface relief. We propose that when along-strike relief falls below a critical threshold value, an eolian surface of transportation or “corridor” develops. To test this hypothesis, we measured multiple along-strike topographic profiles and eolian epipedon textures on two piedmonts in the Ivanpah Valley and adjacent Hidden Valley in Clark County, Nevada. Both piedmonts are located near sand-dominated playas and exhibit clear evidence of eolian transport across their distal fan regions. The near-surface boundary layer flow above each topographic profile was quantified using the multispectral finite difference (MSFD) numerical model. This model predicts the surface shear stress above complex terrain for any wind condition assuming neutrally stable flow. The minimum shear stress calculated by MSFD for each profile during extreme wind conditions was compared to the shear-velocity threshold necessary to initiate saltation. Model results showed that in proximal fan areas, along-strike relief was large enough to prevent eolian transport of all but fine sand particles. In distal fan profiles within the eolian corridor, model results predict shear stresses everywhere above threshold for both fine and coarse sand.

Citation: Cook, J. P., and J. D. Pelletier (2007), Relief threshold for eolian sand transport on alluvial fans, *J. Geophys. Res.*, 112, F02026, doi:10.1029/2006JF000610.

1. Introduction

[2] Alluvial fan formation has characteristically been described in terms of primary (depositional) and secondary (surficial reworking) fluvial processes [Blair and McPherson, 1994]. In arid environments, eolian processes can constitute a third process significant in fan evolution. Portions of alluvial fans and piedmonts located downwind from eolian sources are subjected to repeated transport of windblown sediment across their surfaces. The amount of windblown sediment deposited on piedmonts is a function of distance from sediment sources, prevailing wind directions, and the vegetation and relief of the substrate. While particles smaller than about 60 μm can enter suspension and be deposited far from the location of entrainment [Pelletier and Cook, 2005], larger sand-sized grains are transported primarily by saltation and are limited to transport within about 2 m of the surface [Reheis, 1999; Greeley and Iversen, 1985; Marticorena and Bergametti, 1995]. For this reason, sand-dominated eolian transport may be limited to pathways where surface roughness (i.e., pavement and vegetation) and relief are continuously low enough for entrainment to occur. The purpose of

this study is to quantify the threshold conditions for transport of fine and coarse sand on alluvial fans using a numerical model and to test the model predictions at two playas in Clark County, Nevada.

[3] Late Cenozoic cutting-and-filling cycles have produced nested terraces on many fans that rise like a flight of stairs from the active channel. These stairs are characterized by a systematic decrease in along-strike fan-surface relief from the head to toe of the fan. The degree of channel entrenchment decreases with distance from the fan apex as the terrace treads of older fan surfaces and the active channel converge. Here we test our hypothesis that when located near a source of sandy material, portions of the fan surface exhibiting low relief allow eolian transport by saltation, resulting in a swath of deposition of sandy material across the distal fan surface. In contrast, we propose that zones of greater relief in the proximal fan region serve as traps for saltating material, thereby inhibiting eolian deposition across the fan surface. Because the gradient between fan terraces and active channels converges at a similar rate across the fans observed in this study, the threshold relief and resulting swath of eolian deposition by saltation approximately follows contour (Figures 1b–1e). Fine-grained sediment in channels transported by fluvial processes into zones of lower relief is also available for transport by saltation. This same sediment in the higher-relief zone of the fan is sheltered from winds that could

¹Department of Geosciences, University of Arizona, Tucson, Arizona, USA.

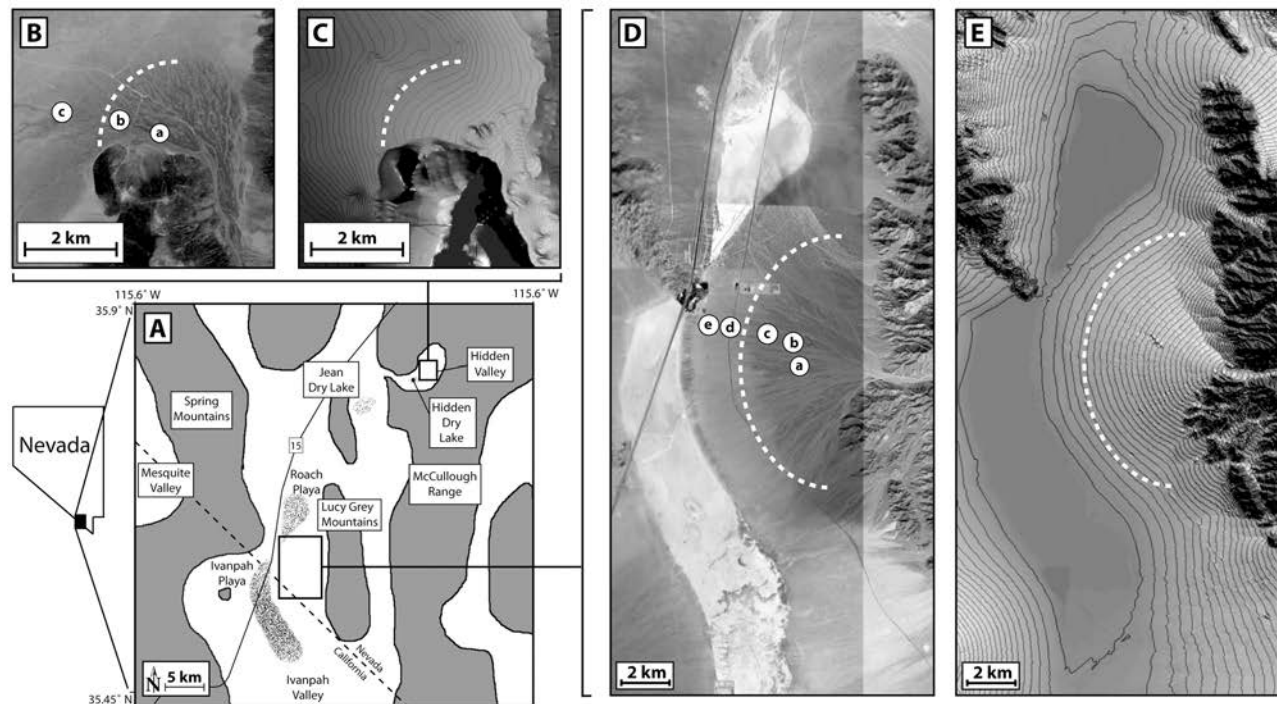


Figure 1. (a) Location map of Ivanpah and Hidden Valley field areas, Clark County, Nevada. (b–e) Quickbird and shaded relief image with topographic contour line overlay for the Hidden Valley and Lucy Grey Fans. Lettered circles correspond with measured topographic profile locations shown in Figures 4 and 5. The dashed line in each figure represents the upper boundary of the observed eolian corridor. Below this boundary, sand-dominated eolian transport occurs everywhere. Above this boundary, saltation is inhibited by higher fan relief and occurs only locally, perhaps only under extreme wind conditions.

otherwise exert sufficient shear stress to initiate saltation of material from channel to terrace.

[4] While research has been devoted to accurately measuring threshold sediment mobilization values in the field [Marticorena *et al.*, 1997a, 1997b; Lancaster and Baas, 1998] and using field-collected data [Pelletier, 2006], the majority of studies have taken place in wind tunnels under controlled conditions [Raupach, 1992; Dong *et al.*, 2002; Hagen, 1999; Nishimura and Hunt, 2000]. Our study combines the multispectral finite difference (MSFD) model with natural particle size and wind data to realistically model boundary layer surface flow over alluvial fan topography. Our approach blends laboratory-tested sediment transport equations with numerical modeling calibrated with field data to predict where saltation is able to operate most effectively under natural conditions.

2. Study Area and Field Observations

[5] Our study area is located in both Ivanpah and Hidden Valley along the western front of the Lucy Grey and McCullough Ranges in Clark County, Nevada near the California border (Figure 1a). Each valley contains an alluvial fan located in close proximity to one or more playas. In Ivanpah Valley, a large fan sourced from the Lucy Grey Mountains terminates adjacent to both Roach Lake and Ivanpah Playa (Figure 1a). Our second study site in Hidden Valley is located approximately 30 km to the

northeast of Ivanpah Playa. Here a smaller fan sourced from the McCullough Range grades toward Hidden Dry Lake (Figure 1b). Both fans exhibit a swath of eolian deposition on their distal reaches where relief between terrace and active channel is lower relative to proximal portions of the fan. Here we use “proximal” and “distal” to describe location within the piedmont, not proximity to the source of eolian sediment (i.e., playas). A series of playas, sand ramps, and an overall drape of sandy, windblown material links multiple valleys in this portion of Nevada, forming a large-scale eolian “corridor” (K. House, personal communication).

[6] Abandoned terraces on both fans exhibit varying degrees of pavement maturity, rock varnish development, remnant microtopography, and planarity depending on age of deposition. The oldest terraces stand highest on the fan; younger terraces are inset into older alluvium, demonstrating the traditional sequence of quaternary fan terraces commonly observed in the southwestern United States [Bull, 1991]. The overall relief between abandoned terrace and active channel decreases from proximal to distal fan. The overall quality of desert pavement on all aged surfaces abruptly diminishes upon entering the “corridor” zone due to the high fluxes of windblown sand passing across lower relief portions of the fan. Terraces straddling this boundary exhibit well-varnished pavements with nearly complete interlocking clast coverage upfan from the boundary, and progressively more degraded, sparse clast coverage moving downfan, yielding to sandier deposition downfan from the boundary.

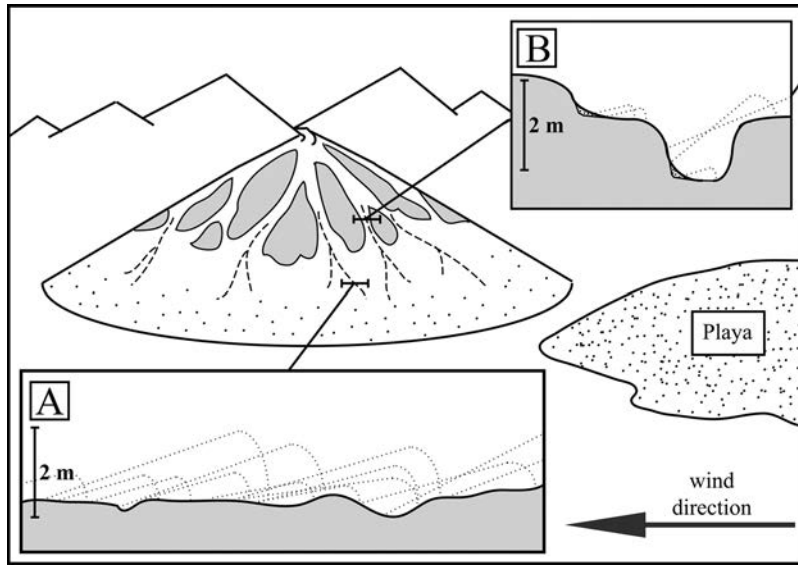


Figure 2. Schematic diagram of fan profiles. (a) Example of distal fan profile. Dashed lines represent grain saltation trajectories unimpeded by low fan relief. (b) Example of midproximal fan profile. Here saltating grains become trapped in high relief areas between channel and terrace. Traps accumulate windblown sand which can be remobilized under extreme wind conditions or transported downfan by fluvial processes.

[7] To accurately represent topography and relative relief from proximal to distal fan for input to MSFD modeling, profiles spanning multiple terrace ages were measured on each fan normal to the channel orientation. Profiles were measured using a tripod-mounted total station positioned on a highstanding terrace to ensure uninterrupted line-of-sight with the pole-mounted prism. Profile point spacing averaged approximately 2 m, although smaller transect steps were used where detailed topography was encountered. While overall relief between active channel and abandoned terrace increased from distal to proximal fan (Figure 2), some variation in this trend was observed. This is reflected in our transect data by portions of transects from the middle to upper fan exhibiting slightly higher relief than transects conducted higher on the fan. This reversal from the expected trend is minor and occurs only locally.

3. Model Description

3.1. Boundary Layer Model Component

[8] In order to compute the turbulent shear stresses over different fan profiles, we developed a numerical modeling code based on the mixed-spectral finite difference (MSFD) code developed and tested by *Walmsley et al.* [1982], *Beljaars et al.* [1987], *Xu and Taylor* [1995], *Karpik et al.* [1995], and *Taylor* [1998]. MSFD is a boundary layer model that solves the Reynolds-stress equations for boundary layer flow over arbitrary topography and surface roughness. The advantage of the model is its computational speed and ease of use. A limitation of the model, however, is that it does not calculate the detailed flow structure of recirculation zones behind topographic obstacles and it loses accuracy for rapidly varying topography and surface roughness. MSFD has been applied to other problems in eolian geomorphology by *Howard* [1978].

[9] MSFD works on a uniformly spaced grid in the horizontal direction and a logarithmically spaced, terrain-following grid in the vertical direction. The vertical coordinate is given by the local distance above the ground surface, $Z = z - f$, where f is the local ground-surface height. Grid points in the vertical direction range from values much lower than the roughness length, z_0 , to values much greater than the topographic relief. For example, if z_0 is 0.01 m and the total relief of the profile is 2 m, a reasonable set of values for the vertical coordinate system is 0.001, 0.00333, 0.01, 0.0333, ... 33.3, and 100 m, for a total of 11 grid points in the vertical direction.

[10] The model solves the linearized Reynolds stress equations assuming mixing-length closure by working in the Fourier, or wave number, domain. The equations for the perturbed velocities and shear stresses in two dimensions (2D) are given by

$$iku_0\hat{u}_1 + \frac{du_0}{dZ}\hat{w}_1 = \frac{1}{\rho}ik\hat{p}_1 + \frac{\partial\hat{\tau}_{x1}}{\partial Z} \quad (1)$$

$$iku_0\hat{w}_1 - ku_0\hat{f}_1 = \frac{1}{\rho}\frac{\partial\hat{p}_1}{\partial Z} \quad (2)$$

$$ik\hat{u}_1 + \frac{\partial\hat{w}_1}{\partial Z} = 0 \quad (3)$$

$$\hat{\tau}_{x1} = 2\kappa(Z + z_0)u_*\frac{\partial\hat{u}_1}{\partial Z} \quad (4)$$

$$u_0 = \frac{u_*}{\kappa} \ln\left(\frac{Z + z_0}{z_0}\right) \quad (5)$$

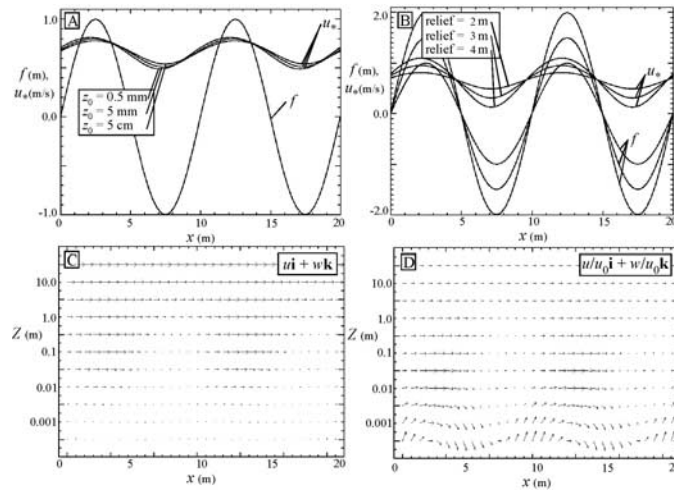


Figure 3. (a) Example of model output over idealized topography (sine wave) with variations in bed roughness. (b) Example of model output over varying topographic relief (sine wave with varying amplitude). Modeled shear velocity patterns are affected to a much greater extent by topographic relief than surface roughness. (c) Vector plot of actual wind velocities at logarithmically spaced heights above the bed as predicted by MSFD modeling. (d) Modeled wind velocities normalized by logarithmic profile to accentuate velocity perturbations near the bed.

where k is the wave number, u and w are the velocities in the horizontal (x) and vertical (z) directions, respectively, p is the pressure, τ_x is the shear stress, f is the topography, u_* is the unperturbed shear velocity, κ is the von Karman constant (0.4), the subscripts 0 and 1 represent the mean and perturbed values for each variable (the mean is the value if the topography was flat), and the hat above each variable indicates a Fourier transform. Each Fourier-transformed variable represents both real and imaginary parts (for example, $\hat{u}_1 = \hat{u}_{1r} + i\hat{u}_{1i}$, where \hat{u}_{1r} and \hat{u}_{1i} are the real and imaginary parts of \hat{u}_1). Equations (1)–(4) represent eight total equations because the real and imaginary part of each variable must be calculated. Equations (1)–(5) are identical to equations (6), (7), and (9) of *Beljaars et al.* [1987] assuming two-dimensional flow. The wind and stress fields for each wave number comprise a one-dimensional (1D) two-point boundary value problem for eight simultaneous ordinary differential equations (ODEs). This type of problem can be solved using a shooting method [*Press et al.*, 1992].

[11] MSFD works with periodic boundary conditions (i.e., the downwind end of the grid wraps around to the upwind end). Due to the Fourier-transformed nature of the model, MSFD works most simply when the number of horizontal grid points is a power of two. If this is the case, fast Fourier transform (FFT) techniques can be directly used to solve the equations with no additional processing. A no-slip boundary condition is enforced at the ground surface (i.e., the velocities and pressures go to zero). Far from the ground, the effects of variable topography and surface roughness variations go to zero. At the upper end of the grid, the perturbed values of all of the model variables go to zero. Mathematically, these boundary conditions are given by

$$\hat{u}_1 = \hat{w}_1 = \hat{p}_1 = 0 \quad \text{at} \quad Z = 0 \quad (6)$$

$$\hat{u}_1 = \hat{w}_1 = \hat{p}_1 = \hat{\tau}_1 = 0 \quad \text{at} \quad Z = \infty \quad (7)$$

In the model, the boundary conditions at $Z = 0$ are enforced at some very small distance from the ground (i.e., $Z = 0.001$ or smaller). Similarly, the upper boundary conditions are enforced at a large distance (for example, $Z = 100$ m for low-relief topography).

[12] The input data required to solve equations (1)–(5) are the topographic profile [Fourier-transformed for use as \hat{f}_1 in equation (2)], the surface roughness z_0 (assumed here to be uniform for each profile), and the unperturbed shear velocity u_* . Topographic profiles surveyed in the field were first preprocessed for input. The profiles were resampled by linear interpolation so that each profile had a number of values equal to a power of two. Second, the profile was made periodic by computing the mirror image of the profile and adding it to the end of the original profile. In this way, a profile with indices from 1 to 256 would become a profile of length 512 with indices 1...256, 256...1. These preprocessing steps enable the input data to be consistent with the periodic boundary conditions used by the model, and they have the effect of minimizing “edge effects.”

[13] Examples of the model output are given in Figure 3 for idealized topography (i.e., a sine wave given by $f = A \sin(2\pi x/\lambda)$), illustrating the sensitivity of model results to variations in bed roughness (Figure 3a) and topographic relief (Figure 3b). In Figure 3a, the topography f is plotted together with the model-predicted values of u_* along each profile. Our “reference” case for these runs uses $z_0 = 5$ mm, $\lambda = 10$ m, $A = 2$ m, and $u_* = 0.67$ (corresponding to 10 m/s at a height 2 m above the ground). Figure 3a also includes the u_* profiles resulting from model runs with z_0 values ten times larger (5 cm) and smaller (0.5 mm) than the reference value. The shear velocities in Figures 3a and 3b follow the sinusoidal topography with the maximum shear velocity located slightly upwind from the crest. The shear velocity pattern depends only weakly on surface roughness, with slightly larger spatial variations and downwind shifts

resulting from rougher beds. The effects of variable relief are shown in Figure 3b. In these cases, the amplitude of the sine wave was varied between $A = 1, 1.5$, and 2 m while keeping all other parameter values the same as in the reference case. These results show that greater relief causes larger spatial variations in shear velocity. In other words, shear stresses are greater above crests and lower above troughs at the relief increases. This suggests that as relief increases, a critical point will eventually be passed where sand cannot be transported through the troughs because the shear velocity falls below the threshold value.

[14] Figures 3c and 3d illustrate vector plots of wind velocity predicted by MSFD for the reference case. Figure 3c illustrates the actual wind velocity at logarithmically spaced heights Z above the bed. Figure 3d illustrates the velocity normalized by the logarithmic profile, which allows for the velocity perturbations close to the bed to be more clearly illustrated (i.e., velocity perturbations increase toward the bed, but the velocity also goes to zero there, so Figure 3d is designed to magnify the bed effects). These figures illustrate the speed-up in velocity over crests associated with flow convergence and the slow-down over troughs caused by flow divergence. This effect extends a distance above the bed roughly equal to the bed relief.

3.2. Effects of Local Topography on Critical Shear Velocity

[15] Variations in topography actually influence eolian transport in two distinct ways. Figure 3b clearly illustrates how topographic variations cause shear-velocity variations. This is a purely aerodynamic effect. The local terrain plays an additional role, however, because movement of sand from a trough requires not only that sand particles be lifted, but that they be lifted with sufficient vertical force to move them uphill. This additional shear stress associated with variations in bed slope was studied by *Hardisty and Whitehouse* [1988]. In their study of sand transport in the Sahara, they endorsed a correction factor proposed by *Dyer* [1986] in which the threshold shear velocity is given by

$$u_{*c} = u_{*c0} \sqrt{\frac{\tan \phi + \frac{\partial f}{\partial x}}{\tan \phi \sqrt{\left(\frac{\partial f}{\partial x}\right)^2 + 1}}} \quad (8)$$

where u_{*c0} is the critical shear velocity for flat terrain and ϕ is the angle of internal friction. The correction factor equals 1 for flat topography, goes below 1 as the downwind bed slope increases (i.e., as $\partial f/\partial x$ becomes more negative), and eventually becomes zero at the angle of internal friction. This behavior is consistent with the fact that very little shear stress is required to transport sand close to the angle of repose. If the downwind bed slope is positive (i.e., sand must move uphill), the threshold shear velocity increases, but more slowly than for the downhill side of the curve.

3.3. Model Calibration

[16] Because no wind gauge data was available for the study areas, wind velocity data for three similarly vegetated piedmonts, twin springs, immigration wash, and oriental

wash (CEMP and RAWs stations, <http://www.wrcc.dri.edu/wraws/nvutF.html>) in Nevada were obtained and processed according to the von Karman-Prandtl “law of the wall”:

$$u_* = \frac{u_z k}{\ln\left(\frac{z}{z_0}\right)} \quad (9)$$

where u_* is shear velocity, u_z is wind velocity measured at height z , k is the Von Karman constant, and z_0 is the roughness length. Although the dominant wind direction for our field areas cannot be inferred from these wind stations, wind directions in the Basin and Range province are generally parallel to the valley aspect (in this case roughly n-s) and reverse seasonally. This direction corresponds to the observed transport and deposition patterns observed in our field areas. Vegetation on both fans is predominantly composed of creosote, saltbush, and Mojave Yucca. To approximate z_0 values we utilized the roughness density approach outlined by *Marticorena et al.* [1997a, 1997b] and *Raupach et al.* [1993]:

$$\lambda = \frac{nbh}{S} \quad (10)$$

where λ is the roughness density, n is the number of roughness elements, b is the mean breadth, h is the mean height, and S is the area being considered. For roughness densities greater than 0.11, z_0 is set equal to $(0.05)h$ [*Marticorena et al.*, 1997a, 1997b; *Raupach et al.*, 1993; *Okin et al.*, 2006]. Average vegetation size and density easily exceeded roughness densities of 0.11 in both field areas. With an average vegetation height of approximately 1 m, a z_0 value of 0.05 m was used for model runs.

[17] Two years of daily average wind velocity data (12 months prior to and following the date of station photos) for three stations was analyzed, and u_* values for winds exceeding the 90th percentile intensities were calculated. This range was chosen in an attempt to identify an “extreme” shear velocity capable of mobilizing significant amounts of sediment, yet occurring with enough frequency to be geomorphically effective [*Wolman and Miller*, 1960]. Percentile wind velocity values for all three wind stations were in close agreement, yielding extreme u_* values ranging from approximately 0.38–0.72 m/s (corresponding with the lowest 90th and highest 99.9th percentile u_* value, respectively). In this paper we choose a u_* value at the low end of this range (0.40 m/s) in order to illustrate the model behavior. Unfortunately, we cannot further constrain the u_* value at our study sites because it is difficult to uniquely choose an “extreme” velocity. Our study sites will experience shear velocities across the full range from 0.38 to 0.72 m/s, but the larger wind speeds may not occur with sufficient frequency to contribute significantly to the overall sand flux.

[18] To accurately determine critical shear velocity for our field areas, channel sediments, proximal and distal fan terrace eolian epipedons, and playa surfaces were sampled and analyzed for particle size distribution. Because many of the samples contained pieces from the eolian epipedon, aggregates were broken up prior to sieving using a mortar and pestle. Samples were separated into 6 size fractions

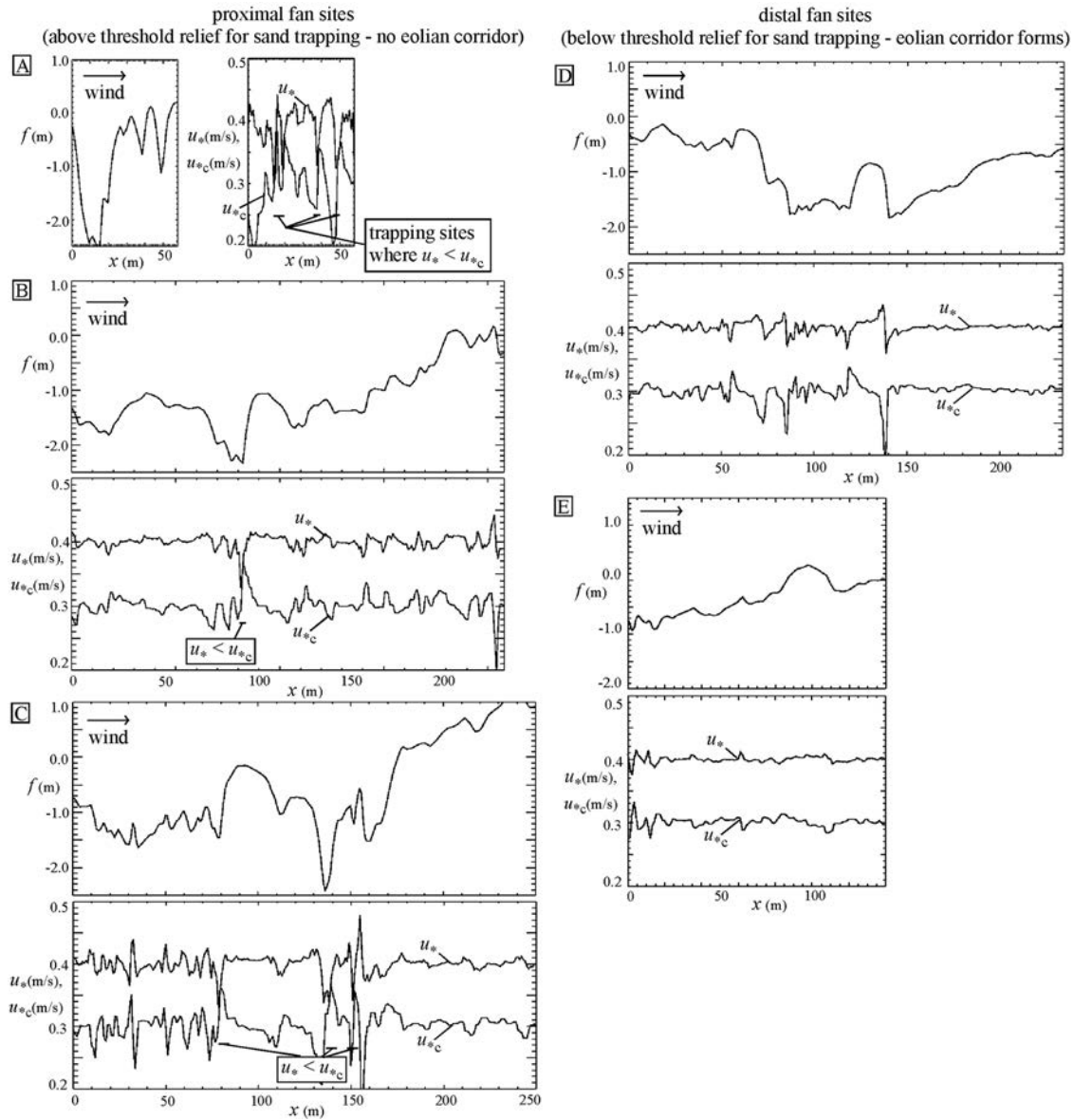


Figure 4. MSFD model results for Lucy Grey field area. In each plot, the upper diagram is the measured topographic profile while the lower plot depicts model results from (a) proximal to (e) distal fan. The top line in each lower plot represents the predicted u_* values along the profile. The bottom line is the predicted u_{*c} value required for sediment transport along the same profile. Where these lines intersect, modeled shear velocities are less than those required to transport sediment, and trapping occurs. Multiple traps exist in (a–c) the proximal fan, potential traps exist where predicted u_* and u_{*c} values nearly intersect in the transitional profile near (d) the eolian corridor boundary, and no trapping occurs in (e) the distal fan where sand transport can occur everywhere.

ranging from very coarse sand (2000–1000 μm) to very fine sand (125–63 μm) and sediment passing through all screens (<63 μm) using a sieve-shaking machine. A grain diameter range of 250–500 μm (medium sand) was chosen for model input based on the absence of medium sand in proximal piedmont deposits compared to channel sediments (Figure 6b). The presence of finer sediments in proximal piedmont as well as channel sediments indicates these sized particles are transported across the entire fan regardless of relief. Larger grains are surely moved, but on a more

infrequent timescale. For model input, u_{*c} was calculated using *Bagnold's* [1941] critical shear velocity calculation:

$$u_{*c} = A \sqrt{\frac{\rho_s}{\rho_a} g D} \quad (11)$$

where A is a constant of proportionality (equal to 0.1 for air), ρ_s is the density of sediment, ρ_a is the density of air, g is the acceleration due to gravity, and D is grain size diameter.

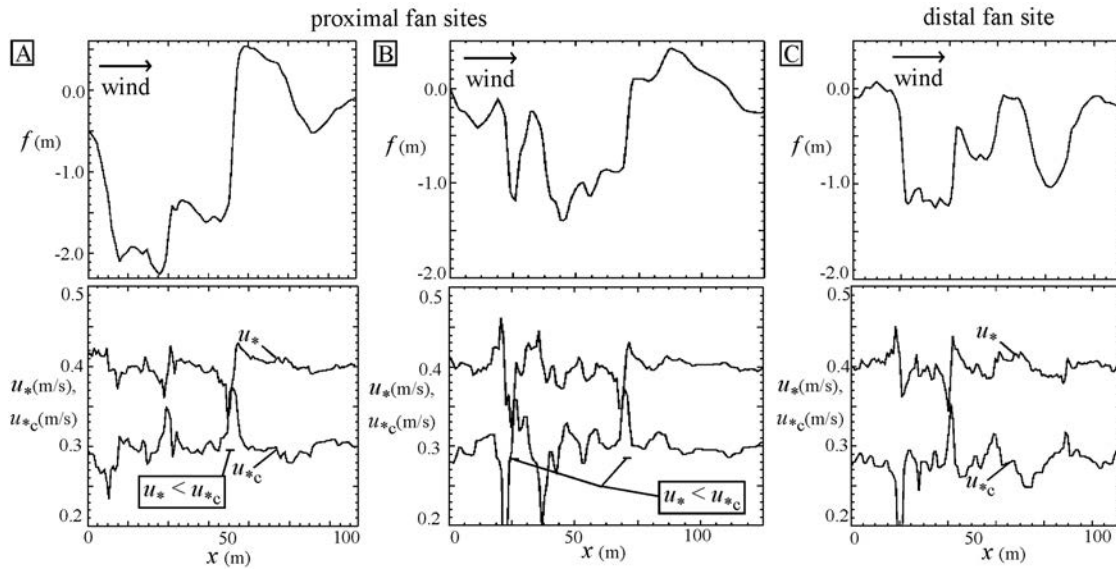


Figure 5. MSFD model results for the Hidden Valley Fan field area. Plots follow the same arrangement as those in Figure 4. Multiple sediment traps exist in (a and b) the upper fan profiles where relief is highest. (c) Although some trapping is still predicted in the lowest profile, overall relief is less than relief measured in Figures 5a and 5b. The rate of change in relief is also important for sediment trapping ability. An abrupt topographic rise inhibits saltation more effectively than a gradual topographic rise of the same relief. For example, a vertical cut bank >1 m effectively stops windblown sediment whereas a gradual slope of similar relief allows saltation to operate.

For medium quartz sand, the critical shear velocity ranges from approximately 0.22 m/s for $D = 250 \mu\text{m}$ to 0.32 m/s for $D = 500 \mu\text{m}$. It is important to note that our use of “critical shear velocity” refers to the shear stress required to initiate saltation, not maintain it (i.e., static, not dynamic shear velocity). Because static shear velocity is greater than dynamic shear velocity, modeled zones of sediment transport may continue to allow saltation at u_* values less than u_{*c} once static shear velocities have been exceeded. Equation (11) has been tested in numerous wind tunnel studies under controlled conditions, including uniform D . Because our study involves heterogeneous natural sediments, the calculated value for u_{*c} may underestimate the true threshold value for our study sites.

3.4. Model Results for the Study Areas

[19] MSFD model runs using field calibrated parameters and measured fan profiles recreate the eolian “corridor” effect at approximately the same fan elevation observed in the study areas. Modeled u_* and u_{*c} values along fan profiles are represented by the uppermost two plots in Figures 4 and 5. Where the upper plot, representing u_* , intersects the lower plot, representing u_{*c} , modeled shear velocity is less than the critical shear velocity required for sediment transport as determined by roughness elements, local slope, and topography. Physically, sand already in transport at these locations along the profile would drop out of transport due to decreased shear velocities owing to flow divergence and locally higher u_{*c} values due to downwind bed slope. In essence, these areas constitute sediment “traps”. Sediment deposited in these traps due to insufficient shear velocity is difficult to remobilize as it is sheltered from winds by locally higher relief and is likely

only susceptible to subsequent eolian transport under extreme wind conditions. High relief profiles provided multiple trapping zones for windblown sediment (Figure 4a) whereas low relief profiles lack traps and allow transport by saltation everywhere, i.e., $u_* > u_{*c}$ along the entire profile (Figure 4e).

[20] The observed onset of eolian deposition on the Lucy Grey Fan occurred very close to our fourth profile downfan (Figure 4d). The model predicts eolian transport across this portion of the fan, with a few locations along the profile which approach trapping topography levels. Pavements in this area of the fan were observed to be degraded compared to similar-age pavements farther up the fan. The locally higher influx of sandy material likely inundates pavement in lower relief portions of the fan, accumulating more rapidly than sediment can be added to the Av horizon beneath pavement clasts. Downfan from the location of this transitional profile, both fine and coarse sand can be transported everywhere along the profile as u_* is uniformly greater than u_{*c} . Although not as clear as the Lucy Grey Fan profiles, model results for the Hidden Valley Fan are similar. Overall relief on the proximal fan profile exceeds 2 m and provides multiple sediment traps (Figure 5a). Lower fan profiles still exhibit a trapping capability, but to a lesser extent in the distal fan.

[21] Contrary to our expected result, percent medium and coarse sand is greater in several transects in the proximal fan compared to those in the distal fan. Grain size distributions from channel sediments exhibit abundant medium to very coarse sand, which designates them as likely sources for the coarse material found in proximal fan deposits (Figure 6b). The abundance of coarse sediment found in fan channels compared to the relative paucity of coarse material observed

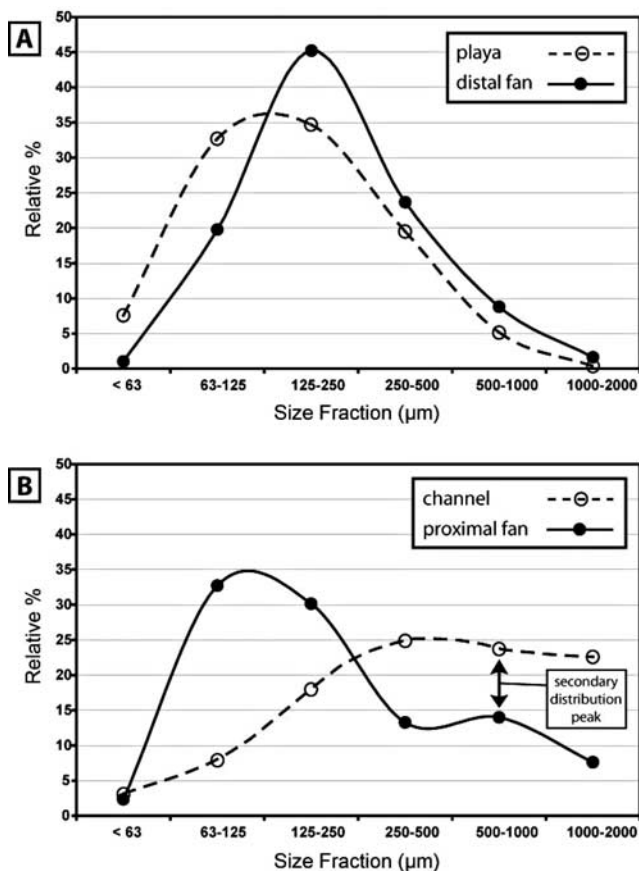


Figure 6. Grain size distributions for sediment samples collected along field transects. (a) Particle size distributions for distal Lucy Grey Fan deposits and Ivanpah Playa. The unimodal grain size distribution is very similar in both samples, particularly for grains larger than 125 μm . This similarity indicates the playa is the dominant source of windblown sediment in the distal fan. (b) Particle size distributions for proximal Lucy Grey Fan deposits and channel sediments. Proximal deposits exhibited a bimodal distribution with a secondary peak in the coarse sand fraction. This particle size is abundant in nearby channel sediments indicating that proximal deposits are partially sourced from coarser channel sediments.

in proximal piedmont eolian epipedons indicates medium sand (250–500 μm) is the critical grain size for which relief is a factor for eolian transportability in our field areas. Grain size analysis for distal fan transects and Ivanpah Playa is strikingly similar (Figure 6a), indicating that the playa is the dominant source of eolian material for the lower fan and that all available sediment is readily transported across the surface due to low relief. The presence of coarse sediment in eolian epipedons of proximal fan terraces indicates some transport of channel material must occur even though many sediment traps exist in this portion of the fan. It is possible that this transport occurs under extreme wind conditions capable of mobilizing larger sand grains from zones of high relief. In this sense, the upper fan “sees” the channels as a source of sediment under extreme wind conditions while the lower fan “sees” both channel and playa sediments as sources, although the playa is clearly the dominant source.

It is also possible that the larger grains observed in proximal piedmont surfaces were deposited by sheetwash or other fan-building processes before relief between terrace and channel was significant. Very fine-grained sediment in suspension sourced from local playas as well as other regional sources is likely deposited over the entire fan as its transport mechanism is not hindered by fan relief.

4. Discussion

[22] Model output is based on u_* and D values chosen from a range of possible field-calibrated values. While our best estimate of these parameters results in model output which closely matches the observed location of the onset of eolian transport across the fan, it is also possible that other combinations of these parameters will result in reasonable model output as well. For example, choosing a lower u_{*c} value would result in modeled eolian transport initiating in higher relief portions of the fan. This effect could be counterbalanced by using a lower estimation of u_* , resulting in model output similar to our initial results.

[23] The precise location of the observed eolian threshold cannot be definitively predicted by MSFD modeling. This is due primarily to uncertainty in the unperturbed shear velocity representing “extreme” wind conditions. In this paper we chose a value of 0.40 m/s, corresponding closely to the 90% percentile wind speed. There will, of course, be larger shear velocities exerted on the substrate (representing 99 and 99.9% percentiles, for example), but their relative rarity of these extreme wind speeds may prevent them from developing an eolian corridor. Despite this uncertainty, the model does show that a threshold condition exists for eolian transport, how the threshold condition is controlled by relief, grain size, and surface roughness, and that the threshold position is approximately where we observe it in the field using reasonable input parameter variables. Better constraint of threshold shear velocities and establishment of geomorphically most effective wind speeds are both candidates for future work pertaining to MSFD modeling of boundary layer flow and the influence of topography on eolian transport.

[24] Although model output was shown to be relatively insensitive to z_0 , the value for z_0 has significant influence on calculated u_* values which, in turn, have influence on model output. Unfortunately, the characterization of z_0 with respect to vegetation is a difficult task. The roughness density approach used here quantifies the mean frontal area of vegetation elements which absorb a portion of the shear stress otherwise available to act on the surface and transport sediment [Raupach *et al.*, 1993]. Possible modifications to the roughness density approach include consideration of vegetation flexibility and patterns in unvegetated areas, or “plant-interspacing” [Okin *et al.*, 2006]. In wind tunnel studies under ideal conditions z_0 is equal to 1/30 the grain size diameter. In our natural study areas, z_0 is a combination of roughness elements on various scales. Small-scale roughness elements such as pavement clasts, microtopography, and vegetation are superimposed on fan topography. The need for better approximation of z_0 values in the field has been previously expressed by Blumberg and Greeley [1993] and Lancaster *et al.* [1991].

[25] The location and extent of eolian corridors is important for hydrologic and pedologic studies. Windblown dust and sand compose a large percentage of pedologic material in late Pleistocene and Holocene soils in arid environments [Reheis *et al.*, 1995]. The amount of sand present in soil epipedons influences rates of infiltration and leaching which, in turn, affect depth to carbonate and other illuvial subsurface horizons. Pulses of eolian sediment can affect rates of soil genesis so significantly that steady state, linear models for soil horizonation and genesis have been shown to be inapplicable for soils forming downwind of significant sources of windblown sediment (i.e., playas or eolian corridors) [Chadwick and Davis, 1990].

5. Conclusions

[26] The existence of a relief threshold for sand transport by saltation is evident based on field and aerial photo observations as well as modeling. Zones of low relief permit transport of all available grain sizes while zones of higher relief provide more sediment traps and offer more resistance to sediment transport, particularly medium to coarse sand. Better constraint of model parameters combined with a more sophisticated approach for simulating complex roughness elements such as vegetation is important for future studies. Combining MSFD modeling of eolian transport by saltation with existing advection diffusion models of dust plume deposition [Pelletier and Cook, 2005] can provide a comprehensive view of eolian activity at subbasin to basin scales.

[27] **Acknowledgments.** Kyle House for helpful conversations regarding eolian corridors and the surficial geology of Ivanpah Valley. We gratefully acknowledge the support by the Army Research Office Terrestrial Sciences Program, grant W911NF-04-1-0266.

References

- Bagnold, R. A. (1941), *The physics of blown sand and desert dunes*, CRC Press, Boca Raton, Fla.
- Beljaars, A. C. M., J. L. Walmsley, and P. A. Taylor (1987), A mixed spectral finite difference model for neutrally stratified boundary layer flow over roughness changes and topography, *Boundary Layer Meteorol.*, **38**, 273–303.
- Blair, T. C., and J. G. McPherson (1994), Alluvial fans and their natural distinction from rivers based on morphology, hydraulic processes, sedimentary processes, and facies assemblages, *J. Sediment. Res. Sect. A*, **64**, 450–489.
- Blumberg, D. G., and R. Greeley (1993), Field studies of aerodynamic roughness length, *J. Arid Environ.*, **25**, 39–48.
- Bull, W. B. (1991), *Geomorphic responses to climatic change*, Oxford Univ. Press, New York.
- Chadwick, O. A., and J. O. Davis (1990), Soil-forming intervals caused by eolian sediment pulses in the Lahontan Basin, northwestern Nevada, *Geology (Boulder)*, **18**, 243–246.
- Dong, Z. B., X. P. Liu, and X. M. Wang (2002), Aerodynamic roughness of gravel surfaces, *Geomorphology*, **43**, 17–31.
- Dyer, K. R. (1986), *Coastal and estuarine sediment dynamics*, John Wiley, Hoboken, N. J.
- Greeley, R., and J. D. Iversen (1985), *Wind as a geological process on Earth, Mars, Venus, and Titan*, Cambridge Univ. Press, New York.
- Hagen, L. J. (1999), Assessment of wind erosion parameters using wind tunnels, paper presented at Sustaining the Global Farm, International Soil Conservation Organization, Purdue University, West Lafayette, Ind., 24–29 May.
- Hardisty, J., and R. J. S. Whitehouse (1988), Evidence for a new sand transport process from experiments on Saharan dunes, *Science*, **332**, 532–535.
- Howard, A. D. (1978), Sand transport model of barchan dune equilibrium, *Sedimentology*, **25**, 307–338.
- Karpik, S. R., J. L. Walmsley, and W. Weng (1995), The mixed spectral finite difference (MSFD) model: Improved upper boundary conditions, *Boundary Layer Meteorol.*, **75**, 353–380.
- Lancaster, N., and A. Baas (1998), Influence of vegetation cover on sand transport by wind: Field studies at Owens Lake, California, *Earth Surf. Process. Landf.*, **23**, 69–82.
- Lancaster, N., R. Greeley, and K. R. Rasmussen (1991), Interaction between unvegetated desert surfaces and the atmospheric boundary layer: A preliminary assessment, *Acta Mech. Suppl.*, **2**, 89–102.
- Marticorena, B., and G. Bergametti (1995), Modeling the atmospheric dust cycle: 1. Design of a soil-derived dust emission scheme, *J. Geophys. Res. Atmos.*, **100**, 16,415–16,430.
- Marticorena, B., G. Bergametti, B. Aumont, Y. Callot, C. Ndoume, and M. Legrand (1997a), Modeling the atmospheric dust cycle: 2. Simulation of Saharan dust sources, *J. Geophys. Res. Atmos.*, **102**, 4387–4404.
- Marticorena, B., G. Bergametti, D. Gillette, and J. Belnap (1997b), Factors controlling threshold friction velocity in semiarid and arid areas of the United States, *J. Geophys. Res. Atmos.*, **102**, 23,277–23,287.
- Nishimura, K., and J. C. R. Hunt (2000), Saltation and incipient suspension above a flat particle bed below a turbulent boundary layer, *J. Fluid Mech.*, **417**, 77–102.
- Okin, G. S., D. A. Gillette, and J. E. Herrick (2006), Multi-scale controls on and consequences of aeolian processes in landscape change in arid and semi-arid environments, *J. Arid Environ.*, **65**, 253–275.
- Pelletier, J. D. (2006), Sensitivity of playa windblown-dust emissions to climatic and anthropogenic change, *J. Arid Environ.*, **66**, 62–75.
- Pelletier, J. D., and J. P. Cook (2005), Deposition of playa windblown dust over geologic time scales, *Geology*, **33**, 909–912.
- Press, W. H., S. A. Teukolsky, W. T. Vetterling, and B. P. Flannery (1992), *Numerical Recipes in C: The Art of Scientific Computing Second Edition*, Cambridge Univ. Press, New York.
- Raupach, M. R. (1992), Drag and drag partition on rough surfaces, *Boundary Layer Meteorol.*, **60**, 375–395.
- Raupach, M. R., D. A. Gillette, and J. F. Leys (1993), The effect of roughness elements on wind erosion threshold, *J. Geophys. Res. Atmos.*, **98**, 3023–3029.
- Reheis, M. C. (1999), Dust deposition and its effect on soils: A progress report, in *Desert winds: Monitoring wind-related surface processes in Arizona, New Mexico, and California*, edited by S. Breed Carol and C. Reheis Marith, pp. 121–131, U. S. Geological Survey, Reston, VA, United States.
- Reheis, M. C., J. C. Goodmacher, J. W. Harden, and L. McFadden (1995), Quaternary soils and dust deposition in southern Nevada and California, *Geol. Soc. Am. Bull.*, **107**, 1003–1022.
- Taylor, P. A. (1998), Turbulent boundary layer flow over low and moderate slope hills, *J. Wind Eng. Ind. Aerodyn.*, **74**, 25–47.
- Walmsley, J. L., J. R. Salmon, and P. A. Taylor (1982), On the application of a model boundary layer flow over low hills to real terrain, *Boundary Layer Meteorol.*, **23**, 17–46.
- Wolman, M. G., and J. P. Miller (1960), Magnitude and frequency of forces in geomorphic processes, *J. Geol.*, **68**, 54–74.
- Xu, D., and P. A. Taylor (1995), Boundary layer parameterization of drag over small-scale topography, *Q. J. R. Meteorol. Soc.*, **121**, 433–443.

J. P. Cook and J. D. Pelletier, Department of Geosciences, University of Arizona, Gould-Simpson Building, 1040 East Fourth Street, Tucson, AZ 85721-0077, USA. (joe.cook@azgs.arizona.gov)

Cantor set model of eolian dust deposits on desert alluvial fan terraces

Jon D. Pelletier*

Department of Geosciences, University of Arizona, Gould-Simpson Building, 1040 East Fourth Street, Tucson, Arizona 85721-0077, USA

ABSTRACT

Available data show that eolian dust accumulation rates on desert alluvial fan terraces are often inversely proportional to the square root of the terrace age for a given area. This temporal scaling is similar to that observed in fluvial and marine stratigraphic sequences in which a fractal distribution of hiatuses occurs (i.e., a Cantor set). Eolian dust accumulation on alluvial fan terraces is controlled by regional climatic influences on dust deposition (e.g., dessication of pluvial lakes in the early Holocene) and local surface characteristics (e.g., vegetation and pavement coverage) that control dust preservation. In order to interpret the observed scaling in terms of these relative influences I consider two end-member models: (1) a deterministic model in which dust deposition is controlled by cyclical climatic changes (i.e., glacial-interglacial cycles) and in which no erosion occurs, and (2) a stochastic model in which erosion and deposition take place with equal probability and magnitude during each time step (i.e., a bounded random walk). The observed temporal scaling is most consistent with the bounded random walk model, suggesting that long-term eolian dust accumulation is predominantly controlled by episodic changes in vegetation and pavement coverage over time and that eolian dust deposits are strongly punctuated by episodes of erosional reworking at a wide range of temporal scales.

Keywords: eolian, dust, alluvial fan, soils, mathematical model.

INTRODUCTION

Eolian dust accumulation plays an important role in controlling the hydrology, pedology, and ecology of alluvial fan terraces (Yaalon and Ganor, 1973; McFadden et al., 1987; Chadwick and Davis, 1990). The input of fine silt and clay particles into gravelly parent material, for example, can reduce soil hydrologic conductivities by a factor of 100 over geologic time scales (Young et al., 2004). Dust accumulation also controls calcium carbonate development in many arid soils, which in turn can influence the types of vegetation that grow on them (McAuliffe, 1994). As such, eolian dust accumulation has been a central focus of surface-process studies in the arid and semiarid southwestern U.S. (e.g., McFadden et al., 1987; Reheis et al., 1995).

Dust accumulation on desert alluvial fan terraces can be affected by changes in either deposition or erosion. Previous studies have argued that climatically controlled dust deposition plays the predominant role in controlling dust accumulation on alluvial fan terraces, implicitly assuming that erosion was either negligible or constant on geologic time scales. Low rates of long-term (10^5 – 10^6 yr) dust accumulation in the southwestern U.S., for example, have been interpreted as a direct result of low dust deposition during the predominantly cool, wet Pleistocene, whereas high rates of shorter-term (10^3 – 10^4 yr) dust accumulation have been interpreted as an early Holocene pulse of dust deposition related to pluvial lake dessication

(Chadwick and Davis, 1990; Reheis et al., 1995; McFadden et al., 1986, 1998). In this paper I compare the observed eolian silt accumulation rates at six alluvial fan study sites with the predictions of quantitative models for eolian dust accumulation to test whether regional climatic controls on dust deposition or the effects of local surface coverage on dust preservation are most important for dust accumulation.

DATA ANALYSIS

Reheis et al. (1995) synthesized data on eolian dust accumulation from alluvial fan terrace study sites in the southwestern U.S. with optimal age control. These sites are located on gently sloping, planar alluvial fan terraces that have not been subject to flooding since abandonment by fan-head entrenchment. This time since fan-head entrenchment is the surface age, and it corresponds to the time interval of eolian dust accumulation. Figure 1 plots silt accumulation rates versus time interval on logarithmic scales for these locations. Error bars represent time interval (i.e., surface age) uncertainties. All of the locations studied by Reheis et al. (1995) that have at least four data points (i.e., distinct alluvial fan terraces) have been included. The plots in Figure 1 (A–D) exhibit a power-law trend (i.e., a straight line on log-log scales) given by

$$R \propto T^{-\alpha}, \quad (1)$$

where R is the accumulation rate, T is the time interval of accumulation, and α is an exponent close to 0.5. Values of α for each data

set were obtained by a linear fit of the logarithm of accumulation rate to the logarithm of time interval, weighted by the age uncertainty for each point. Accumulation rates plotted in Figures 1E and 1F (lower and upper fans near Silver Lake Playa) show only a weak dependence on time interval. Figure 1E, for example, has a nearly constant rate across time intervals, while Figure 1F shows a peak in accumulation rates at time intervals of 10^3 – 10^4 yr, consistent with an early Holocene dust pulse. Although only silt accumulations are plotted in Figure 1 (except for Fig. 1C, which gives results for clay accumulation on the Whipple Mountains fan because silt data were not available), results for clay and salt fractions at the same locations were broadly similar.

MODEL DESCRIPTION

In order to interpret the temporal scaling of dust accumulation rates with time interval I considered two end-member models. The first model assumes that the magnitude of dust deposition and erosion is constant through time (with a rate equal to $0.01 \text{ g/cm}^2/\text{yr}$ in this example) and that erosion or deposition takes place with equal probability during each time step (1 yr). Figure 2A illustrates two runs of this bounded random walk model. The walk is bounded because the net accumulation is always positive (in an unbounded random walk, negative values are also allowed). At the longest time interval ($\sim 10^4$ yr), both model runs have accumulated $\sim 1.5 \text{ g/cm}^2$ of dust (equal to a thickness of 1.5 cm if a density of 1 g/cm^3 is assumed).

*E-mail: jdpellet@email.arizona.edu.

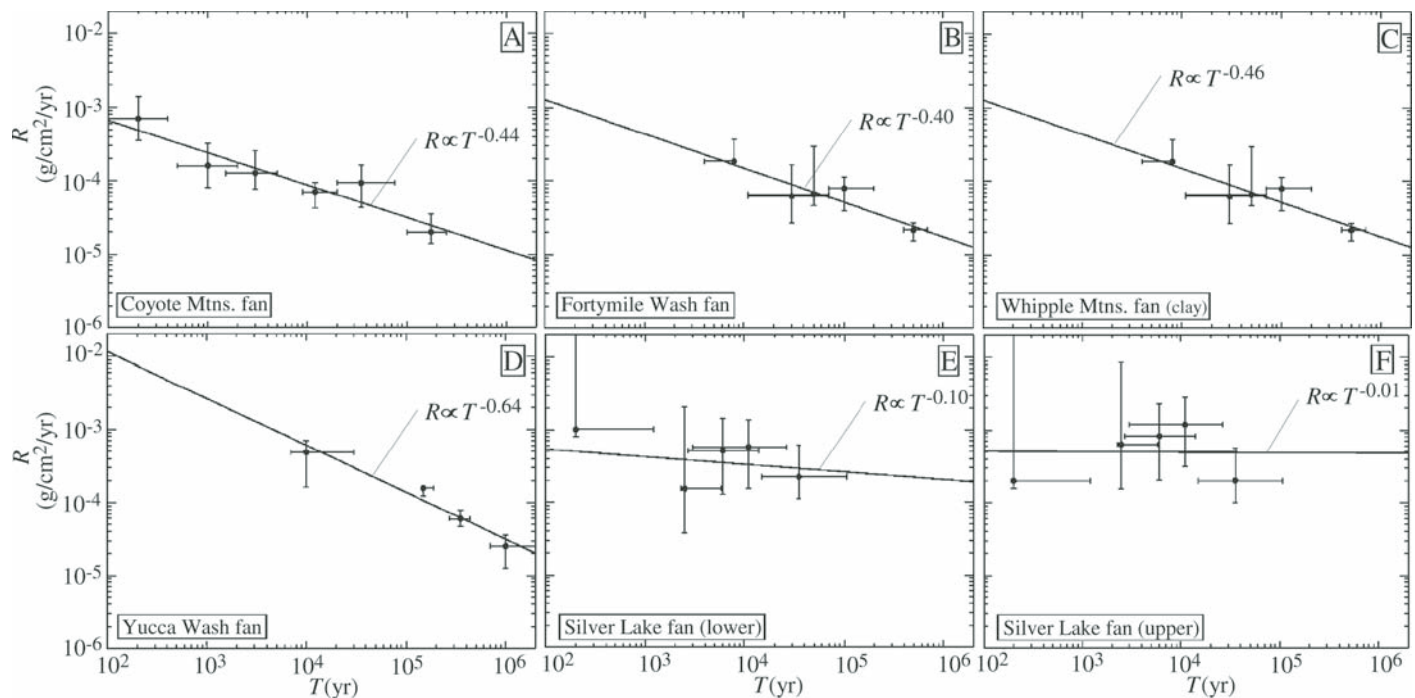


Figure 1. Plots of silt accumulation rates (R) vs. time interval (T) on alluvial fan terrace surfaces (from data in Reheis et al., 1995). A: Coyote Mountains fan. B: Fortymile Wash fan. C: Whipple Mountains fan (clay fraction shown). D: Yucca Wash fan. E: Lower fan near Silver Lake Playa. F: Upper fan near Silver Lake Playa. Best-fit lines indicate power-law scaling with exponents close to -0.5 for A–D. Trends in E and F are more consistent with linear accumulation or cyclical climate models.

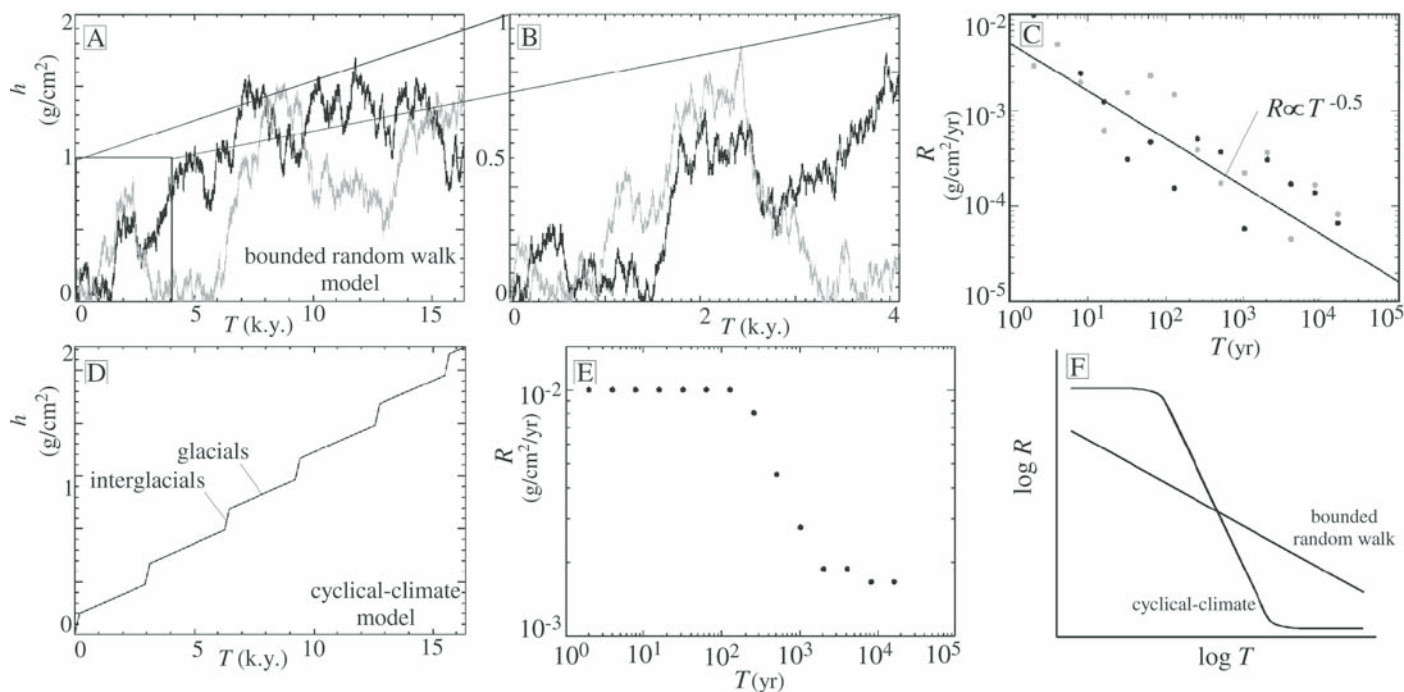


Figure 2. A: Plot of dust accumulation vs. time for two runs of bounded random walk model. B: Inset of A illustrating scale-invariance of bounded random walk model by rescaling time by factor of 4 and accumulation by factor of 2. C: Plot of accumulation rate vs. time interval illustrating power-law scaling behavior. D: Plot of dust accumulation vs. time in cyclical climate model. E: Plot of accumulation rate vs. time interval in cyclical-climate model, illustrating inverted S-shaped curve. F: Schematic diagram summarizing results of two models for accumulation rate vs. time interval.

On shorter time intervals (10^3 and 10^2 yr), net accumulations are smaller than the 1.5 value, but they are not linearly proportional to the time interval. For example, net accumulation is 0.3–0.5 g/cm² over 10^3 yr for the two model runs shown, a much larger change per unit time than the 1.5 g/cm² observed over 10^4 yr. Figure 2B illustrates the temporal scaling of accumulation rates versus time interval in this model. The results in Figure 2B illustrate that accumulation rates decrease, on average, at a rate proportional to one over the square root of the time interval, similar to that in Figures 1A–1D.

This power-law scaling behavior can also be derived theoretically. The average distance from zero in a bounded random walk, $\langle h \rangle$, increases with the square root of the time interval, T (van Kampen, 2001):

$$\langle h \rangle = aT^{1/2}, \quad (2)$$

where the brackets denote the value that would be obtained by averaging the result of many different model runs and a is the magnitude of erosion or deposition during each time step. As applied to eolian dust accumulation, the average distance $\langle h \rangle$ represents the total accumulation of eolian dust (in g/cm² or cm) on the surface, including the effects of episodic erosion. The average accumulation rate is obtained by dividing equation 2 by T to give

$$\langle R \rangle = aT^{-1/2}. \quad (3)$$

While the average rate scales according to equation 3, individual runs of the bounded random walk model do not follow equation 3 exactly due to fluctuations inherent in the model.

In the second end-member model, dust deposition is assumed to have a high value during interglacial periods (0.01 g/cm²/yr), a low value during glacial periods (0.002 g/cm²/yr), and no erosion. Figure 2E illustrates the accumulation rate versus time interval for this model. The plot follows an inversed S-shaped curve (Fig. 2E). This relationship is characteristic of accumulation rate curves for all periodic functions (Sadler and Strauss, 1990), and it is markedly different from the observed scaling in Figures 1A–1D.

The scaling behavior of accumulation rates shown in Figures 1A–1D is broadly similar to that observed in fluvial and marine deposits, and has a close association with the problem of stratigraphic completeness. Fluvial and marine stratigraphic sections are often incomplete because unconformities or hiatuses with a broad distribution of time intervals are present in these sections (Sadler, 1981). The accumulation rate curve can be used to quantify the completeness of a given section using the ratio of the overall accumulation rate to the average rate at a particular time interval T (Sadler and

Strauss, 1990). In the bounded random walk model, for example, a complete stratigraphic section (i.e., one with no hiatuses) of 10 k.y. duration would have a total accumulation of 100 g/cm² based on an annual accumulation rate of 0.01 g/cm². The bounded random walk model, in contrast, has an average accumulation of 1 g/cm² over 10 k.y. based on equation 2. Therefore, a 10 k.y. sequence is only 1% complete (i.e., 99% of the mass that was once deposited has been eroded). Plotnick (1986) showed that a power-law accumulation-rate curve (i.e., equation 1) specifically implied a power-law or fractal distribution of hiatuses, with few hiatuses of very long duration and many of short duration, analogous to the Gutenberg-Richter power-law distribution of earthquake magnitudes (Turcotte, 1997).

To see how temporal scaling of accumulation rates relates to the completeness of the stratigraphic record and to a fractal distribution of hiatuses, consider the accumulation model illustrated in Figures 3A–3C (after Plotnick, 1986). Depositional units (beds) in this model are of equal thickness. The depth of each bed is given as a function of age in Figure 3A. The time intervals of preserved deposits are characterized by a second-order Cantor set. A Cantor set is a classic fractal pattern created by repeatedly deleting the middle thirds from a set of line segments, starting by deleting the middle third of the line segment [0,1] to leave [0,1/3] and [2/3,1] (i.e., a first-order

Cantor set). Next the middle thirds of these two remaining line segments are removed to create a second-order Cantor set. Mathematically, a true Cantor set is created when this process of removing middle thirds is continued ad infinitum, but in nature there is always a finite bed thickness that limits the fractal scaling. Figure 3A shows that at the largest time interval (9 yr), 8 mm of sediments have accumulated, so the mean rate of accumulation is $R(9 \text{ yr}) = 8 \text{ mm}/9 \text{ yr} = 0.89 \text{ mm/yr}$ over this period. Similarly, during the first three years of accumulation the mean rates of accumulation are $R(3 \text{ yr}) = 4 \text{ mm}/3 \text{ yr} = 1.33 \text{ mm/yr}$. Thus the rate of deposition increases as the period considered decreases. This is shown in Figure 3B, where the power-law temporal scaling is illustrated. The bounded random walk model leads to a stochastic rather than a deterministic Cantor set, and to an exponential distribution of bed thicknesses rather than a single uniform bed thickness (Pelletier and Turcotte, 1997). Figure 3D illustrates the chronostratigraphic plot corresponding to a single run of the bounded random walk model (with $a = 0.01 \text{ cm/yr}$) shown in Figure 3C. In this plot, sediments deposited that are later eroded are removed from the sequence and identified as horizontal lines (hiatuses). The bounded random walk model results in a fractal distribution of hiatus lengths, located randomly in the domain, and exhibits power-law scaling of accumulation rate versus time interval similar to the deterministic Cantor set of Figures 3A and 3B.

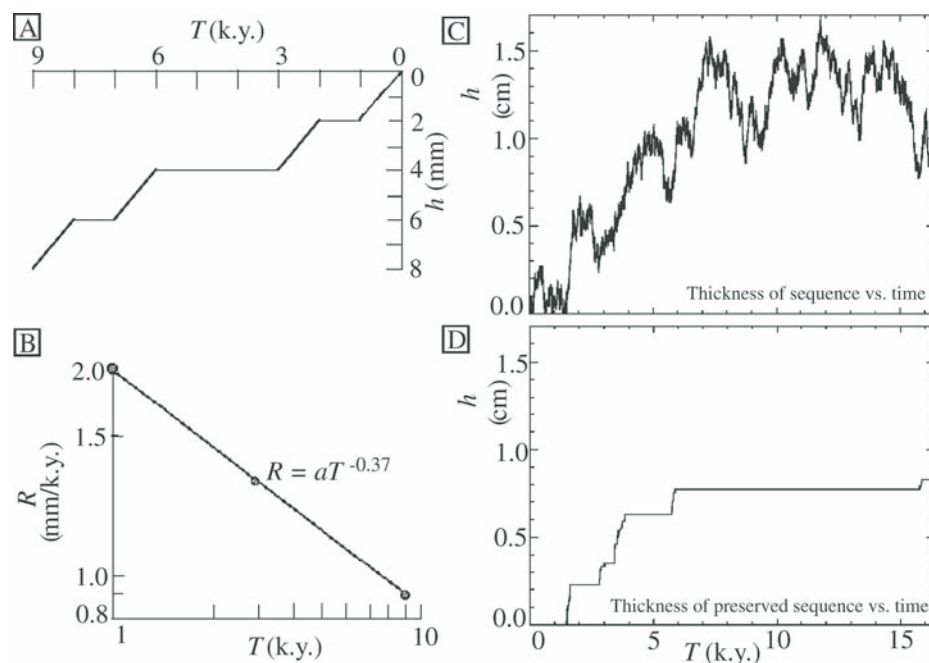


Figure 3. A, B: Illustration of synthetic stratigraphic section based on second order Cantor set. A: Depth of sediments h (mm) as function of sediment age (k.y.). B: Accumulation rate R as function of time interval T for model stratigraphic section in A. C: Plot of accumulation h (cm) in bounded random walk model as function of time assuming $a = 0.01 \text{ cm/yr}$ (a is magnitude of erosion or deposition during each time step). D: Chronostratigraphic plot of C, in which all sediment later eroded has been removed to indicate hiatuses (horizontal lines).

DISCUSSION AND CONCLUSIONS

Temporal scaling of accumulation rates in the bounded random walk model is observed down to time scales as low as the time step at which erosion and deposition alternate randomly. The success of this model in reproducing the observed temporal scaling of eolian accumulation rates suggests that erosion and deposition alternate over time scales $<10^2$ – 10^3 yr based on the lower limit of observed scaling in Figures 1A–1D. What process or processes could result in erosional and depositional alternation at time scales of 10^2 – 10^3 yr or smaller? Vegetation growth and decay is a likely possibility, either at the plant scale during individual births and deaths or at the landscape scale during interannual climatic changes. The presence of shrubs, for example, generally protects the nearby ground from eolian erosion and promotes deposition (Wolfe and Nickling, 1993). When a plant dies and its cover is removed, however, the ground surface is often mounded and susceptible to local wind erosion (Whicker et al., 2002). In such cases the fundamental time scale for alternation could be either the mean shrub lifespan, which is typically $\sim 10^2$ yr (Cody, 2000), or at the interannual and interdecadal time scales of short-term climatic changes that modulate landscape-scale vegetation cover.

The results of Figure 1 suggest that eolian dust accumulation on alluvial fans located close to playa sources (Figs. 1E, 1F) is fundamentally different from that on fans located far from playa sources (Fig. 1A–1D). The fan study sites close to Silver Lake Playa exhibit a linear accumulation trend on the lower fan site and a cyclical climate trend on the upper fan site while the remaining fan sites exhibit accumulation trends consistent with the bounded random walk model. This distinction between fans proximal and distal to playa sources is consistent with the results of Pelletier and Cook (2005), who showed that dust accumulation is strongly localized downwind from playa sources and decreases to regional background values within a few kilometers from a playa source. The results of Figure 1 and those of Pelletier and Cook (2005) suggest that the bounded random walk model may be representative of the majority of fans located far (i.e., greater than a few kilometers) from playas, and that the classic linear-accumulation or cyclical-climate models are representative of accumulation on fans proximal to playa sources where dust deposition is rapid enough to overwhelm the effects of episodic disturbances.

Climate cannot be dismissed as a factor in dust accumulation, and it cannot be argued that dust accumulation on desert surfaces is purely random. It is clear from ice core records that global dust deposition varies strongly with glacial-interglacial cycles (Petit et al., 1990), and such variations must have an influence on dust accumulation. It is also clear that dust accumulation is not purely a random process. Dust accumulation and desert pavements, for example, clearly coevolve by a positive feedback in which dust accumulation promotes clast migration and suturing through wetting-drying cycles, thereby increasing dust preservation in a positive feedback (McFadden et al., 1987). Nevertheless, the results shown in this paper suggest that eolian deposits preserve only a tiny fraction of the total dust deposited on the surface over time. Care should be taken, therefore, in interpreting eolian dust deposits in terms of purely deterministic factors.

ACKNOWLEDGMENTS

I thank Peter Sadler and Marith Reheis for helpful reviews, and the U.S. Army Research Office Terrestrial Sciences Program (grant W911NF-04-1-0266) for financial support. This work would not have been possible without the painstaking effort of many U.S. Geological Survey geologists, especially Reheis, over the course of many years.

REFERENCES CITED

- Chadwick, O.A., and Davis, J.O., 1990, Soil-forming intervals caused by eolian sediment pulses in the Lahontan basin, northwestern Nevada: *Geology*, v. 18, p. 243–246, doi: 10.1130/0091-7613(1990)018<0243:SFICBE>2.3.CO;2.
- Cody, M.L., 2000, Slow-motion population dynamics in Mojave Desert perennial plants: *Journal of Vegetation Science*, v. 11, p. 351–358.
- McAuliffe, J.R., 1994, Landscape evolution, soil formation, and ecological patterns and processes in Sonoran Desert bajadas: *Ecological Monographs*, v. 64, p. 111–148, doi: 10.2307/2937038.
- McFadden, L.D., Wells, S.G., and Dohrenwend, J.C., 1986, Influences of Quaternary climatic changes on processes of soil development on desert loess deposits of the Cima volcanic field, California: *Catena*, v. 13, p. 361–389, doi: 10.1016/0341-8162(86)90010-X.
- McFadden, L.D., Wells, S.G., and Jercinovich, M.J., 1987, Influences of eolian and pedogenic processes on the origin and evolution of desert pavements: *Geology*, v. 15, p. 504–508, doi: 10.1130/0091-7613(1987)15<504:IOEAPP>2.0.CO;2.
- McFadden, L.D., McDonald, E.V., Wells, S.G., Anderson, K., Quade, J., and Forman, S.L., 1998, The vesicular layer and carbonate collars of desert soils and pavements: Formation, age, and relation to climate change: *Geomorphology*, v. 24, p. 101–145, doi: 10.1016/S0169-555X(97)00095-0.
- Pelletier, J.D., and Cook, J.P., 2005, Deposition of playa windblown dust over geologic time scales: *Geology*, v. 33, p. 909–912, doi: 10.1130/G22013.1.
- Pelletier, J.D., and Turcotte, D.L., 1997, Synthetic stratigraphy with a stochastic diffusion model of sedimentation: *Journal of Sedimentary Research*, v. 67, p. 1060–1067.
- Petit, J.R., Mounier, M., Jouzel, J., Korotkevitch, Y., Kotlyakov, V., and Lorius, C., 1990, Paleoclimatological implications of the Vostok core dust record: *Nature*, v. 343, p. 56–58, doi: 10.1038/343056a0.
- Plotnick, R.E., 1986, A fractal model for the distribution of stratigraphic hiatuses: *Journal of Geology*, v. 94, p. 885–890.
- Reheis, M.C., Goodmacher, J.C., Harden, J.W., McFadden, L.D., Rockwell, T.K., Shroba, R.R., Sowers, J.M., and Taylor, E.M., 1995, Quaternary soils and dust deposition in southern Nevada and California: *Geological Society of America Bulletin*, v. 107, p. 1003–1022, doi: 10.1130/0016-7606(1995)107<1003:QSADDI>2.3.CO;2.
- Sadler, P.M., 1981, Sediment accumulation rates and the completeness of stratigraphic sections: *Journal of Geology*, v. 89, p. 569–584.
- Sadler, P.M., and Strauss, D.J., 1990, Estimation of completeness of stratigraphic sections using empirical data and theoretical models: *Geological Society [London] Journal*, v. 147, p. 471–485.
- Turcotte, D.L., 1997, *Fractals and chaos in geology and geophysics*: New York, Cambridge University Press 398 p.
- van Kampen, N.G., 2001, *Stochastic processes in physics and chemistry*: Amsterdam, Elsevier, 419 p.
- Whicker, J.J., Breshears, D.D., Wasiolek, P.T., Kirchner, T.B., Tavani, R.A., Schoep, D.A., and Rodgers, J.C., 2002, Temporal and spatial variation of episodic wind erosion in unburned and burned semiarid shrubland: *Journal of Environmental Quality*, v. 31, p. 599–612.
- Wolfe, S.A., and Nickling, W.G., 1993, The protective role of sparse vegetation in wind erosion: *Progress in Physical Geography*, v. 17, p. 50–68.
- Yaalon, D.H., and Ganor, E., 1973, The influence of dust on soils in the Quaternary: *Soil Science*, v. 116, p. 146–155, doi: 10.1097/00010694-197309000-00003.
- Young, M.H., McDonald, E.V., Caldwell, T.C., Benner, S.G., and Meadows, D.G., 2004, Hydraulic properties of a desert soil chronosequence, Mojave Desert: CA: *Vadose Zone Journal*, v. 3, p. 956–963.

Manuscript received 15 September 2006

Revised manuscript received 21 December 2006

Manuscript accepted 28 December 2006

Printed in USA

Desert pavement dynamics: numerical modeling and field-based calibration

Jon D. Pelletier,^{1*} Michael Cline^{2,3} and Stephen B. DeLong^{1,3}

¹ Department of Geosciences, The University of Arizona, Tucson, AZ, USA

² Department of Geography and Regional Development, The University of Arizona, Tucson, AZ, USA

³ Los Alamos National Laboratories, Los Alamos, NM, USA

*Correspondence to: Jon D. Pelletier, Department of Geosciences, University of Arizona, 1040 East Fourth Street, Tucson, AZ 85721, USA. E-mail: jdpellet@email.arizona.edu

Abstract

Desert pavements are widely used as a relative surface-dating tool because they are progressively better developed on surfaces ranging from thousands to hundreds of thousands of years in age. Recent work, however, has highlighted the dynamic nature of pavements and undermined their use as surface-age indicators. Quade (2001) proposed that latest Pleistocene vegetation advances destroyed all Mojave Desert pavements above 400 m elevation, making all such pavements Holocene in age. In an effort to reconcile young-pavement evidence with their widespread use as Pleistocene surface-age indicators, we developed a numerical model based on the classic conceptual model in which pavements co-evolve with their underlying eolian epipedons over millennial timescales. In this co-evolutionary process, fine-grained eolian deposition and A_v-horizon development within the eolian epipedon promotes surface clast motion and pavement development, enhancing the eolian-sediment-trapping ability of the pavement in a positive feedback. Model results illustrate the multi-scale nature of pavement dynamics: pavements may require tens of thousands of years to fully develop from a newly abandoned alluvial surface, but may heal over timescales of decades to centuries if a mature eolian epipedon is present. As such, there is no inconsistency between rapid pavement healing and a Pleistocene age for the underlying alluvial surface.

To calibrate the model, we conducted surficial geologic mapping and pavement-sedimentological analysis on two desert piedmonts. Our study areas include both proximal and distal fan environments, illustrating the role of parent-material texture in controlling the mode of pavement formation. Using available geochronology, our work provides a rigorous calibration of pavement formation rates in our study areas and provides evidence supporting the use of pavements as local relative surface-age indicators over Holocene to late Pleistocene timescales. Copyright © 2007 John Wiley & Sons, Ltd.

Keywords: desert pavement; numerical modeling; alluvial fan; Amargosa Valley

Received 7 July 2006;
Revised 18 December 2006;
Accepted 9 January 2007

Introduction

Desert pavements have long been used as relative-age indicators on arid-region alluvial surfaces (Wells *et al.*, 1985; McFadden *et al.*, 1987; Bull, 1991; Wells *et al.*, 1995; Anderson *et al.*, 2002; Valentine and Harrington, 2006). Pavements form as eolian sediments are progressively accumulated on desert surfaces. On these surfaces, a stony monolayer rises and organizes atop a thickening cumulic eolian epipedon (Wells *et al.*, 1985, 1987; McFadden *et al.*, 1987). While pavements are often used as surface-age indicators from Holocene to late Pleistocene timescales, other evidence suggests that desert pavements may form and heal over much shorter timescales (Haff and Werner, 1996; Quade, 2001). Quade (2001), for example, argued that all Mojave Desert pavements above 400 m elevation must be early Holocene in age or younger due to the existence of pavement-disrupting plants at those elevations during the last glacial maximum. This argument undermines the widely assumed long-term stability of pavements and the relationship between the age of a desert pavement and the underlying alluvial deposit. Marchetti and Cerling (2005) provided further evidence that pavement ages might differ from surface ages by demonstrating that pavement clasts have

systematically younger cosmogenic exposure ages than boulders on the same abandoned depositional surface. Their results imply that pavements formed significantly later than the age of abandonment of the underlying alluvial deposit and/or that pavement clasts were subject to episodic burial and excavation. Experiments conducted by Haff and Werner (1996) and observations by Haff (2005) provide evidence for the dynamic nature of pavements over annual to decadal timescales. Extrapolating their measured rates of pavement healing, Haff and Werner (1996) concluded that a decimeter-scale clearing on a pavement surface could completely 'heal' in approximately 80 yr. Similarly, Prose and Wilshire (2000) observed that pavement disturbance by Patton's tank tracks during the 1942–1944 Mojave Desert exercises and 1964 Desert Strike tank exercises shows significant pavement healing. Both studies noted that pavements tend to heal with smaller clasts than the original pavement.

Recently, Valentine and Harrington (2006) noted that desert pavements on a 75–80 ka volcanic surface and a ca. 1 Ma surface differed in 'tightness, reddening of clast undersides and varnishing of clast tops'. They concluded that their findings contradicted Quade's (2001) conclusion that all pavements above 400 m are Holocene in age. Valentine and Harrington dismissed the idea that multiple cycles of pavement formation and healing could result in a more mature pavement, and suggested that a more favorable possibility was that the older pavement has been vegetation free since initial formation.

In light of these seemingly conflicting observations, we gathered new field data and developed a numerical model of desert pavement formation and healing that treats the stony monolayer and its underlying eolian epipedon as a coupled system. Our work was motivated by the evidence that vegetation and other periodic disturbances on old desert surfaces likely influence pavement dynamics, but that pavements are nonetheless relative age indicators on Pleistocene timescales. Our field results indicate that desert pavements are useful age indicators on Holocene and late Pleistocene-aged alluvial surfaces and our model demonstrates that there is no inconsistency between rapid pavement healing and much slower pavement formation on a newly abandoned alluvial surface.

Desert Pavement Formation

Most desert pavements are understood to form by an inflationary process in which eolian sediment is trapped beneath surface clasts. The presence of a subsurface eolian layer promotes the surface motion of clasts by a variety of processes, leading to the interlocking and suturing of clasts to form a pavement. These processes include wetting–drying cycles, freeze–thaw cycles and bioturbation (Springer, 1958; Corte, 1963; Inglis, 1965; Haff and Werner, 1996). Each of these processes is enhanced by the presence of the fine-grained epipedon itself. For example, wetting–drying and freeze–thaw cycles are intensified by the presence of fine-grained sediments with a high water-storage potential. Faunal bioturbation is enhanced when the epipedon is sufficiently thick to accommodate animal burrowing. Fracturing of the coarsest clasts to form smaller, more-angular clasts with greater coverage potential has also been suggested as an important pavement-forming process (McFadden *et al.*, 2005; Al-Farraj and Harvey, 2000; Amit *et al.*, 1993). Although this process is unrelated to eolian-layer thickness, because it is also time dependent it serves as an enhancement to other processes that accelerate as the eolian layer thickens.

Our fieldwork focused on three primary goals. First, by examining two piedmonts with contrasting textures, we aimed to identify the role of texture in the processes and timescales of pavement development. Second, we aimed to evaluate alternative quantitative measures of pavement formation (i.e. fraction clast cover, mean clast size and clast-size autocorrelation function) and identify which measures were most appropriate for each piedmont environment. Our third goal was to use geochronology and measures of pavement development on a range of surfaces with different ages to calibrate the timescale for pavement development in our study areas.

Study Areas

Our field work focused on two piedmonts in Amargosa Valley (Nevada and California) (location map in Figure 1). The Fortymile Wash alluvial fan is an alluvial-channel-fed, low-relief, distal alluvial fan, which transports and deposits moderately sorted sandy alluvium and is strongly influenced by sand-dominated eolian input. The Eagle Mountain piedmont, in contrast, is a small, proximal, steep, poorly sorted, gravel-to-cobble-dominated bajada with dominantly silty eolian input. Our study sites on each fan were chosen to be between 600 and 700 m above sea level. In this way, the effects of elevation (and hence vegetation) on pavement development were minimized.

We conducted detailed surficial geologic mapping in both study areas (Figure 2). The Fortymile Wash alluvial fan is located in northern Amargosa Valley, NV. Fortymile Wash drains a 970 km² drainage basin that includes the proposed Nuclear Waste Repository at Yucca Mountain. A portion of the fan was mapped at a 1:10 000 scale by the authors to

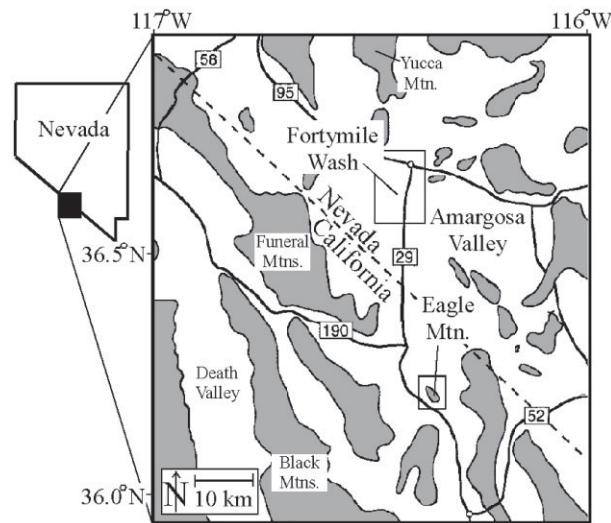


Figure 1. Location map of the study areas in Fortymile Wash alluvial fan and Eagle Mountain piedmont.

support volcanic-hazard assessment for the Yucca Mountain Project (i.e. modeling the fluvial and eolian redistribution of ash following a hypothetical eruption that intersects the repository). The gradient of the fan rarely exceeds 1%. The fan is dominated by sandy, gravelly and occasionally cobbly material, with rare boulders up to 1 m in diameter. The eolian-silt input is likely sourced by nearby playas, especially Franklin Lake Playa, but the dominant eolian input is fine to medium-grained sand derived from local active channels along Fortymile Wash and the Amargosa River. This sand locally forms coppice dunes and is visible as bright, NNW-directed streaks on aerial photographs. Silt-dominated vesicular A_v horizons on Fortymile Wash alluvial fan are fairly thin (<5 cm) and spatially discontinuous. The maximum relief from the oldest unit (Qa3) to the active channels (Qa7) is 1–2 m, decreasing down-fan. Relief between units of adjacent age is typically 0.5 m, and often the intra-surface bar-and-swale relief approaches the relief between surface units.

Eagle Mountain piedmont is located in southern Amargosa Valley, CA, where Franklin Lake Playa abuts the Eagle Mountain piedmont. This piedmont is fed by a series of small (<5 km²), high-relief drainage basins. The water table in Franklin Playa is less than 3 m below the surface (Czarnecki, 1997). Vapor discharge from this shallow aquifer creates a 'soft, puffy, porous' surface responsible for unusually high dust fluxes (Czarnecki, 1997). Eagle Mountain piedmont acts as the depositional substrate for dust emitted from Franklin Lake playa under northerly-wind conditions.

The surficial geology of Fortymile Wash fan and Eagle Mountain piedmont was mapped using the elevation above active channels, terrace dip, depth-of-dissection, degree of planarity, drainage pattern (tributary versus distributary) and development of pavement, varnish and calcic soils as relative-age indicators (McFadden *et al.*, 1989; Bull, 1991) (Table I). Holocene and Pleistocene units were readily distinguished using pavement and varnish development, as is the case elsewhere in Amargosa Valley (Whitney *et al.*, 2004). The degree of surface planarity was particularly useful for distinguishing between middle-to-late (Qa2) and late Pleistocene (Qa3) units on Eagle Mountain piedmont, both of which have moderate to strong pavement and varnish development. Middle-to-late Pleistocene terraces are 'crowned,' reflecting a longer interval of diffusive hillslope adjustment compared to late Pleistocene surfaces. Approximate ages have been assigned based on correlation with the regional chronology of Whitney *et al.* (2004), who established a uniquely detailed Quaternary alluvial chronology in northern Amargosa Valley and surrounding areas in support of the Yucca Mountain Project. Terraces on the Eagle Mountain piedmont range in age from middle Pleistocene (Qa2), middle to late Pleistocene (Qa3), late Pleistocene (Qa4), and latest Pleistocene to active (Qa5–Qa7) based on this correlation.

We utilized surface characteristics uncontrolled or only loosely controlled by eolian influx to the greatest extent possible in our mapping. In particular, we relied heavily on landscape position, drainage pattern development, degree of planarity and the degree of preserved bar-and-swale patterns in order to distinguish between surfaces and correlate with the Whitney *et al.* (2004) chronology. Progressively older surfaces are characterized by a systematic decrease in bar-and-swale micro-topography and texture, and a gradual rounding of gully and terrace edges by diffusive hillslope processes (Hsu and Pelletier, 2004). On both piedmonts, hillslope erosion has performed only minor rounding of Qa6 and Qa5 surfaces. Fluvial scarps bounding these map units rise abruptly to planar surfaces over a distance of less than

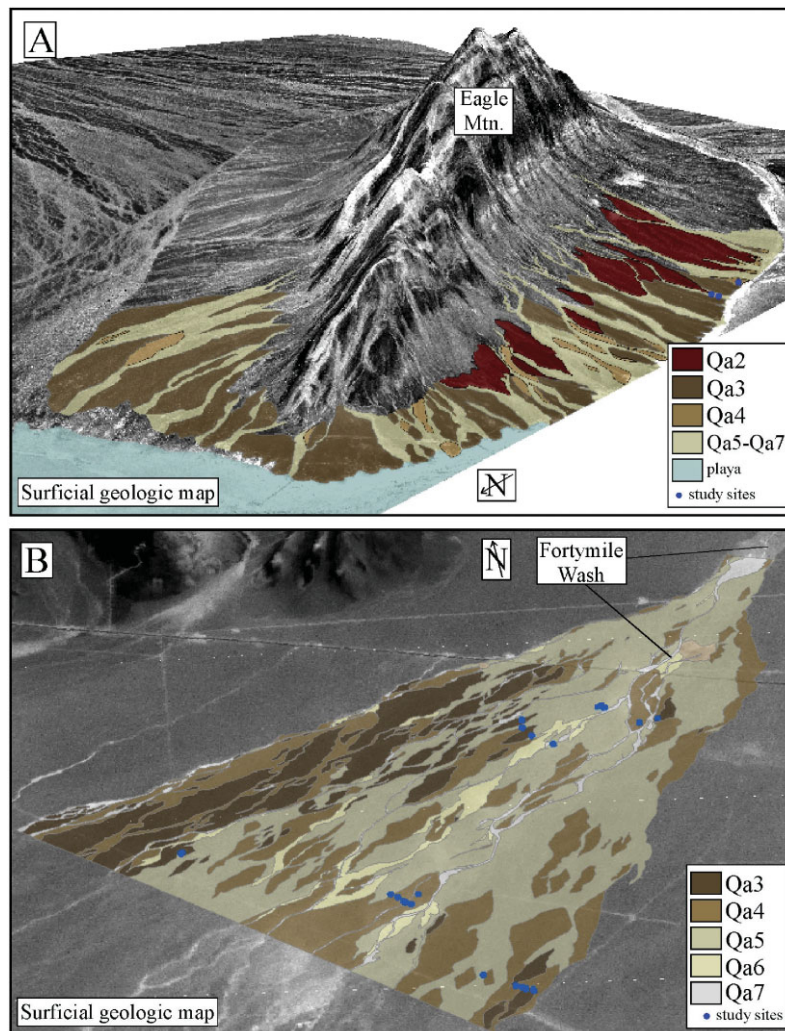


Figure 2. Surficial-geologic maps of the study areas on (A) Eagle Mountain piedmont and (B) Fortymile Wash alluvial fan. Approximate surface ages are Qa2 – middle Pleistocene, Qa3 – middle to late Pleistocene, Qa4 – late Pleistocene, Qa5–Qa7 – latest Pleistocene to active, based on correlation with the chronology of Whitney et al. (2004). This figure is available in colour online at www.interscience.wiley.com/journal/esp

1 m. On Qa4 surfaces, the terrace-bounding scarp is wider: backwearing and hillslope rounding has penetrated 2–4 m horizontally into the terrace tread. The extent of hillslope rounding increases greatly as one steps up onto the Qa3 and Qa2 deposits (to approximately 10 m and 20–40 m, respectively), reflecting the much longer duration of hillslope erosion experienced by these surfaces. Utilizing the extent of preserved bar-and-swale texture and micro-topography is potentially problematic as a method to correlate equal-age surfaces between distinct piedmonts, because this process is partly dependent on eolian influx. It does appear, however, to be a robust method for distinguishing differing-age surfaces within a single piedmont.

Role of Parent-Material Texture in Pavement Formation and Measurement

The texture of the alluvial-fan parent material plays an important role in determining the specific mode of pavement formation in each of the study areas. In a gravel-dominated parent-material environment such as a proximal fan, clast motion is unlikely to be significant until the eolian layer is sufficiently thick to cause expansion/contraction of

Table 1. Map unit descriptions on Fortymile Wash alluvial fan

	Qa7	Qa6	Qa5	Qa4	Qa3
Age range (ka) [†]	Historical	0–5?	7 + 10/–5	27 ± 10	86 + 40/–16
Pavement development	None	Extremely weak	Weak	Moderate	Strong
Bar/swale relief; drainage pattern	Variable	1 m relief; distributary	0.5–1 m relief; distributary	Subdued, sub-planar; <30 cm relief, tributary	Planar; indistinct drainage
Relief above active channel (m)	N/A	0.3–1	0.5–1	0.5–1	0.5–2.0
Rubification and varnish	None	None	None	Weak to moderate	Moderate to strong
Maximum soil development	None	Rare incipient petrocalcic development on sands and some gravels	Stage I+ petrocalcic development	Stage II+ petrocalcic development at 0.5 m; B _{cambic} horizon below 60 cm	Stage IV petrocalcic K horizon at 1.2 m; incipient B _t horizon at 0.8–1 m
Eolian epipedon thickness (cm)	None	10	20–35	30–60	60–80
Epipedon description	None	Rare, sandy	Loamy sand; floating clasts in lower epipedon	Loamy sand; floating clasts; discontinuous A _v with max. thickness 10 mm	Loamy sand; floating clasts; discontinuous A _v with max. thickness 50 mm
Areal %	12	3	42	26	16 (area only includes internal portions of fan)

Based on correlation with Whitney *et al.* 2004.

the surface through wet–dry and freeze–thaw cycles. In a sand-dominated parent-material environment such as a distal fan, the initial surface has relatively few clasts with which to form a pavement. In these cases, pavement clasts must first be pushed to the surface vertically and/or distributed horizontally by freeze–thaw, wetting–drying cycles and bioturbation (Springer, 1958; Corte, 1963; Inglis, 1965), or other size-segregative processes, or possibly made available through progressive fracturing of larger clasts (Al-Farraj and Harvey, 2000; McFadden *et al.*, 2005). As the surface gains clast-material coverage, lateral migration serves to interlock and suture the clasts as in the gravel-dominated case. These two distinct modes of pavement formation are found in the Fortymile Wash and Eagle Mountain study areas, and they are illustrated schematically in Figure 3.

Pavement Development Measurement

On the sand-dominated Fortymile Wash alluvial fan we used the fraction clast coverage to quantify pavement development. Fraction clast coverage was determined by point counting using wire-framed grids. We measured pavements at 29 sites, comprising two transects along the upper and lower parts of the fan (Figure 2(B)). We chose a 4 mm diameter cutoff to distinguish between clasts that are part of the pavement and sand and granules that are most likely either parent material or eolian material and not part of the pavement. Sampling sites were chosen on intershrub areas, where pavements were least disturbed by modern vegetation. We also measured the mean and standard deviation of clast diameter (on the intermediate axis) on each surface as an alternative measure of pavement development. The mean and standard deviation of clast size did not show systematic variations with surface age. Most likely, these measures are a complex combination of pavement development and parent-material differences (Mayer and Bull, 1981). We also described the underlying epipedon at each site.

In gravel-dominated parent materials, the modern channel is comprised almost entirely of gravel-sized clasts. In this case, fraction clast coverage is not a meaningful measure of pavement development, since it begins at or near unity and stays constant. We therefore designed a new method for pavement-development measurements on the Eagle Mountain piedmont. In gravel-dominated environments such as this, pavement development is best characterized by a gradual reduction in the bar-and-swale texture through time (Figure 3). The processes causing reduction in bar-and-swale texture include the aforementioned freeze–thaw, wetting–drying and bioturbation. Because of the relatively pronounced original topography on the gravel-dominated alluvial surfaces, sediment transfer related to gravity-driven processes such as overland flow, and locally increased water and dust flux in swale soils (Eppees and Harrison, 1999),

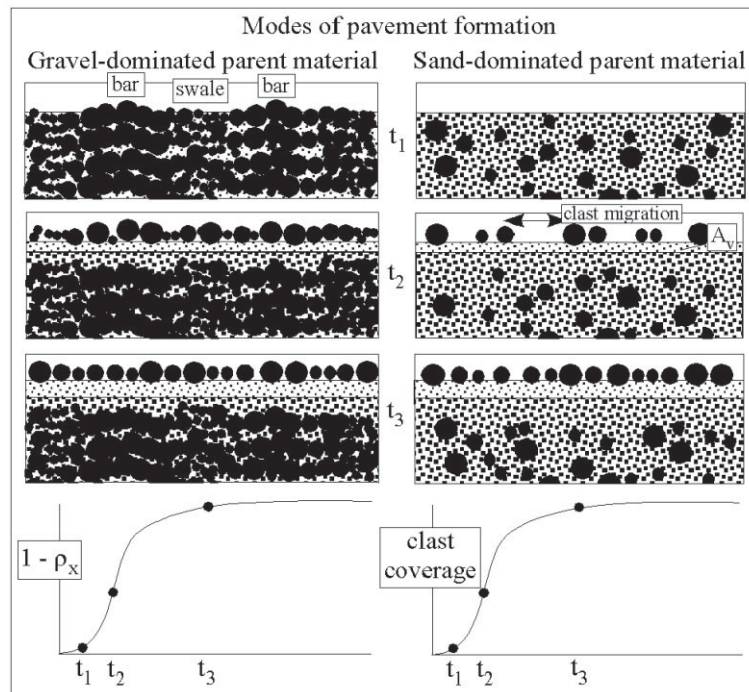


Figure 3. Modes of pavement formation in sand-dominated and gravel-dominated parent materials, exemplified by the Fortymile Wash and Eagle Mountain study areas. In a gravel-dominated environment, pavement development is characterized by a progressive loss of bar-and-swale texture through time. The eolian epipedon promotes expansion/contraction processes that move clasts laterally on the surface, gradually eliminating the bar-and-swale texture and microtopography inherited from alluvial-channel processes. This progressive loss of bar-and-swale pattern can be quantified as $1 - \rho_x$, where ρ_x is the correlation coefficient of clast diameters separated by a distance x . In sand-dominated parent material, pavement development involves the upward migration of large clasts by expansion/contraction processes in addition to lateral migration. Pavement development in these cases can be quantified using fraction clast coverage.

may play important roles in reducing bar-and-swale texture. Matmon *et al.* (2006) concluded that spatially variable bar to swale sediment transfer on abandoned alluvial fans decreases over geologic timescales as fan surfaces are smoothed. Matmon *et al.* (2006), however, also concluded that, based on cosmogenic data, abandoned fans in their study area were dominated by surface lowering and lack pavement formation during smoothing. This contrasts with the fans in our study areas that are dominated by surface inflation due to eolian input and pavement development over geologic timescales.

Young gravel-dominated alluvial surfaces have a relatively strong bar-and-swale texture (i.e. coarse clasts tend to be clustered on bars and fine clasts are clustered in swales), while older surfaces have progressively less clustering, gradually approaching a state in which each clast size is independent of adjacent clast sizes. This evolution can be characterized using the autocorrelation function of clast size along transects that run perpendicular to the surface dip and flow direction. The autocorrelation function is a measure of the average similarity between two values in a series separated by a distance x . Mathematically, the autocorrelation function is defined by (Box *et al.*, 1994)

$$\rho_x = \frac{\sum_i (d_i - \bar{d})(d_{x+i} - \bar{d})}{\sum_i (d_i - \bar{d})^2} \quad (1)$$

where d_i is the intermediate-axis clast diameter at a position i along the transect and \bar{d} is the mean intermediate clast diameter. For young surfaces, the value of ρ_x is significantly above zero (for spatial lags x less than the typical bar-and-swale width). Over time, ρ_x tends towards zero as the bar-and-swale texture is gradually eliminated by random clast motion along the surface. In order to use ρ as part of an index of pavement development that increases over time, $1 - \rho_x$ should be used. We call this function the 'textural randomness' because it increases in value as the surface

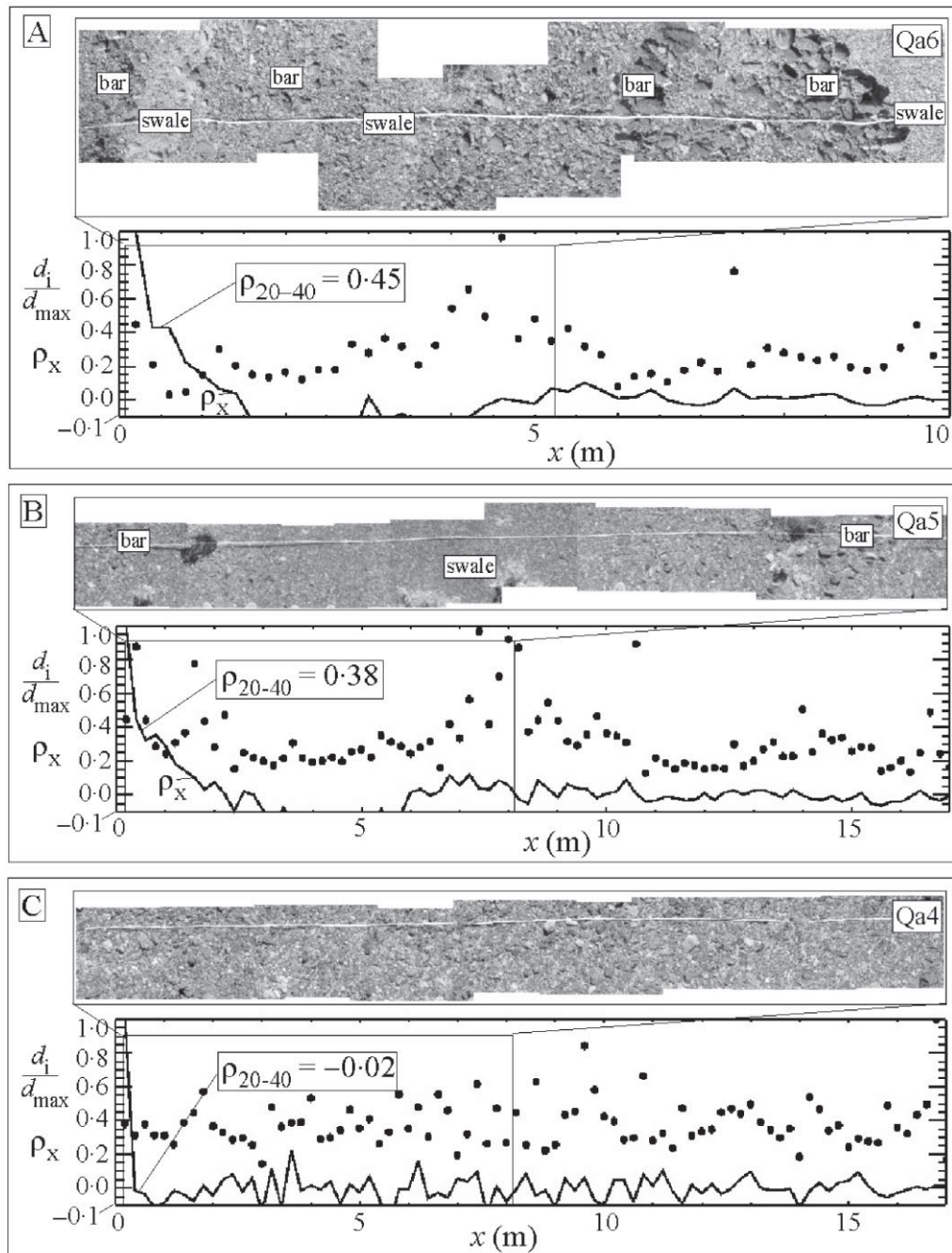


Figure 4. Clast-size autocorrelation-function analysis for Eagle Mountain piedmont, showing photo-mosaic, along-strike transects of clast diameter and autocorrelation function for (A) Qa6, (B) Qa5 and (C) Qa4. Photo-mosaics show a decrease in bar-and-swale texture with age. The autocorrelation function values for lags 20–40 cm capture effect quantitatively.

texture becomes more random over time. The value of the spatial lag x should be chosen to be larger than the coarsest clasts (to avoid double-counting) but smaller than the typical width of bars and swales.

Figure 4 illustrates examples of the textural randomness on Qa6, Qa5 and Qa4 surfaces of Eagle Mountain piedmont. Due to the large number of clast counts required for this analysis we used photo-mosaics rather than direct field measurements. In doing so, we assumed that each pavement clast is embedded in the pavement with its short

axis aligned vertically. With this assumption, the intermediate-axis diameter is measured along the short axis in the photographs. Photographs were acquired using a high-resolution digital camera located approximated 1.2 m from the surface and aimed straight down. Photographs were acquired along transects oriented along-strike (i.e. perpendicular to the surface dip and direction of flow). A tape measure was used for scale. The photographs were mosaicked and a grid was overlain to aid in clast counting.

Clast counting took place in two steps. First, the intermediate-axis diameter was measured for five clasts located along short transects oriented perpendicular to the main transect. The diameters of these clasts were then averaged to yield a single measurement along the main transect. Averaging of clasts in this way was necessary to improve the signal-to-noise ratio in the analysis. The eye does an excellent job at identifying bar-and-swale texture because it can sense many surface clasts at once. Measurements of single clasts along the main transect do not illustrate the bar and swale pattern well, however, because the presence of some small clasts on bars obscures the pattern. This problem can be rectified by averaging the sizes of many clasts perpendicular to the main transect. Second, clast-averaging was repeated for each point along the main transect, separated by a 20 cm spacing. This spacing value is also used as the spatial lag in the autocorrelation analysis. The clast-diameter transects obtained in this way are plotted in Figure 4 for each of the photo-mosaics, along with their corresponding autocorrelation functions. Although Figure 4 plots the entire autocorrelation function at all lags, only the average value of the lag-1 and lag-2 autocorrelation values (i.e. 20–40 cm spacing) was used to quantify the pavement development p . As surface age increases, the value of the autocorrelation function at lags between 20 and 40 cm decreases from $\rho_{20-40} = 0.45$ on Qa6 to $\rho_{20-40} = 0.38$ on Qa5 to $\rho_{20-40} = -0.02$ (i.e. indistinguishable from white noise) on Qa4.

Numerical Modeling Design and Behavior

The goal of this section is to translate this conceptual model of pavement formation into a numerical model aimed at understanding the timescales of desert-pavement formation and healing. The numerical model is designed specifically to illustrate the 'life cycle' of desert-pavement formation and its co-evolutionary relationship with the underlying eolian epipedon, and to generate hypotheses that can be tested in the field. Wainwright *et al.* (1999) was the first to construct a model of desert pavement formation, but their model assumed desert pavements to be erosional in origin. As such, their model is not applicable to the inflationary desert pavements most commonly observed in the southwestern US.

The cumulated eolian epipedon is represented by a steadily accumulating layer of thickness h (cm) and deposition rate e (cm/yr) in the model:

$$\frac{dh}{dt} = e \quad (2)$$

The surface clast motion takes place by a complex set of processes that are difficult to quantify. In our model, we approximate the integrated effects of clast-moving processes with a pavement-formation rate k that increases with epipedon thickness. We assume that k increases rapidly as the epipedon first begins to accumulate, then flattens out to a maximum value as the epipedon reaches a characteristic value related to the mean diameter of surface clasts. Mathematically, we assume that the rate of pavement formation k (yr⁻¹) has an S-shaped dependence on epipedon thickness h :

$$k = \begin{cases} \frac{k_{\max}}{2} \left(\frac{2h}{h_c} \right)^2 & \text{if } h < \frac{h_c}{2}, \\ k_{\max} - \frac{k_{\max}}{2} \left(\frac{2(h - h_c)}{h_c} \right)^2 & \text{if } h \geq \frac{h_c}{2} \end{cases} \quad (3)$$

Equation (3) states that the rate of pavement formation increases quadratically with h for low h values, then asymptotically approaches its maximum value of k_{\max} at a critical epipedon thickness h_c (Figure 1(A)). This mathematical expression is not unique, however, and other functions (or more process-based modeling) could be used to express the positive correlation between h and k . The relationship in (3) assumes that thin epipedons are relatively ineffective at moving clasts of a given size until a certain critical thickness is achieved. Above this thickness, the increase in pavement-formation rate per unit thickness steadily decreases. The specific value of h_c for a given surface depends on the mean surface clast diameter and on the specific clast-moving processes. All else being equal, pavements formed on initially gravel-dominated parent material will require a thicker epipedon (i.e. a larger h_c value) to achieve the same clast mobility compared with pavements developed on sand-dominated parent material. As such, an increase in parent-material grain size can be represented in the model by a larger value of h_c . The variable k_{\max} predominantly

reflects the amplitude of climatic variability. Climatic regimes with more frequent wetting–drying and freeze–thaw cycles may be represented in the model with higher k_{\max} values.

Clast mobility in nature may depend on the overall epipedon thickness (which may be very sandy) or the thinner, vesicular, silt-dominated A_v -horizon thickness that sometimes characterizes the upper portion of a desert epipedon, or both, depending on the texture of the epipedon. In the Fortymile Wash study site, sand from the active channels of Fortymile Wash contributes to a thick, sandy epipedon. The relatively coarse silty-sand texture of these epipedons most likely results in little expansion and contraction, however, compared with the much thinner A_v horizon. Our model does not resolve the epipedon and A_v horizons separately, but instead combines them into a single clast-moving eolian layer related to pavement-formation rate k through the S-shaped curve in (3). As such, the ‘epipedon thickness’ in the model may, for some study sites, be more closely approximated by the A_v -horizon thickness.

Pavement development in the model depends both on the value of k and on the difference between the pavement and its ideal state:

$$\frac{dp}{dt} = k(p_{\max} - p), \quad (4)$$

where p_{\max} represents the measure of pavement development corresponding to an ideal pavement. The variable p is a measure of pavement development, varying from an initial value of p_{\min} to a maximum value of p_{\max} . The specific values of p_{\min} and of p_{\max} reflect local conditions. For example, if pavement development is quantified using the fraction of clast coverage, p_{\min} is the parent-material clast fraction. The value of p_{\max} for a bare surface will usually be unity, but continuous pavement disturbance (e.g. by vegetation) may lower p_{\max} locally.

The term $p_{\max} - p$ in (4) represents the gradual reduction in unoccupied pavement sites as the pavement develops. Early on in the pavement-formation ‘life cycle’, clast motion on the surface leads to rapid pavement formation because there are many unoccupied sites for a clast to be lodged and sutured into the pavement. As the pavement matures, however, the number of unoccupied sites becomes progressively smaller as the pavement approaches an ideal state. As a result of this process, the same value of k leads to progressively slower pavement development as the pavement matures. The same ‘diminishing returns’ occurs when pavement development is characterized by a reduction in bar-and-swale texture (as in the Eagle Mountain study site). In such cases, pavement development is associated with the randomizing effect of clast motions, which gradually destroys the bar-and-swale textural ‘order’ inherited from alluvial depositional processes. Early on in pavement formation, when the bar-and-swale texture is pronounced, nearly every clast movement contributes to a reduction in textural ‘order’. As the pavement matures and the clast arrangement becomes more random, subsequent clast movements have less of a randomizing influence. This effect is also represented by the $p_{\max} - p$ term.

The model behavior is illustrated in Figure 5(A) for a representative set of model parameters. The straight line labeled by h represents a linear increase in epipedon thickness with time (Equation (1)) using $e = 0.2$ cm/kyr and zero initial thickness. Assuming a linear increase in eolian epipedon thickness is an approximation to the natural system, in which changes in aridity, vegetation cover, regional streamflow characteristics and playa moisture contribute to variations in the regional eolian deposition rate (McFadden *et al.*, 1998).

Eolian deposition rates also vary regionally as a function of distance from playa and fluvial sources as well as prevailing wind directions, but 0.2 cm/kyr is a reasonable value for Holocene deposition (Reheis *et al.*, 1995). The S-shaped curve labeled by k represents the relationship between pavement-formation rate and epipedon thickness (Equation (3)) using $h_c = 5$ cm and $k_{\max} = 0.002$ yr^{−1}. The curve labeled by p represents pavement development starting from a minimum value of p_{\min} , increasing to a maximum of p_{\max} . The plot is normalized to apply to any value of p_{\min} and p_{\max} .

The value of k is small during the early stage of pavement development, reflecting the limited ability of a thin epipedon to promote surface clast motion. As the epipedon thickens, however, the rate of pavement development rapidly increases. Eventually, the number of sites available for clast emplacement (i.e. the $p_{\max} - p$ term) decreases the rate of pavement development as the pavement approaches its ideal state. The result is an S-shaped curve broadly similar to the shape of the k curve, but with a significantly shorter timescale. The timescale for pavement development can be quantified using the interval of time between the initial surface formation ($t = 0$) and the time when the pavement becomes 50% developed (i.e. $(p - p_{\min})/(p_{\max} - p_{\min}) = 0.5$). For the parameter values in Figure 1(A), the 50% pavement-formation time is 5 kyr. The results shown in Figure 5(A) (using $e = 0.2$ cm/kyr, $h_c = 5$ cm and $k_{\max} = 0.002$ yr^{−1}) are referred to as the ‘reference case’ for comparison with other model results.

The effects of differing eolian deposition rate are illustrated in Figure 5B. In this example, the deposition rate is equal to 0.1 cm/kyr, or one-half of the value in Figure 5A. The timescale for 50% pavement formation is 8.5 kyr in this example. This value is slightly less than twice the value of the pavement-formation timescale for the previous example, shown in Figure 5(A).

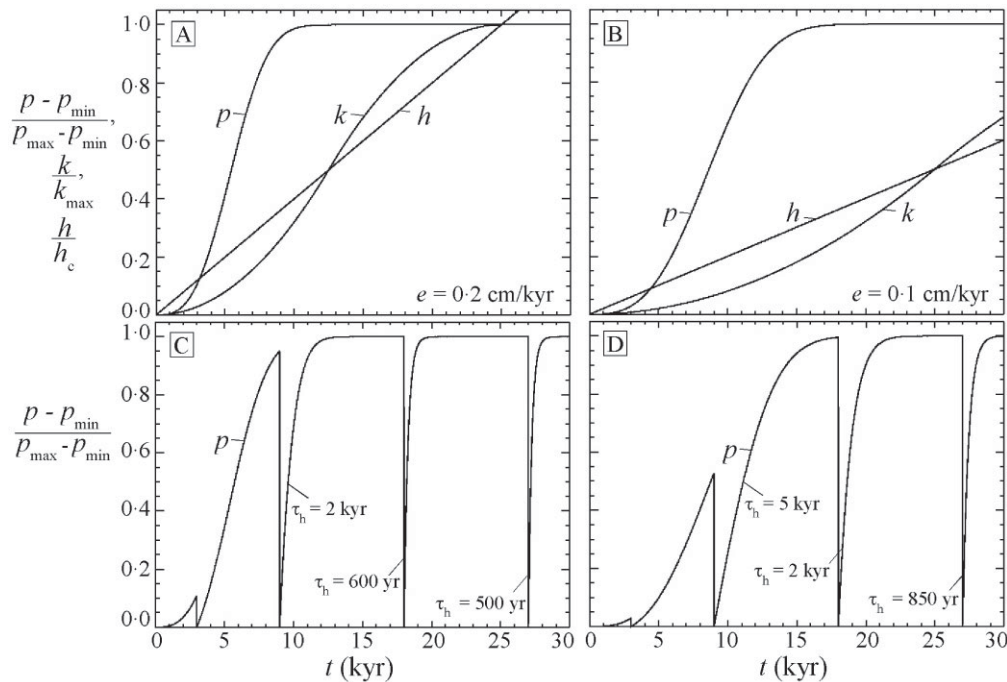


Figure 5. Plots of normalized pavement development $(p - p_{\min})/(p_{\max} - p_{\min})$, development rate k/k_{\max} and A_v-horizon thickness h/h_c as a function of time in the numerical model. (A) Results for the reference case of $e = 0.2$ cm/kyr, $h_c = 5$ cm and $k_{\max} = 0.002$ yr⁻¹. (B) Results for the same values as (A), but with a lower deposition rate $e = 0.1$ cm/kyr. (C), (D) Plots of normalized pavement development for the same model runs as (A) and (B), respectively, with pavement erasure at $t = 3$ kyr and every 9 kyr thereafter. As the A_v horizon thickens, the healing time τ_h decreases. These results suggest that pavement formation time and healing time can vary by one to two orders of magnitude.

Pavement response to a hypothetical mechanical disturbance is illustrated in Figure 5(C) and (D). These graphs illustrate pavement development through time using the same model parameters as in Figure 5(A) and (B), respectively, except that the pavement is assumed to be completely erased at $t = 3$ kyr, and periodically every 9 kyr thereafter, without affecting the underlying epipedon. This hypothetical pavement erasure is analogous to a pavement-healing experiment (see, e.g., Haff and Werner, 1996). In each case of simulated pavement disturbance, the pavement rebounds to an ideal state with a timescale that decreases as the epipedon thickens. In Figure 5(A), for example, the timescale for pavement healing decreases from a high value of $\tau_h = 2$ kyr to a low value of $\tau_h = 500$ yr. These results illustrate that pavement formation and healing can occur on vastly different timescales, controlled by where within the pavement 'life cycle' the disturbance occurs.

The model sensitivity to the values of h_c and k_{\max} is illustrated in Figure 6(A) and (B) respectively. Figure 6(A) shows the model result for the same parameters as the reference case (Figure 1(A)) but using $h_c = 7$ cm instead of $h_c = 5$ cm. The results of Figure 6(A) show that increasing the value of h_c results in a corresponding increase in pavement formation time. This example demonstrates the effects of coarser pavement material, because a thicker epipedon is required to move larger clasts under otherwise similar conditions. Increasing the value of k_{\max} from 0.002 to 0.003 yr⁻¹ decreases the pavement formation time, mimicking the effect of more variable climatic conditions that lead to more frequent and/or larger-amplitude clast motions.

The results of the model sensitivity analysis are summarized in Figure 7. In this figure, the 50% pavement-formation time τ_f is plotted as a function of e , h_c and k_{\max} . Each plot represents the model results obtained by varying each parameter value over the plot domain, keeping the other parameters the same as the reference case of Figure 5(A). The plot labeled by e , for example, graphs τ_f values corresponding to $h_c = 5$ cm, $k_{\max} = 0.002$ yr⁻¹, with e values ranging from 0.05 to 1 cm yr⁻¹. The strongest controlling variable in the model is the eolian deposition rate e . The k_{\max} parameter follows the same inverse relationship with τ_f as e does, but the dependence of τ_f on k_{\max} is not quite as strong as with e . Increasing the value of h_c results in τ_f values that increase approximately as the square root of h_c .

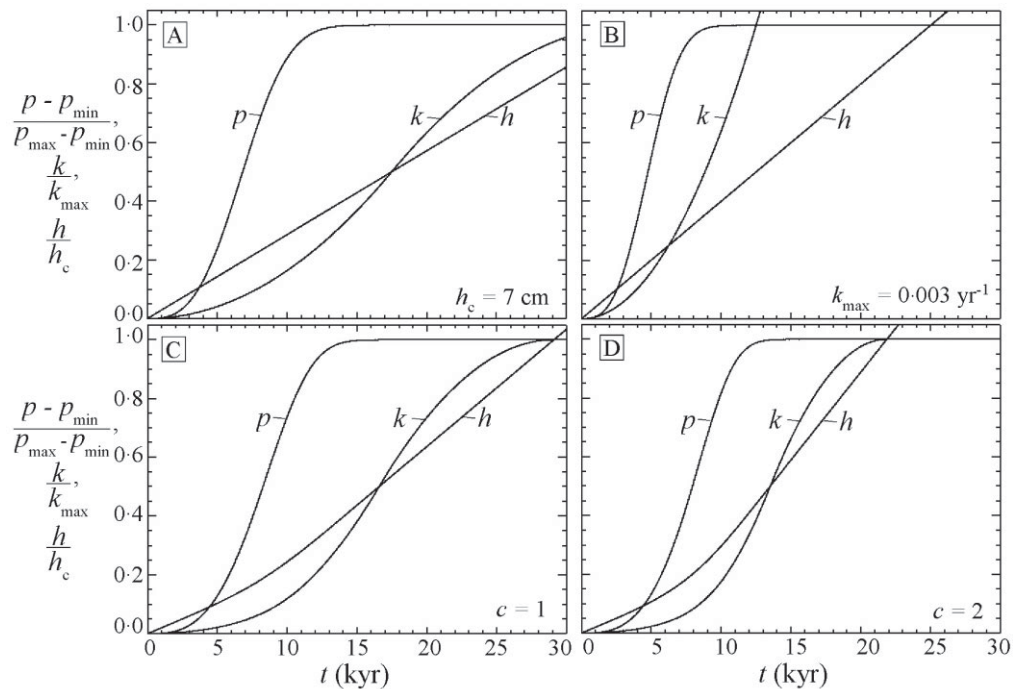


Figure 6. Plots of normalized pavement development $(p - p_{\min})/(p_{\max} - p_{\min})$, development rate k/k_{\max} and A_v -horizon thickness h/h_c as a function of time in the numerical model. (A) Results for the reference case of Figure 1(A) but with a larger value of $h_c = 7$ cm, illustrating the delayed pavement development in cases of coarser parent material. (B) Results for the reference case of Figure 1(A) but with a larger value of $k_{\max} = 0.003 \text{ yr}^{-1}$, illustrating the effects of a climatic regime with more frequent or larger-magnitude expansion/contraction events. (C) Results for the reference case but with a feedback between pavement development and eolian deposition added (Equation (4)) with $c = 1$. (D) Results for the reference case but with $c = 2$.

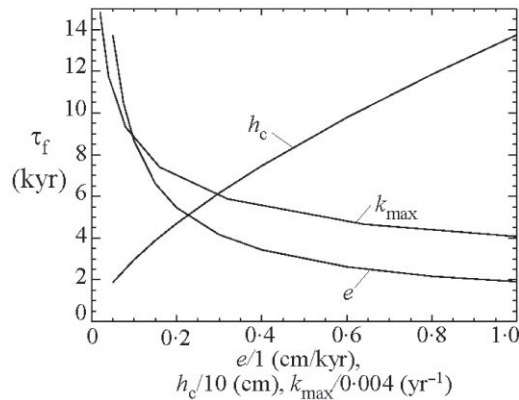


Figure 7. Plots of 50% pavement formation time τ_f versus normalized model parameters, illustrating the model sensitivity to each parameter. Formation time increases sublinearly with eolian deposition rate e and inversely with characteristic A_v -horizon thickness h_c and maximum development rate k_{\max} .

One potentially important feature of pavement development neglected in the model is a feedback between pavement development and eolian deposition rate. As a pavement develops, its ability to trap eolian material generally increases (Goossens, 1995). This effect is difficult to quantify, but one approach is to make the rate of eolian deposition an explicit function of p :

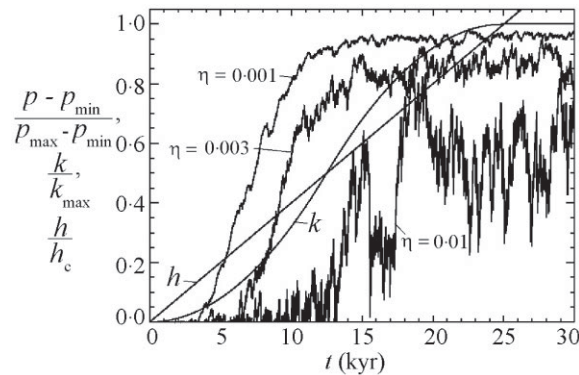


Figure 8. Plots of model results for the reference case ($e = 0.2 \text{ cm kyr}^{-1}$, $h_c = 5 \text{ cm}$ and $k_{\max} = 0.002 \text{ yr}^{-1}$) with random disturbances in p included. Increasing the magnitude of disturbance ($\eta = 0.001$, 0.003 and 0.01) results in a lower maximum pavement development and delayed development.

$$\frac{dh}{dt} = e(1 + c(p - p_{\min})/(p_{\max} - p_{\min})) \quad (5)$$

Equation (5) assumes that the eolian deposition rate increases linearly with pavement development. For example, if $c = 1$, then a fully developed pavement accumulates dust 100% faster than the newly abandoned alluvial surface. Figure 7(C) and (D) illustrates the effects of the feedback term on the model, using (5) in place of (2) and $c = 1$ and $c = 2$, respectively. The presence of the feedback term decreases the pavement-formation time, but not significantly. Even for a large value of $c = 2$ (i.e. the mature pavement captures 200% more dust than the original surface), the pavement-formation time is lowered only by about 10% compared with the results in Figure 6(A).

The effects of random pavement disturbances are illustrated in Figure 8. Episodic events (e.g. opportunistic vegetation growth or overland flows) continually disturb pavement development in many areas. Random disturbance was simulated in the model by reducing the value of p by a random number evenly distributed between 0 and η for each time step in the model (i.e. 1 yr). The underlying epipedon was not disturbed. For a relatively small disturbances ($\eta = 0.001$), pavement development follows a similar curve as in Figure 1(A), except that the 'ideal' pavement has a lower p value, reflecting the dynamic steady state between disturbance and healing that keeps the pavement slightly away from its ideal state. In addition to the lower p_{\max} value, the pavement formation time τ_f is lengthened with the introduction of random variability. As the magnitude of the variability increases (i.e. $\eta = 0.003$ and 0.01 in Figure 8), the value of p_{\max} decreases and τ_f increases.

Model Calibration with Field Measurements

Plots of the fraction clast coverage and textural randomness are shown in Figure 9 for the study areas. Fortymile Wash fan sites were divided into upper and lower fan sites (Figure 9(A) and (B)) and treated separately in the analysis. The vertical error bars are the standard deviations between different samples on the same surface unit. The horizontal error bars correspond to the age range given by Whitney *et al.* (2004) for each surface based on available age control.

The measured field data were fitted to a curve with a single exponential timescale given by

$$p = p_{\min} + (p_{\max} - p_{\min})(1 - e^{-\sqrt{2}t/\tau_f}). \quad (6)$$

Equation (6) is the solution to (4) assuming a constant value for k and written in terms of the 50% pavement formation time τ_f used in Figure 8. Equation (6) is a simplification of the full model but it has the advantage of fewer free parameters. The best-fit parameters for the upper Fortymile Wash fan are $\tau_f = 5.7 \text{ kyr}$, $p_{\min} = 0.25$ and $p_{\max} = 0.73$. The value of p_{\max} can be determined visually based on the asymptotic trend of the data. The remaining two parameters are determined using the Levenberg–Marquardt algorithm, a nonlinear least-squares curve-fitting routine (Press *et al.*, 1992). The best-fit values for the lower fan are $\tau_f = 8.4 \text{ kyr}$, $p_{\min} = 0.05$ and $p_{\max} = 0.53$. These results indicate that the lower fan has a smaller parent-material clast frequency since both the initial and final clast coverages are approximately 20% smaller on the lower fan compared with the upper fan. This pattern is consistent with downstream fining.

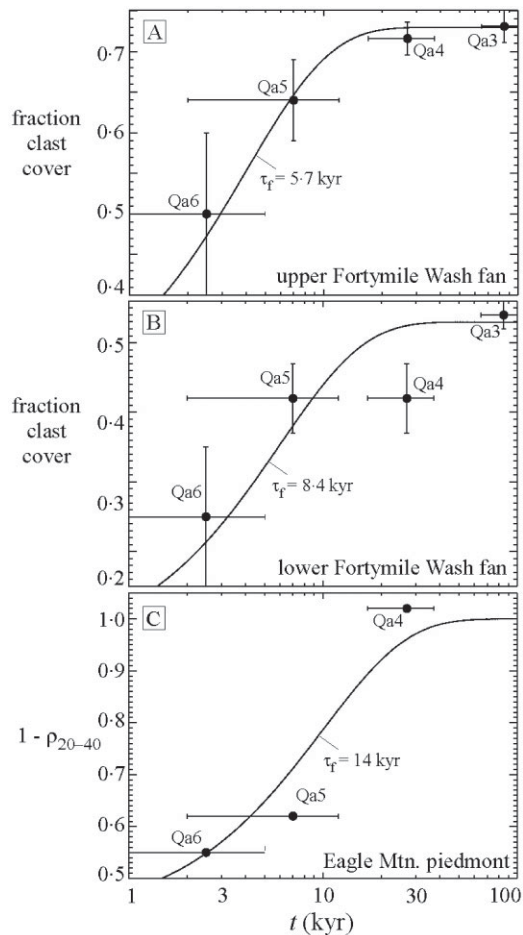


Figure 9. Plots of pavement development for Qa6–Qa3 surfaces of Fortymile Wash fan and Eagle Mountain piedmont. (A) Plot of fraction clast coverage for upper Fortymile Wash fan surfaces (study-site locations in Figure 5(B)). Vertical error bars are the standard deviation between surfaces, horizontal error bars reflect the range in age control given by Whitney *et al.* (2004). A best fit to the data using (6) gives a pavement formation timescale of $\tau_f = 5.7$ kyr, $p_{\min} = 0.25$ and $p_{\max} = 0.73$. (B) Plot of fraction clast coverage for lower Fortymile Wash fan surfaces. A best fit to the data using (6) gives $\tau_f = 8.4$ kyr, $p_{\min} = 0.05$ and $p_{\max} = 0.53$. (C) Plot of $1 - \rho_{20-40}$ for the Eagle Mountain piedmont surfaces (study-site locations in Figure 5(A)). A best fit to the data using (6) gives $\tau_f = 14$ kyr, $p_{\min} = 0.42$ and $p_{\max} = 1.0$. No vertical error bars are given in (C) because only one site was analyzed for each surface unit.

The larger value for τ_f on the lower fan is not statistically significant given the error bars in the data and the range of τ_f values that can be adequately fitted to the data. The best-fit parameters for textural randomness on Eagle Mountain piedmont are $\tau_f = 14$ kyr, $p_{\min} = 0.42$ and $p_{\max} = 1.0$. All else being equal, we would expect τ_f values to be smaller on Eagle Mountain piedmont than Fortymile Wash because of its proximity to the active fine-grained dust source of Franklin Lake playa. The average clast size on Eagle Mountain piedmont is several times larger than that of Fortymile Wash, however. Model results suggest that larger pavement clasts require a thicker epipedon to initiate surface clast motion, and hence develop more slowly. These competing effects result in a pavement-formation time on Eagle Mountain piedmont that is approximately twice as large as that of Fortymile Wash fan. It should also be noted, however, that surface coarsening on Fortymile Wash fan and bar-and-swale reduction on Eagle Mountain piedmont are driven by somewhat different processes and hence may not be quantitatively comparable. As a follow-up to this work, it would be interesting to measure pavement-formation times at several positions on Eagle Mountain piedmont downwind of Franklin Lake playa in order to test for a correlation between pavement-formation time and eolian deposition rate.

Discussion

Our results highlight the multi-scale nature of desert-pavement dynamics and provide a means for reconciling the disparate timescales observed in pavement formation and healing. Measurements at Fortymile Wash fan and Eagle Mountain piedmont show the 50% pavement-formation time to be approximately 5–10 kyr in these areas. Pavements can be useful surface-age indicators up to larger timescales, however, because pavements asymptotically approach an ideal state (e.g. $(p - p_{\min})/(p_{\max} - p_{\min}) = 0.5$ at $t = \tau_i$, $(p - p_{\min})/(p_{\max} - p_{\min}) \approx 0.75$ at $t = 2\tau_i$, $(p - p_{\min})/(p_{\max} - p_{\min}) \approx 0.875$ at $t = 3\tau_i$ etc.). The ‘saturation’ time for desert pavements as diagnostic age indicators, therefore, is several times larger than τ_i .

Pavement-formation times may be longer or shorter at other sites depending on parent-material texture, eolian deposition rate and other factors. In areas of fine-grained parent material downwind of active playa sources, for example, well developed pavements may form on newly abandoned alluvial surfaces in only a few thousand years. The sensitivity of pavement development to eolian deposition rate in our model suggests that pavement-formation times may vary strongly with distance from nearby dust sources, prevailing-wind direction and through time with climatic variations. Pelletier and Cook (2005) mapped the spatial distribution of dust deposition downwind of Franklin Lake playa over Quaternary timescales and showed that deposition rates decrease by approximately a factor of two for every 1 km of distance. Given that playas are typically separated by 10–20 km in the Basin and Range, these results imply that eolian deposition rates vary by at least an order of magnitude depending on distance from nearby playas and prevailing-wind directions. Pavement development, therefore, may not be a reliable relative-age indicator over regional spatial scales where eolian deposition rates vary greatly. This is consistent with the results of Quade (2001), who clearly demonstrated locations in Las Vegas Valley where well developed pavements had formed on early-to-mid-Holocene alluvial surfaces. Previous work had generally assumed that strongly developed pavements were indicative of late Pleistocene surface age or older.

Several studies suggest that pavement healing can take place up to 100 times faster than pavement formation. Haff and Werner (1996), for example, conducted experiments in the Mojave Desert that showed average resurfacing rates of 6.2% over 5 years, with lower resurfacing rates for larger plots. These results imply pavement-healing times of 80 yr, which is significantly faster than the pavement formation times inferred for our study areas. We propose that the fast healing observed in these studies can be associated with the presence of a mature underlying eolian epipedon. This hypothesis may be tested using pavement-healing experiments with and without epipedon removal.

Our model results illustrate the dynamic steady state between mature pavements and continuous vegetative disturbance. Even in the presence of continuous disturbance (e.g. bioturbation by annual grasses), pavements undergo a life cycle dictated by the accumulation of their underlying eolian epipedon. In these cases, pavements achieve a steady-state balance between disturbance and healing characterized by a pavement of less-than-ideal quality that nevertheless returns rapidly towards an ideal state once it is disturbed. These results may help to interpret those of recent studies emphasizing the effect of vegetative disturbance on pavement development. Quade (2001), for example, documented a strong inverse correlation between fraction clast coverage and elevation greater than 400 m in Amargosa and neighboring valleys. Quade interpreted his results in terms of pavement disturbance by Pleistocene mature vegetation (e.g. piñon and ponderosa pine, and juniper), because this type of vegetation reached a low elevation of about 400 m at the last glacial maximum. The results of our study suggest that pavements are more likely to be in dynamic equilibrium with modern brushy vegetation (which also strongly correlates with elevation), rather than being a relict of Pleistocene mature vegetation, because such rapid pavement healing is possible in the presence of a mature eolian epipedon. This interpretation is consistent with Wood *et al.* (2005), who documented a correlation between vegetation density and clast coverage at constant elevation, implying a dynamic steady state between pavements and modern vegetation.

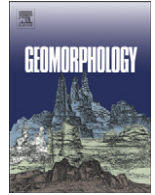
Our work has implications for understanding and predicting desert-surface response to anthropogenic activity. Qualitatively, our results suggest that desert pavements are able to recover over human timescales if the underlying eolian epipedon is preserved. Even if disturbance completely eliminates the clast coverage from the surface, our results suggest that an intact epipedon should promote healing at the rates similar to those observed by Haff and Werner (1996).

Acknowledgements

We gratefully acknowledge financial support from the Yucca Mountain Project, the US Army Research Office Terrestrial Sciences Program (grant No. W911NF-04-1-0266) and the US Geological Survey Earth Surface Processes Program. C. Harrington and J. Cook provided helpful conversations and field assistance. We thank M. Eppes and an anonymous referee for helpful reviews.

References

- Al-Farraj A, Harvey AM. 2000. Desert pavement characteristics on wadi terrace and alluvial fan surfaces: Wadi Al-Bih, U.A.E. and Oman. *Geomorphology* **35**: 279–297.
- Amit R, Gerson R, Yaalon DH. 1993. Stages and rate of the gravel shattering process by salts in desert Reg soils. *Geoderma* **57**: 295–324.
- Anderson K, Wells S, Graham R. 2002. Pedogenesis of vesicular horizons, Cima volcanic field, Mojave Desert, California. *Soil Science Society of America Journal* **66**: 878–887.
- Box GEP, Jenkins GM, Reinsel GC. 1994. *Time Series Analysis Forecasting and Control*, 3rd edn. Prentice-Hall: Englewood Cliffs, NJ.
- Bull WB. 1991. *Geomorphic Responses to Climatic Change*. Oxford University Press: New York.
- Corte AE. 1963. Particle sorting by repeated freezing and thawing. *Science* **142**: 499–501.
- Czarnecki JB. 1997. *Geohydrology and Evapotranspiration at Franklin Lake Playa, Inyo County, California*, U.S. Geological Survey Water Supply Paper 2377. Reston, VA.
- Eppes ME, Harrison JBJ. 1999. Spatial variability of soils developing on basalt flows in the Portillo volcanic field, southern New Mexico: prelude to a chronosequence study. *Earth Surface Processes and Landforms* **24**: 1009–1024.
- Goossens D. 1995. Effect of rock fragments on eolian deposition of atmospheric dust. *Catena* **23**: 167–189.
- Haff PK. 2005. Response of desert pavement to seismic shaking, Hector Mine earthquake, California, 1999. *Journal of Geophysical Research* **110**: FO2006. DOI: 10.1029/2003JF000054
- Haff PK, Werner BT. 1996. Dynamical processes on desert pavements and the healing of surficial disturbances. *Quaternary Research* **45**: 38–46.
- Hsu L, Pelletier JD. 2004. Correlation and dating of Quaternary alluvial fan surfaces using scarp diffusion. *Geomorphology* **60**: 319–335.
- Inglis DR. 1965. Particle sorting and stone migration by freezing and thawing. *Science* **148**: 116–1617.
- Marchetti DW, Cerling TE. 2005. Cosmogenic ³He exposure ages of Pleistocene debris flows and desert pavements in Capitol Reef National Park, Utah. *Geomorphology* **67**: 423–435.
- Matmon A, Nichols K, Finkel R. 2006. Isotopic insights into smoothing of abandoned fan surfaces, Southern California. *Quaternary Research* **66**: 109–118.
- Mayer L, Bull WB. 1981. Impact of Pleistocene–Holocene climatic change on particle size distribution of fan deposits in southwestern Arizona. *Geological Society of America Abstracts with Programs* **13**: 95.
- McFadden LD, Eppes MC, Gillespie AR, Hallet B. 2005. Physical weathering in arid landscapes due to diurnal variation in the direction of solar heating. *Geological Society of America Bulletin* **117**: 161–173.
- McFadden LD, McDonald EV, Wells SG, Anderson K, Quade J, Forman SL. 1998. The vesicular layer and carbonate collars of desert soils and pavements: formation, age, and relation to climate change. *Geomorphology* **24**: 101–145.
- McFadden LD, Ritter JB, Wells SG. 1989. Use of multi-parameter relative-age estimates for age estimation and correlation of alluvial fan surfaces on a desert piedmont, Eastern Mojave Desert, California. *Quaternary Research* **32**: 276–290.
- McFadden LD, Wells SG, Jercinovich MJ. 1987. Influences of eolian and pedogenic processes on the origin and evolution of desert pavements. *Geology* **15**: 504–508.
- Pelletier JD, Cook, JP. 2005. Deposition of playa windblown dust over geologic time scales. *Geology* **33**: 909–912.
- Press WH, Teukolsky SA, Vetterling WT, Flannery BP. 1992. *Numerical Recipes in C the Art of Scientific Computing*, 2nd edn. Cambridge University Press: New York.
- Prose DV, Wilshire HG. 2000. *The Lasting Effect of Tank Maneuvers on Desert Soils and Intershrub Flora*, U.S. Geological Survey Open-File Report 00-512. United States Geological Survey: Reston, VA.
- Quade J. 2001. Desert pavements and associated rock varnish in the Mojave Desert: how old can they be? *Geology* **29**: 855–858.
- Reheis MC, Goodmacher JC, Harden JW, McFadden LD, Rockwell TK, Shroba RR, Sowers JM, Taylor EM. 1995. Quaternary soils and dust deposition in southern Nevada and California. *Geological Society of America Bulletin* **107**: 1003–1022.
- Springer ME. 1958. Desert pavement and vesicular layer of some soils of the desert of the Lahontan Basin, Nevada. *Proceedings of the Soil Science Society of America* **22**: 63–66.
- Valentine GA, Harrington CD. 2006. Clast size controls and longevity of Pleistocene desert pavements at Lathrop Wells and Red Code volcanoes, southern Nevada. *Geology* **34**: 533–536.
- Wainwright J, Parsons AJ, Abrahams AD. 1999. Field and computer simulation experiments on the formation of a desert pavement. *Earth Surface Processes and Landforms* **24**: 1025–1037.
- Wells SG, Dohrenwend JC, McFadden LD, Turrin BD, Mahrer KD. 1985. Late Cenozoic landscape evolution on lava flow surfaces of the Cima volcanic field, Mojave Desert, California. *Geological Society of America Bulletin* **96**: 1518–1529.
- Wells SG, McFadden LD, Dohrenwend JC. 1987. Influence of late Quaternary climatic changes on geomorphic and pedogenic processes on a desert piedmont, Eastern Mojave Desert, California. *Quaternary Research* **27**: 130–146.
- Wells SG, McFadden LD, Poths J, Olinger CT. 1995. Cosmogenic ³He surface-exposure dating of stone pavements: implications for landscape evolution in deserts. *Geology* **23**: 613–616.
- Whitney JW, Taylor EM, Wesling JR. 2004. Quaternary stratigraphy and mapping in the Yucca Mountain area. In *Quaternary Paleoseismology and Stratigraphy of the Yucca Mountain area, Nevada*, U.S. Geological Survey Professional Paper 1689, Keefer WR, Whitney JW, Taylor EM (eds). United States Geological Survey: Reston, VA; 11–23.
- Wood YA, Graham RC, Wells SG. 2005. Surface control of desert pavement pedologic processes and landscape function, Cima volcanic field, Mojave Desert, California. *Catena* **59**: 205–230.



Controls on the height and spacing of eolian ripples and transverse dunes: A numerical modeling investigation

Jon D. Pelletier

Department of Geosciences, The University of Arizona, 1040 E. Fourth St., Tucson, Arizona, 85721, USA

ARTICLE INFO

Article history:

Received 14 June 2008

Received in revised form 14 October 2008

Accepted 16 October 2008

Available online 28 October 2008

Keywords:

Eolian geomorphology

Ripples

Dunes

Numerical modeling

ABSTRACT

Ripples and transverse dunes in areas of abundant sand supply increase in height and spacing as a function of time, grain size, and excess shear velocity. How and why each of these factors influence ripple and transverse dune size, however, is not precisely known. In this paper, the controls on the height and spacing of ripples and transverse dunes in areas of abundant sand supply are investigated using a numerical model for the formation of eolian bedforms from an initially flat surface. This bedform evolution model combines the basic elements of Werner's [Werner, B.T., 1995. Eolian dunes: Computer simulations and attractor interpretation. *Geology* 23, 1107–1110.] cellular automaton model of dune formation with a model for boundary layer flow over complex topography. Particular attention is paid to the relationship between bed shear stress and slope on the windward (stoss) side of evolving bedforms. Nonlinear boundary layer model results indicate that bed shear stresses on stoss slopes increase with increasing slope angle up to approximately 20°, then decrease with increasing slope angle as backpressure effects become limiting. In the bedform evolution model, the linear boundary layer flow model of Jackson and Hunt [Jackson, P.S., Hunt, J.C.R., 1975. Turbulent wind flow over a low hill. *Quarterly Journal of the Royal Meteorological Society* 101, 929–955.], generalized to 3D, is modified to include the nonlinear relationship between bed shear stress and slope. Bed shear stresses predicted by the modified Jackson and Hunt flow model are then used to predict rates of erosion and deposition iteratively through time within a mass conservative framework similar to Werner [Werner, B.T., 1995. Eolian dunes: Computer simulations and attractor interpretation. *Geology* 23, 1107–1110.]. Beginning with a flat bed, the model forms ripples that grow in height and spacing until a dynamic steady state condition is achieved in which bedforms migrate downwind without further growth. The steady state ripple spacing predicted by this model is approximately 3000 times greater than the aerodynamic roughness length of the initially flat surface, which is a function of grain size and excess shear velocity. Once steady state ripples form, they become the dominant roughness element of the surface. The increase in roughness associated with ripple formation triggers the same bedform instability that created ripples, causing dunes to form at a larger scale. In this way, the numerical model of this paper suggests that ripples and dunes are genetically linked. Transverse dunes in this model have a steady state height and spacing that is controlled by the effective roughness length of the rippled surface, which is shown to be on the order of 500 times greater than the original roughness length, but varies significantly with the details of ripple morphology. The model predictions for ripple and dune spacing and their controlling variables are consistent with field measurements from the published literature. The model of this paper provides a preliminary process based understanding of the granulometric control of ripples and dunes in areas of abundant sand supply and unidirectional prevailing winds, and it argues for a genetic linkage between ripples and dunes via a scaling relationship between eolian bedform size and the aerodynamic roughness length.

© 2008 Elsevier B.V. All rights reserved.

1. Introduction

1.1. Problem statement

Eolian bedforms are constructed by a positive feedback in which incipient, small amplitude perturbations modify the air flow around them to cause spatial variations in erosion and deposition that pro-

mote taller and more widely spaced bedforms over time. How this process works at small (ripple) and large (dune) scales, however, is still not well understood and a number of questions remain. First, field measurements indicate that the height and spacing of ripples are positively correlated with grain size and excess shear velocity (Sharp, 1963; Walker, 1981) and that the height and spacing of transverse dunes are also positively correlated with grain size in areas of abundant sand supply (Wilson, 1972; Lancaster, 1988). How and why these factors influence bedform size, however, is not precisely known. Moreover, it is still unclear whether dunes grow in size indefinitely, or

E-mail address: jon@geo.arizona.edu.

whether, after an initial period of growth, they achieve a dynamic steady state condition in which they migrate downwind without further growth. In this paper we take a numerical modeling approach to addressing these questions, integrating the cellular automaton model of [Werner \(1995\)](#) with a realistic boundary layer flow model in order to investigate the coupling between boundary layer flow and bedform evolution at both small and large scales. The model results suggest that boundary layer flow processes set a limit on bedform size.

In this paper, I describe a process based numerical model designed to determine the controls on the height and spacing of ripples and dunes. The model combines the strengths of the [Werner \(1995\)](#) model framework, which successfully generates self organized bedforms from an initially flat surface, with the [Schwammle and Herrmann \(2004\)](#) framework, which successfully quantifies the positive feedback between topography, air flow, and erosion/deposition during bedform evolution. In this paper I focus on the simplest case of ripple and dune development in areas of abundant sand supply (i.e. 100% sand cover). Also, the model assumes unidirectional winds and does not explicitly include variable grain sizes or sorting effects. In focusing on this simple, idealized case, it is not my intention to imply that the effects of limited sand supply, shifting winds, and/or spatial and temporal variations in grain size are unimportant in natural dunes. Rather, my goal is to understand the coupling between boundary layer flow and bedform evolution for this simple case first before adding additional complexity.

1.2. Field and remote sensing observations

There are three fundamental types of transverse eolian bedforms that form in areas of abundant sand supply and unidirectional prevailing winds. Ripples occur at the smallest scale and are typically spaced from 0.01–10 m and have heights of 0.2–50 cm, with higher, more widely spaced ripples forming in areas with stronger winds and/or coarser sand ([Sharp, 1963](#); [Wilson, 1972](#)). Dunes are the next level in the bedform hierarchy and achieve spacings of 10–1000 m and heights of 0.5–50 m. At still larger scales, megadunes may form and reach heights of 50–300 m and spacings of 1–3 km, given sufficient time in addition to sand supply. Working in the large sand seas of the Sahara Desert, [Wilson \(1972\)](#) documented a positive correlation between the grain diameter of the coarsest twentieth percentile of crestal sand and the height and spacing of each bedform type ([Fig. 1](#)). Working in the Skeleton Coast, Namib, and Gran Desierto sand seas, [Lancaster \(1988\)](#) documented a correlation between dune spacing and grain size in compound crescentic (i.e. transverse) dunes. The spacing of barchan, star, and longitudinal dunes in Lancaster's study areas did not show any correlation with grain size.

One way that grain size may affect the size of ripples and dunes is via the aerodynamic roughness length. The aerodynamic “law of the wall” states that the wind velocity profile above a rough surface is a function of the aerodynamic roughness length, which, during sal-

tation, is a function of both grain size and excess shear velocity ([Sherman, 1992](#)). Therefore, if the spacing of bedforms is controlled in a significant way by the wind velocity profile above the bed, it is reasonable to hypothesize that the size of bedforms will be partially controlled by grain size and excess shear velocity. This is the fundamental hypothesis investigated in this paper.

In ripples, spacing is well established to increase with increasing grain size and excess shear velocity ([Sharp, 1963](#); [Walker, 1981](#); [Andreotti et al., 2006](#)), although there is still no process based understanding of how those variables control spacing. [Bagnold \(1941\)](#) performed the pioneering work on the height and spacing of eolian ripples. He proposed that ripples form by an instability mechanism in which a small, incipient perturbation in the bed topography exposes the windward side to more impacts and faster surface creep than the leeward side, resulting in more grains being ejected into saltation. In his theory, sand grains move a characteristic saltation distance, resulting in periodic ripples with spacing equal to that characteristic distance. The fact that ripple spacing increases over time in both field and laboratory experiments ([Sharp, 1963](#); [Seppala and Linde, 1978](#); [Walker, 1981](#)), however, is inconsistent with Bagnold's concept of a constant characteristic saltation length. Moreover, experimental studies of grain impacts suggest that a wide distribution of energies are imparted to grains on the bed during each impact, resulting in a wide distribution of saltation path lengths ([Mitha et al., 1986](#)). Using a discrete particle framework informed by [Mitha et al.'s \(1986\)](#) work, [Anderson \(1987\)](#) and [Anderson and Bunas \(1993\)](#) constructed models for ripple formation and evolution aimed at understanding the controls on ripple height and spacing. [Anderson \(1987\)](#) argued that ripple spacing is controlled by the mean reputation length. Anderson's model is a linear stability analysis, however, and hence only addresses the spacing of ripples early on in their development from a flat surface. [Anderson and Bunas \(1993\)](#) modeled the evolution of ripples using the distribution of particle paths documented by [Mitha et al. \(1986\)](#), together with a simplified boundary layer flow model. In their model, ripples grow in height and spacing until a steady state condition is achieved. The steady state behavior in their model, however, was directly related to an arbitrary “ceiling” imposed on the flow in their model. As a result, there is currently no realistic model for ripples that predicts a steady state relationship between grain size and excess shear velocity control ripple size, as observed.

The controls on the spacing of dunes are also incompletely understood. As noted above, [Wilson \(1972\)](#) and [Lancaster \(1988\)](#) both documented positive correlations between grain size and dune height and dune spacing. On the other hand, tests of granulometric control of bedform height and spacing in barchan, star, and longitudinal dunes all show no grain size control (e.g. [Wasson and Hyde, 1983](#); [Lancaster, 1988](#); [Ould Ahmedou et al., 2007](#); [Elbelrhiti et al., 2008](#)). It is important to distinguish between dunes formed in areas of abundant sand supply from those formed in areas of limited sand supply in this context, however. In areas of limited sand supply (i.e. partial sand cover), the aerodynamic roughness length will be at least partially controlled by the roughness elements (e.g. vegetation, alluvial deposits, and bedrock outcrops) that comprise the interdune or sand free areas. As the percent of sand cover decreases significantly below 100% in a dune field, the aerodynamic roughness length will become progressively more influenced by the size of the roughness elements in the interdune areas (which generally have no relationship with the grain size of sand on the dunes). For this reason, the height and spacing of barchan, star, and longitudinal dunes are not likely to exhibit granulometric control, even if the boundary layer flow over these types of dunes exerts a controlling influence on their morphology. For this reason, we will not consider those dune types in this paper.

Most conceptual models for eolian dune formation relate dune height and spacing to the dimensions of the zone of disturbance downwind (e.g. [Hanna, 1969](#); [Wilson, 1972](#); [Folk, 1976](#)). It is difficult to

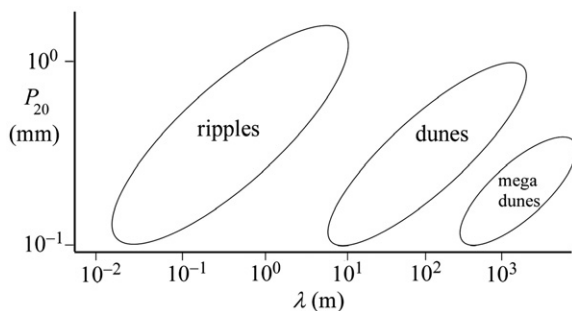


Fig. 1. Schematic plot of grain diameter of coarsest twentieth percentile crestal sand, P_{20} , and bedform spacing, λ , from transverse eolian bedforms of the Sahara Sand Seas. After [Wilson \(1972\)](#).

separate cause and effect in these conceptual models, however, because, it is unclear whether the size of the zone of separation controls, or is controlled by, dune size. Moreover, the size of the zone of separation is controlled by other parameters besides dune size and shape in ways that have not been fully quantified. For example, Howard et al. (1989) proposed that dune size is controlled, in part, by the aerodynamic roughness length upwind because it is this length scale that determines the speedup ratio on the windward side of dunes for a given dune height and aspect ratio. How the aerodynamic roughness length influences dune size, however, is still uncertain. Indeed, whether dune size is controlled primarily by the characteristics of boundary layer flow (e.g. Howard et al., 1989; Schwammle and Herrmann, 2004) or by the nonlinear dynamics intrinsic to interacting bedforms (e.g. Werner and Gillespie, 1993; Werner and Kocurek, 1999) is still debated.

1.3. Previous process based modeling work

Werner (1995) was the first to model the formation of eolian dunes numerically from an initially flat surface. Werner's (1995) model is based on the iterative entrainment, transport, and deposition of discrete units of sand that are picked up at random, transported multiples of a characteristic distance downwind, and redeposited back onto the surface. Sand units transported by the model during a given iteration are deposited on the bed with a probability that is low on bedrock surfaces relative to sandy surfaces (reflecting the higher coefficient of restitution of a hard bed versus a soft bed). Sand units that are not deposited are transported repeatedly downwind until deposition occurs. In this way, the local sand flux above the surface is directly proportional to the probability of deposition. In Werner's model, the effect of air flow over incipient dunes is included in a simplified way by defining "shadow" zones where the probability of deposition is one. Shadow zones are defined to be areas located in shadow when the surface is illuminated by a sun angle of 15° from the horizontal and parallel to the wind direction. In Werner's model, shadow zones provide a simplified representation of the recirculation

zone on the lee sides of incipient dunes where wind driven sediment flux is low and deposition rates are high. Sand units deposited back down on the bed in Werner's model roll down the direction of steepest descent if deposition causes an oversteepened condition (i.e. a slope angle greater than the angle of repose). Werner's model combines three basic elements that, taken together, are responsible for the complex self organized behavior observed in the model. First, the stochastic model of entrainment generates initially structureless, multi scale relief from an initially flat bed. Second, shadow zones provide a mechanism for a positive feedback between the topography of incipient bedforms and the spatial pattern of erosion and deposition that enhances bedform height and spacing over time. Finally, avalanching provides a limitation on dune slope and a mechanism for cross wind sand transport. Example output of Werner's model is illustrated in Fig. 2. The height and spacing of bedforms in Werner's model increase proportionately to the square root of time until a single dune, equivalent in size to the model domain, remains.

Werner's model is capable of reproducing the four principal dune types (transverse, barchan, star, and longitudinal) by varying sand supply and wind direction variability. Despite the success of Werner's model for understanding dune types, the model has limitations for understanding dune size. Werner's model includes the physics of boundary layer flow over topography only in a very limited way. For example, erosion on the stoss side of evolving bedforms is independent of both height and slope in Werner's model, an assumption that is inconsistent with basic field measurements (Lancaster, 1996). Werner's model also predicts symmetric topographic profiles when bedforms evolve in a unidirectional wind regime, while bedform profiles in nature are asymmetric under unidirectional wind conditions. Momiji et al. (2000) constructed a modified version of Werner's model capable of producing asymmetric bedforms by prescribing erosion on the windward side of bedforms to be a nonlinear function of slope. Nevertheless, both of these models have no prescribed length scale and they depend on parameters that are abstracted from the actual transport processes (e.g. saltation). As such, they are difficult to calibrate for comparison to real world bedforms (Baas, 2007).

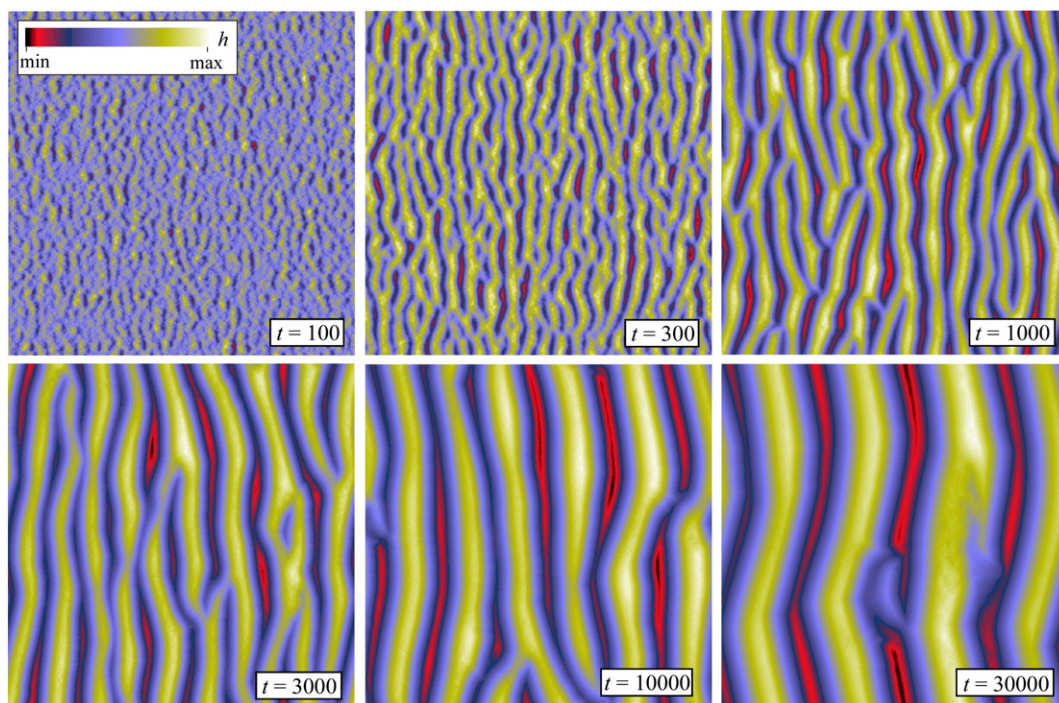


Fig. 2. Color maps of elevation predicted by Werner's model for dunes at $t=100, 300, 1000, 3000, 10,000$, and $30,000$ ($\times N^2$) time steps. Wind direction is from left to right. In the model, dune height and spacing increase proportionately to the square root of time until only one dune remains, equivalent in size to the model domain. Note that each color map is separately scaled so that black is the minimum height and white is the maximum.

Following upon Werner's work, Stam (1996, 1997), Van Dijk et al. (1999), and Schwammle and Herrmann (2004) developed numerical models that include the physics of boundary layer flow over evolving transverse bedforms. These models, in turn, followed upon an earlier generation of boundary layer flow models over barchan dunes (e.g. Wippermann and Gross, 1986). Stam's (1996, 1997) model was limited to 2D and could not be used to model the evolution of dunes from an initially flat bed (i.e. Stam's model predicted that the smallest wavelengths were the most unstable, leading to infinitely steep slopes). Given that the height and spacing of dunes depends on the interaction of bedforms and defects in 3D (e.g. Werner and Kocurek, 1999), it is unlikely that any 2D model will be sufficient to determine the controls on bedform height and spacing. In Van Dijk et al.'s (1999) and Schwammle and Herrmann's (2004) models, sine waves and small Gaussian hills were used as an initial conditions, respectively. As such, these models do not simulate bedform evolution from a structureless initial condition and hence they do not directly constrain the height and spacing of natural bedforms. Moreover, because both models require a characteristic bedform length L to be input into the model, the size of the bedforms produced by these models is, to some extent, prescribed by the input data. A comprehensive model of bedforms must predict bedform lengths rather than input them into the model.

All of the bedform evolution models that include boundary layer flow have used the Jackson and Hunt (1975) boundary layer model for flow over "low" hills as their foundation (later generalized to 3D by Mason and Sykes, 1979). This model, as well as subsequent Fourier Transform based models for boundary layer flow (i.e. Weng et al., 1991), solve the linearized Reynolds stress equations over prescribed bed topography. Boundary layer models based on linearized Fourier Transform techniques have the advantage of computational speed, thus allowing them to be integrated into bedform evolution models that require bed shear stresses to be calculated during each model time step for tens of thousands of time steps. More sophisticated computational fluid dynamics models (i.e. Large Eddy Simulation (LES) and Direct Numerical Simulation (DNS) methods) have the advantage of greater accuracy than linearized Reynolds' stress models, but they are too computationally intensive to be run for the tens of thousands of iterations required by bedform evolution models. Linearized Reynolds' stress models such as the Jackson and Hunt model do not adequately compute the stresses over steep ($>10^\circ$) bedforms, however. As such, these models must be modified to account for nonlinear flow effects over steep topography. Schwammle and Herrmann (2004), for example, incorporated the effects of flow separation over the lee sides of growing dunes by correcting a linearized Reynolds' stress model solution using a geometric model for the separation zone. Flow separation, however, affects the entire wind field, not just the zone of separation, hence a local correction does not fully account for the effects of nonlinear flow processes on bed shear stresses and erosion rates on the stoss sides of evolving bedforms.

Recent work has suggested that bedform spacing is controlled by the evolution of defects in bedform populations over time (Werner and Gillespie, 1993; Werner and Kocurek, 1997, 1999). The defect density model predicts that bedform height and spacing grows linearly with time from an initial value, then transitions to a logarithmic increase in time. While defect density and bedform spacing are strongly correlated during bedform development (suggesting that defect density directly controls height and spacing), it should be noted that this model makes a number of simplifying assumptions (e.g. bedforms are uniformly spaced and of uniform height, aerodynamics plays no role in bedform migration, and defects are not created over time). The defect density model is also limited in that it requires input data for the initial bedform spacing. This value largely determines the final bedform spacing predicted by the model.

2. Numerical modeling

2.1. Model description

At the start of each iteration of the model, the topography $h(x,y)$ is used as input to a boundary layer flow model that calculates the bed shear stresses over complex topography. This boundary layer model is a 3D version of the Jackson and Hunt (J&H) (1975) model for flow over low hills, modified to include the nonlinear effects of flow over steep topography. Bed shear stress in the J&H model, τ_b , can be written as the sum of the shear stress over flat topography, τ_{b0} , plus the normalized variation in bed shear stress induced by the variations in topography, τ_{b1} :

$$\tau_b = \tau_{b0}(1 + \tau_{b1}). \quad (1)$$

According to the J&H model, the Fourier Transform of the normalized variations in bed shear stress, $\hat{\tau}_{b1}$, is given by x and y components:

$$\hat{\tau}_{b1x}(k_x, k_y) = \varepsilon \kappa \frac{k_x^2}{|k|} \hat{h}(k_x, k_y) z_k \frac{K_1(z_k e^{i\phi})}{K_0(z_k e^{i\phi})}, \quad (2)$$

$$\hat{\tau}_{b1y}(k_x, k_y) = \varepsilon \kappa \frac{k_x k_y}{|k|} \hat{h}(k_x, k_y), \quad (3)$$

where

$$\phi = \begin{cases} +\pi/4 & (k_x \geq 0) \\ \pi/4 & (k_x < 0) \end{cases}, \quad (4)$$

and x is the downwind distance, y is the crosswind distance, ε is a dimensionless factor, κ is the von Karman constant (0.4), k is the wave number (with x and y components), $\hat{h}(k_x, k_y)$ is the Fourier Transform of the topography, z_k is

$$z_k = 2\sqrt{\frac{z_0}{l}} |k^*|, \quad (5)$$

K_0 is the modified Bessel function of zero order, K_1 is the modified Bessel function of first order, z_0 is the aerodynamic roughness length, l is a characteristic "inner layer" thickness given by

$$l \ln\left(\frac{l}{z_0}\right) = 2L\kappa^2, \quad (6)$$

k^* is the normalized wavenumber (i.e. kL) and L is the half length of the bedforms at the half height position (Jackson and Hunt, 1975). In most applications of the J&H model, where the goal is to calculate the flow over an isolated hill of prescribed size and shape, L is assumed to be constant. In this paper, where the goal is to model flow over evolving bedforms with a range of sizes, L changes with each Fourier coefficient, i.e. $L = \pi/2k_x$. Because the J&H model is linear (and hence solutions can be superposed), L can be allowed to vary in this way. The value of ε , a measure of the "strength" of the perturbation, is given by

$$\varepsilon = \frac{\ln^2\left(\frac{l}{z_0}\right)}{\kappa \ln\left(\frac{l}{z_0}\right)} \quad (7)$$

The J&H flow model includes only one intrinsic length scale: the aerodynamic roughness length z_0 . That is, for a given topography (i.e. the topography at a given time step in the bedform evolution model), $\hat{h}(k_x, k_y)$, L , and l are prescribed, and the nature of the flow over the topography, including the magnitude of the normalized bed shear stress variations, τ_{b1} , will depend only on the length scale z_0 .

The effect of the aerodynamic roughness length on the magnitude of bed shear stress variation over sinusoidal bedforms is illustrated in

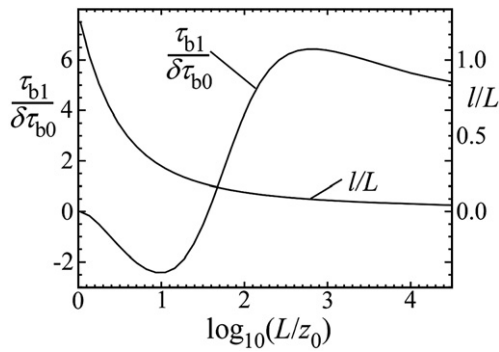


Fig. 3. Plots of normalized bed shear stress variations, $\tau_{b1}/\delta\tau_{b0}$, and normalized inner layer thickness, l/L , predicted by the Jackson and Hunt (1975) model versus the logarithm (base 10) of the ratio of the half height of the hill to the roughness length. This plot illustrates that the normalized bed shear stress variations reach a maximum when $L/z_0 \approx 500$.

Fig. 3. This figure plots the magnitude of the normalized bed shear stress variation, $\tau_{b1}/\delta\tau_{b0}$, as a function of the logarithm (base 10) of the ratio of the half length of the bedforms to the roughness length, $\log_{10}(L/z_0)$. The normalized bed shear stress, τ_{b1}/τ_{b0} , is scaled in this plot to the tangent of the maximum slope angle, δ . **Fig. 3** also plots the normalized inner layer thickness l/L computed by solving Eq. (4) iteratively. In order to interpret **Fig. 3**, let us first consider a sinusoidal bed of half length 10 cm and maximum slope 0.1. If the aerodynamic roughness length is relatively large (e.g., 1 mm, corresponding to $\log_{10}(L/z_0) = 2$), for example, **Fig. 3** shows that the value of $\tau_{b1}/\delta\tau_{b0}$ is approximately 4, hence $\tau_{b1}/\tau_{b0} = 0.4$. This means that the bed shear stress will increase by approximately 40% near the crest of sinusoidal bedforms according to this model, and decrease by approximately 40% near the trough. At smaller roughness lengths, e.g., $z_0 = 0.1$ mm, the value of $\tau_{b1}/\delta\tau_{b0}$ increases to approximately 6. This increase in bed shear stress is associated with the fact that, for relatively small roughness lengths, the wind velocities interacting with the bedforms will be greater (due to the higher velocity gradients associated with smaller roughness lengths), hence the degree of flow compression/expansion will also be greater. At still smaller roughness lengths, however, e.g., $z_0 = 0.01$ mm, the value of $\tau_{b1}/\delta\tau_{b0}$ actually decreases to slightly more than 5. This decrease is associated with the increase in form drag and backpressure that limit near surface wind velocities compared to the cases with lower L/z_0 ratios (Wood and Mason, 1993). The shape of this plot illustrates that, for a given topography, there is a certain value of z_0 that maximizes the variations in bed shear stress over sinusoidal bedforms. If the ratio L/z_0 is too low, the bed shear stress variations are small because the bedforms are too small to experience the high velocity winds that occur far from the bed. If the

ratio L/z_0 is too large, backpressure effects act to limit the bed shear stress. In between these two extremes, an optimal condition exists where the bedforms are tall enough (relative to the roughness length) to drive significant flow compression and expansion but not so tall that backpressure and form drag become a limiting factor. In addition to the magnitude of bed shear stress variations, the roughness length also controls the phase shift between the bed shear stress and the topography. For larger values of z_0 , the maximum of bed shear stress is shifted further upwind from the bedform crest.

The J&H flow model is a linear model that is accurate to within a few percent only for maximum slopes less than approximately 0.2 (i.e. $\approx 10^\circ$). Because mature bedforms commonly attain slope angles close to or equal to the angle of repose, some modification to the J&H model is necessary in order to model the development of ripples and dunes. Schwammle and Herrmann (2004), for example, modified the bed shear stress predicted by the J&H model on the lee side of growing dunes using a geometric model for the region of flow separation. This approach neglects the effect of flow separation (and of drag induced backpressure more generally) on the rest of the boundary layer. Consider the case of flow over steep ramps (forward and backward facing), illustrated in **Fig. 4**. In the forward facing case, we can expect the normalized bed shear stress or speedup ratio above the ramp to increase with increasing ramp angle, at least for small angles. This is because flow lines converge as the flow moves over the step, causing higher velocity gradients and bed shear stresses. In the extreme case of a vertical step, however, the flow will stagnate behind the step and the speedup ratio will be lower than that of a flat surface. In that case, the stagnation zone in front of the step leads to a low shear stress because of the backpressure that develops behind the zone of stagnant flow. Between these two extreme cases, there must be some transition from increasing bed shear stress to decreasing bed shear stress as the ramp slope increases. The J&H model, however, predicts an increasing bed shear stress for all slopes. Although the J&H model does include the backpressure effects associated with gentle slopes, it is clear that the J&H model (or any other linear model) does not include the transition of increasing bed shear stresses to decreasing bed shear stresses as slope angle increases and nonlinear flow effects become dominant.

In order to quantify the nonlinear relationship between bed shear stresses and bed slope, I computed the boundary layer flow over forward and backward facing ramps of various inclinations using the Nonlinear Mixed Spectral Finite Difference Model (NLMSFD) of Xu et al. (1994). This model has been used successfully to quantify the nonlinear effects of flow separation on speedup ratios over sinusoidal topography (Ayotte and Hughes, 2004; Ayotte, 2008). The open circles in **Fig. 4** represent the maximum bed shear stress on the inclined portion of the ramp predicted by the NLMSFD model, with a step height of 10 cm and a roughness length of 1 mm. These results indicate

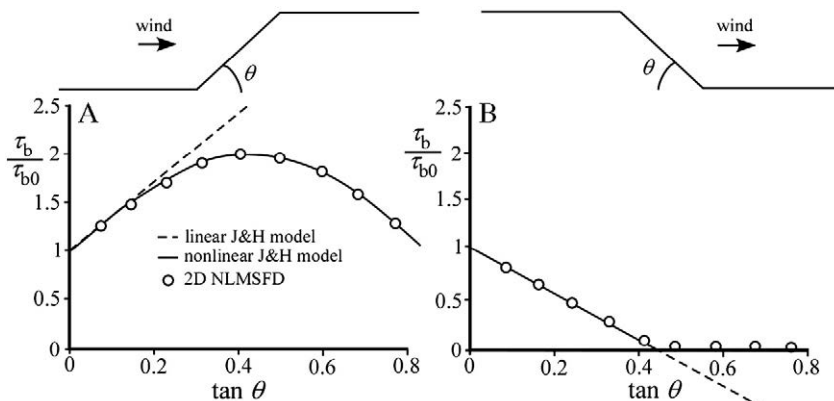


Fig. 4. Plots of peak normalized bed shear stress, τ_b/τ_{b0} , over (A) forward and (B) backward-facing steps according to the Jackson and Hunt model (dashed line), modified, nonlinear Jackson and Hunt model of this paper (solid curve, see text for details), and 2D Nonlinear Mixed Spectral Finite Difference (NLMSFD) model of Xu et al. (1994).

that the maximum bed shear stress on a forward facing ramp initially increases linearly with slope $\tan \theta$, following the prediction of the J&H model closely until $\tan \theta \approx 0.2$. As $\tan \theta$ increases, the bed shear stress reaches a maximum value at $\tan \theta \approx 0.4$ and then decreases as backpressure becomes a dominant factor. In the backward facing step case, the NLMSFD results follow the predictions of the J&H model closely until separation occurs at $\tan \theta \approx 0.4$. At larger slopes, the bed shear stress remains close to zero in the nonlinear model, while the linear model predicts negative bed shear stresses.

The NLMSFD model is too computationally intensive to be run in 3D during each time step of the bedform evolution model. Therefore, some abstraction of the results of the NLMSFD model must be used. Results from the NLMSFD model suggest a way in which the J&H model can be corrected for nonlinear effects over steep topography. In this modified model, which I refer to as the “modified, nonlinear J&H model,” the local bed shear stress predicted by the linear model, τ_b , is modified by the local slope in the downwind direction, $\partial h / \partial x$, according to a parabolic function:

$$\tau_{b,nl} = \tau_b \left(1 - 2 \left(\frac{\partial h}{\partial x} \right)^2 \right) \quad \text{if } \frac{\partial h}{\partial x} > 0, \quad (8)$$

where the subscript nl refers to the nonlinear modification. Fig. 4 shows that Eq. (8) closely follows the trend observed in the NLMSFD results for the case of the forward facing step. The precise shape of the nonlinear transition plotted in Fig. 4 and represented empirically by Eq. (8) will vary as a function of the shape of the step and the aerodynamic roughness length, however. As such, Eq. (8) is only an approximation based on representative NLMSFD results for flow over abrupt changes in slope. In the backward facing ramp case, it is appropriate to modify the bed shear stress predicted by the linear model by making the stress equal to zero if the predicted value is less than zero, i.e.

$$\tau_{b,nl} = 0 \quad \text{if } \tau_b < 0. \quad (9)$$

Eq. (9), which is not plotted in Fig. 4 because it follows the linear model until the bed shear stress is equal to zero and then follows the x axis at $\tau_b = 0$ for higher values of $\tan \theta$, closely follows the trend observed in the NLMSFD results for the case of a backward facing step.

Once the bed shear stress is computed, the bedform evolution model computes the flux at each grid point, q_x , using the relationship

$$q_x = \begin{cases} c \tau_b^{1/2} (\tau_b - \tau_{bt}) & \text{if } \tau_b \geq \tau_{bt} \\ 0 & \text{if } \tau_b < \tau_{bt} \end{cases}, \quad (10)$$

where τ_{bt} is the threshold shear stress for entrainment and c is a coefficient that quantifies the bed erodibility and is primarily a function of grain size. The value of c is set to 1 in the model for simplicity. As a result, the units of time in the model are arbitrary. The threshold bed shear stress for entrainment, τ_{bt} , is given by

$$\tau_{bt} = \tau_{bt0} \frac{S_c + \frac{\partial h}{\partial x}}{S_c \sqrt{\left(\frac{\partial h}{\partial x} \right)^2 + 1}}, \quad (11)$$

where τ_{bt0} is the threshold bed shear stress for entrainment on a flat bed, given by

$$\tau_{bt0} = A^2 (\rho_s - \rho) g D, \quad (12)$$

S_c is the tangent of the angle of repose (0.67), A is the entrainment coefficient (equal to 0.1 for air flow over a sandy bed), ρ_s is the sediment density, g is the acceleration due to gravity, and D is the grain size (Bagnold, 1936). The threshold shear stress over flat topography, τ_{bt0} , can be introduced into the model most simply by defining the threshold to be a ratio, α , of the applied shear stress over the initially flat topography, i.e. $\alpha = \tau_{bt0} / \tau_{b0}$. Topography influences

sediment transport over bedforms in two separate ways. First, topographic variations cause flow compression and expansion that increase or decrease bed shear stress, as represented in the modified, nonlinear J&H model. Eq. (11) indicates that topography influences sediment transport through an additional mechanism, however. The local slope of the bed changes the threshold shear stress necessary to entrain sediment (e.g., less bed shear stress is required to entrain sediment from a lee slope due to the sloping geometry of the surface) (Howard, 1977; Hardisty and Whitehouse, 1988; Willetts and Rice, 1988; Iversen and Rasmussen, 1999). This additional topographic control on sediment transport has been neglected in recent bedform evolution models (e.g. Stam 1996, 1997; Schwammler and Herrmann, 2004) by assuming $\tau_{bt} \gg \tau_{bt0}$.

The bedform evolution model of this paper integrates the boundary layer flow and sediment transport models described above with a modified version of Werner's (1995) bedform evolution model. In the model, all of the length scales in the problem are scaled to z_0 . As such, the value of z_0 in the model is set to 1 and the height and spacing of bedforms produced by the model have units that are multiples of z_0 . In this way, the model represents the feedbacks between topography, air flow, and erosion and deposition in a scale independent way. To scale the bedform heights and spacings predicted by the model to actual units, one needs only to multiply the model predictions for height and spacing by a specific value of z_0 .

In Werner's model, sand units are picked up at random and transported a unit distance l_s downwind. In the present model, sand units are entrained with a probability p_e that depends on the local flux q_x in the direction of the wind, with a coefficient p_0 :

$$p_e = p_0 q_x. \quad (13)$$

Following downwind transport of the sand unit a distance l_s , the sand unit falls back to the bed with a probability p_d that also depends on flux according to:

$$p_d = p_0 (1 - q_x) \quad (14)$$

Because Eqs. (13) and (14) relate the probabilities of entrainment and deposition linearly to q_x , the time averaged flux in the model is proportional to q_x . The value of p_0 is chosen such that $p_e = 1$ $p_d \approx 0$ on the lee sides of well developed bedforms (i.e. in zones of flow recirculation where transport is predominantly by avalanching) and $p_e = 1$ $p_d \approx 1$ on stoss sides. Since q_x varies from approximately 0 (in recirculation zones) to as high as 2.5 (on the stoss sides of mature bedforms), a value of p_0 between 0.3 and 0.4 is an appropriate default value. Finally, as in Werner's model, avalanching occurs if the entrainment or deposition of any sand unit causes an oversteepened condition (i.e. a local slope angle in excess of 33°), and the avalanching sand units are transported in the direction of steepest descent.

The bedform evolution model of this paper is fully defined with six parameters: N , the number of grid points in the x and y directions; Δx , the width of an individual grid point; Δh , the height of an individual sand unit; l_s , the displacement unit of each sand unit; p_0 ; and α . All of the length scales in the model are scaled to the fundamental length scale of the problem, z_0 . For the model results presented here, I use $N = 256$, $\Delta x = 500 z_0$, $\Delta h = 25 z_0$, $l_s = \Delta x$, $p_0 = 0.33$, and $\alpha = 0$ unless otherwise noted. Time in the model is measured by the number of time steps normalized by the total number of grid points N^2 . Varying the values of Δh , l_s , and/or p_0 in the model affects how quickly bedforms develop, but not the resulting geometry (height and spacing) of those bedforms. If the value of Δh is lowered, for example, the model exhibits smaller fluctuations in sediment transport, hence more time is required for the instability to develop. Varying Δx changes the model resolution but does not change the geometry of bedforms as long as individual bedforms are sufficiently well resolved.

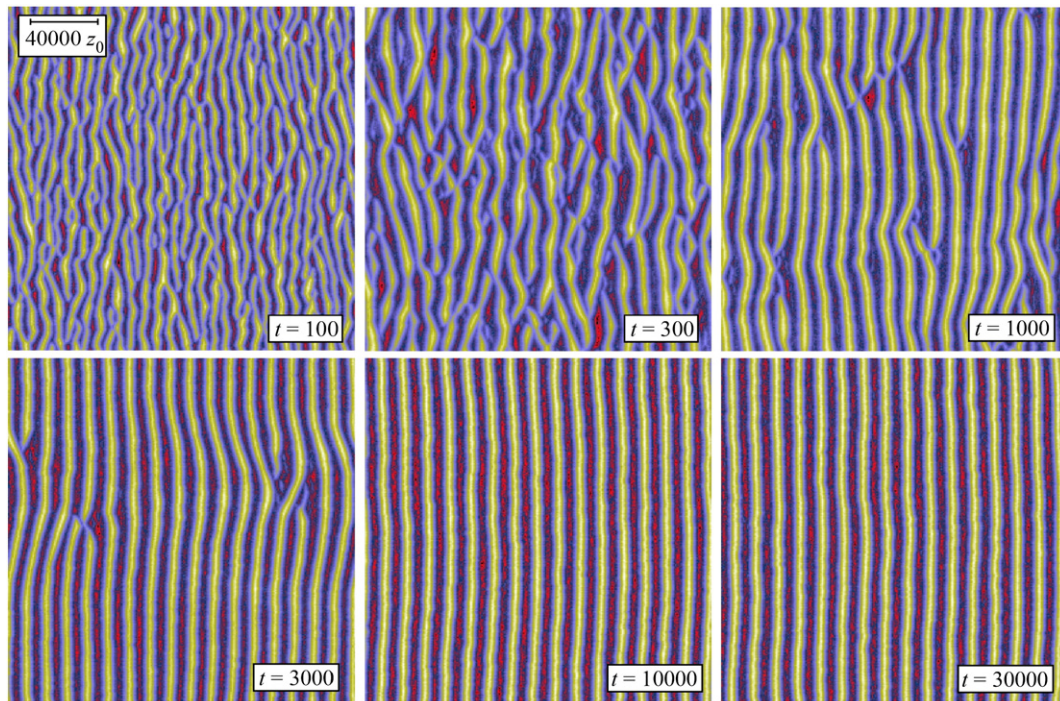


Fig. 5. Color maps of elevation predicted by the bedform evolution model with the linear Jackson and Hunt boundary layer flow model at $t = 100, 300, 1000, 3000, 10,000$, and $30,000$ ($\times N^2$) time steps. In the model, bedform spacing and crest line length increase until a steady-state condition is achieved after $t \approx 1000 \times N^2$ time steps.

2.2. Model results

In order to determine the effects of the nonlinear relationship between windward speedup ratio and bed shear stress on bed slope, let's first consider a “control” model run with a version of the bedform evolution model that uses the linear J&H flow model. Parameters for this run are $N=256$, $\Delta x=1000z_0$, $\Delta h=50z_0$, $l_s=\Delta x$, $p_0=0.33$, and $\alpha=0$. Fig. 5 illustrates color maps of the surface topography predicted by this

version of the bedform evolution model. A scale bar is included in the upper left corner of the figure and the wind direction is from left to right. Early on in the model run, narrowly spaced bedforms are created with short crest lines and a high defect density. Over time, bedform height, spacing, and crest line length all increase while defect density decreases. After $t \approx 1000 \times N^2$, the model achieves a steady state condition in which there is no further growth in height or spacing. In steady state, the model predicts that bedform spacing is equal to approximately 10,000 times

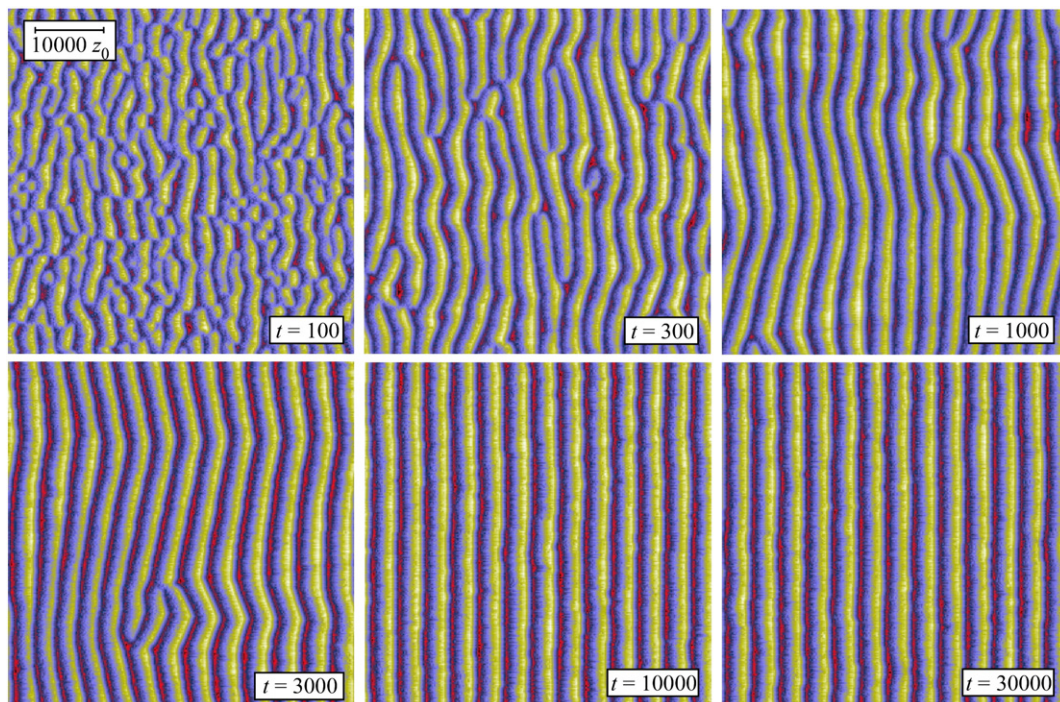


Fig. 6. Color maps of elevation predicted by the bedform evolution model with the modified (nonlinear) Jackson and Hunt boundary layer flow model at $t = 100, 300, 1000, 3000, 10,000$, and $30,000$ ($\times N^2$) time steps. In the model, bedform spacing and crest line length increase until a steady-state condition is achieved after $t \approx 1000 \times N^2$ time steps.

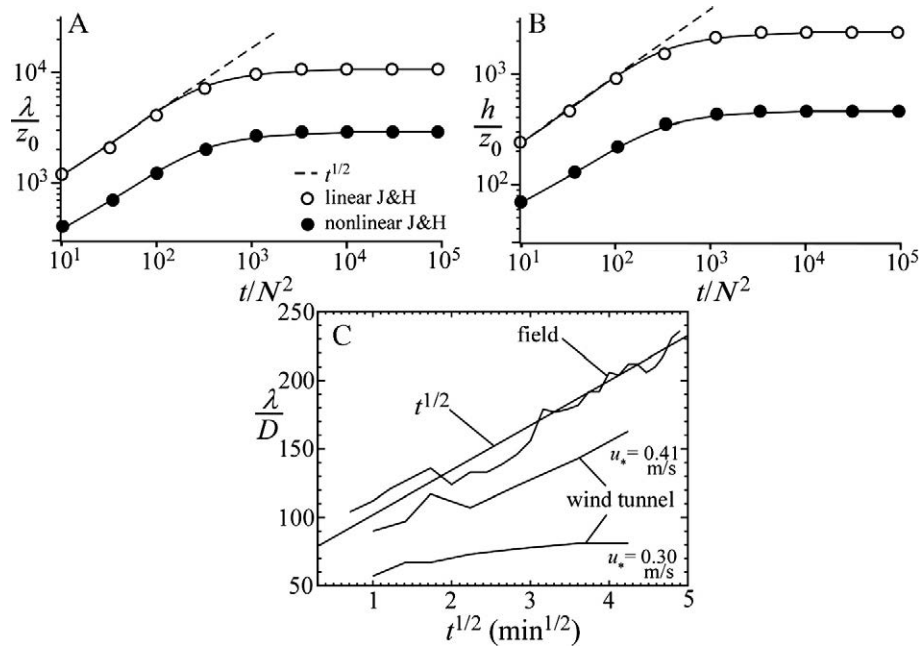


Fig. 7. Plot of (A) normalized spacing, λ/z_0 , and (B) normalized height, h/z_0 , versus time for the bedform evolution model with the linear Jackson and Hunt model (open circles) and the modified, nonlinear version (close circles) based on an average of ten simulations. Early in the model, height and spacing grow proportionately to the square root of time (dashed line), but eventually reach a steady-state condition in which height and spacing do not increase significantly with time. (C) Field and wind tunnel experiments on ripple formation showing that bedform spacing closely follows the square root relationship observed in the model for short time scales.

the roughness length ($\lambda \approx 10,000z_0$) and bedform height is approximately 3000 times the roughness length ($h \approx 3000z_0$). This behavior is illustrated in Fig. 7, which shows that the spacing and height of bedforms both increase proportionately to the square root of time until a steady state condition is achieved. The achievement of a steady state condition in this model can best be understood as a balance between two competing effects that relate migration rate to bedform height. In Werner's (1995) model, bedform migration rate is inversely proportional to bedform height. Over time, smaller bedforms migrate faster than larger bedforms, causing bedforms to coalesce over time with no preferred length scale. Hence, bedform size increases as a power law over time with no maximum size. It should also be emphasized that the increase in bedform height and spacing in Werner's model continues even after all of the defects have been removed from the system. In contrast, bedform migration rate in this model is influenced by bedform height in two independent ways. As in Werner (1995), taller bedforms migrate more slowly due to the increase in cross sectional surface area to volume ratio with increasing height (which causes migration rate to be inversely proportional to height if slopes are constant). Taller bedforms, however, are subject to greater speedup ratios and bed shear stresses for a given width (within a certain range of λ/z_0), causing taller bedforms to migrate faster than they do in Werner's model. This boundary layer flow effect does not only depend on the height of the migrating bedform, but also on the heights of bedforms upwind and downwind via boundary layer interactions. The existence of a steady state height and spacing in the model is related to a competition between these two opposing effects. As with Werner's (1995) model, however, this model is also limited in that it predicts symmetric bedform profiles (i.e. both the stoss and lee slopes achieve angles close to the angle of repose). Including a finite threshold shear stress (i.e. $\alpha > 0$) in the model does not measurably change the size of the resulting bedforms.

Figs. 6 and 7 illustrate the corresponding results for the bedform evolution model with modified, nonlinear J&H flow. The relationship between bedform spacing and time in this version of the model is broadly similar to that of the linear model illustrated in Fig. 5. Over time, bedform height, spacing, and crest line length all increase while defect density decreases. After $t \approx 1000 \times N^2$, this model also reaches a steady state condition. In contrast to the linear J&H model, however, bedforms

in this model are asymmetric, with slope angles of $\approx 20^\circ$ on the stoss slopes and close to 33° on the lee slopes (Fig. 8). In steady state, this model predicts that bedform spacing is equal to approximately 3000 times the roughness length ($\lambda \approx 3000z_0$) and bedform height is approximately 600 times the roughness length ($h \approx 600z_0$). This version of the bedform evolution model is clearly the preferred version, both because it incorporates a flow model with more realistic nonlinear effects and because it leads asymmetric bedform topographic profiles similar to those observed in nature (Fig. 8). Including a finite threshold shear stress (i.e. $\alpha > 0$) in this version of the model also does not measurably change the size of the resulting bedforms, but the shape of the bedforms do change. The model predicts lower stoss slopes and bedform aspect ratios with higher values of α .

2.3. Application to ripples

Available data on the growth of ripple spacing versus time is consistent with the square root dependence on time observed in the model prior to steady state. Fig. 7C illustrates ripple spacing data from

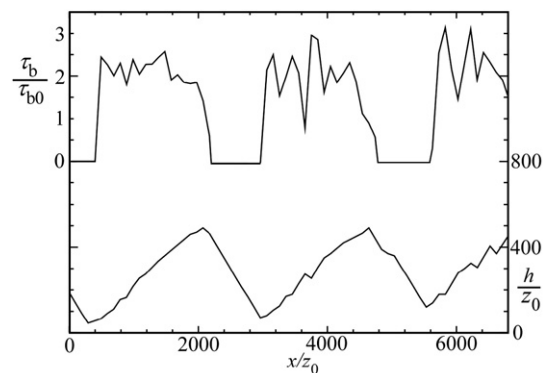


Fig. 8. Plot of normalized bed shear stress and topography as a function of downwind distance predicted by the bedform evolution model with the modified, nonlinear Jackson and Hunt flow model. Bedforms are asymmetric, with maximum slope angles on the stoss side of $\approx 15^\circ$ and maximum angles on the lee side of 33° .

a 25 minute field experiment of ripple formation and two wind tunnel experiments performed at different shear velocities. [Werner and Gillespie \(1993\)](#) used this data to support a logarithmic increase in ripple spacing versus time, but they fitted their model to only a portion of the data. [Fig. 7C](#) shows that, in the case of the field experiment and the wind tunnel experiment with high shear velocity (i.e. $u_* = 0.41 \text{ m s}^{-1}$), the entire dataset closely follows the $t^{1/2}$ dependence, consistent with the model of this paper and with the cellular automaton model of [Werner \(1995\)](#). The field and laboratory measurements were acquired over too short a duration to document the transition to steady state, however. The results of the wind tunnel experiment performed at lower shear velocity (i.e. $u_* = 0.30 \text{ m s}^{-1}$) is not consistent with a square root dependence on time. This could be due to a transition to steady state. The limited resolution of the data, however, makes it difficult to reach any firm conclusion.

Next we evaluate the model prediction for the steady state spacing of ripples formed on an initially flat surface. On a flat surface with active saltation, the aerodynamic roughness length is a function of the grain size and the excess shear velocity. Using measured values of z_0 , D , and u_* from the literature, [Sherman \(1992\)](#) proposed the following expression:

$$z_0 = \frac{D}{15} + C_m \frac{(u_* - u_{*t})^2}{g} \quad (15)$$

where C_m is an empirical, dimensionless parameter and

$$u_{*t} = A \sqrt{\frac{\rho_s}{\rho} g D} \quad (16)$$

In the first term on the right side of Eq. (13), grain size influences roughness because grains are the discrete units from which the bed is composed and larger grains produce rougher microtopography and hence greater drag on the boundary layer whether or not saltation is occurring. During saltation (i.e. when $u_* - u_{*t} > 0$), an additional “saltation induced” roughness occurs, represented by the second term on the right side of Eq. (15). The magnitude of this effect increases with the excess shear velocity, because higher values of excess shear velocity cause greater saltation. [Sherman \(1992\)](#) constrained the value of C_m to be 0.025 from 99 data points, the large majority of which were measured in wind tunnels. More recently, [Sherman and Farrell \(2008\)](#) used an analysis of an expanded dataset of 291 data points to propose a value of $C_m = 0.132$ for field conditions. [Sherman and Farrell \(2008\)](#) documented that measurements of z_0 from wind tunnels are, on average, approximately an order of magnitude lower than those measured in the field, due to the effects of flow confinement in wind tunnels. This is the reason why the value for C_m in field conditions (0.132) is so much larger than the originally proposed value (0.025).

Eq. (15), together with the fundamental scaling of bedform height and spacing to roughness length predicted by the bedform evolution model of this paper, provides the technical basis for predicting the dependence of ripple spacing on grain size and shear velocity in the field ([Sharp, 1963; Wilson, 1972](#)) and in the laboratory ([Walker, 1981; Andreotti et al., 2006](#)). It should be noted that natural sand beds have a range of grain sizes and it is possible that coarser grains have greater influence on aerodynamic roughness than median sized grains. For this reason, many field studies of the granulometric control of ripple and dune spacing have used the grain size of the coarsest 20th percentile (e.g. [Wilson, 1972; Lancaster, 1988](#)) instead of the mean grain diameter, D , when testing the granulometric control of bedform size. Here we will use Eq. (15) to estimate the roughness length during ripple formation for comparison to measured data, even if the measured data report P_{20} values, bearing in mind that values of D may be significantly lower than values of P_{20} .

[Fig. 9A](#) plots the predictions of the model for a range of values of the grain diameter and shear velocity, along with field measurements of

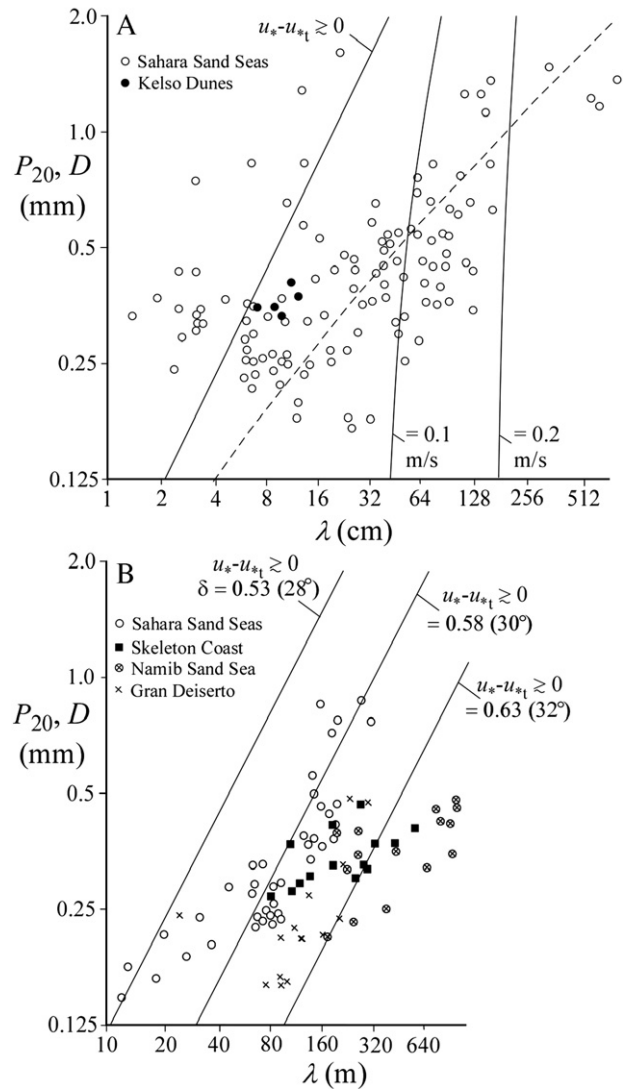


Fig. 9. Plots of P_{20} and D versus bedform spacing for (A) ripples and (B) dunes. (A) Data from [Wilson \(1972\)](#) (P_{20} reported, open circles) and [Sharp \(1963\)](#) (D reported, closed circles). Solid curves represent model predictions assuming no positive correlation between grain size and excess shear velocity. Dashed curve represents model prediction assuming a linear correlation between grain size and excess shear velocity. (B) Data from [Wilson \(1972\)](#) (P_{20} reported, open circles) and [Lancaster \(1988\)](#) (P_{20} reported, all other symbols). In addition to grain size and shear velocity, predicted dune spacing is a sensitive function of maximum ripple slope, δ .

ripple spacing versus grain size from the Saharan Sand Seas ([Wilson, 1972](#)) and from Kelso Dunes, California ([Sharp, 1963](#)). Measurements of ripple spacing in wind tunnels (not plotted) are similar to the values measured by [Sharp \(1963\)](#), e.g. [Walker \(1981\)](#) measured ripples from 5–10 cm in spacing for median grain sizes of 0.2–0.8 mm. [Fig. 9A](#) plots the ripple spacing predicted by the model (i.e. $\lambda \approx 3000z_0$), using Eq. (15) with $C_m = 0.132$ (i.e. field conditions) to estimate z_0 as function of D or P_{20} and $u_* - u_{*t}$, for three excess shear velocity values: $u_* - u_{*t} \geq 0$, 0.1, and 0.2 m s^{-1} . For conditions just above the transport threshold, the model predicts ripple spacings very close to the values measured by [Sharp \(1963\)](#), e.g. $\lambda = 4–8 \text{ cm}$ for $D = 0.25–0.5 \text{ mm}$ and on the low end of the values reported by [Wilson \(1972\)](#). As the excess shear velocity increases, the predicted ripple spacing increases nonlinearly according to Eq. (15). The dependence of ripple spacing on excess shear velocity for a fixed grain size has been investigated by [Walker \(1981\)](#) and [Andreotti et al. \(2006\)](#). Both studies document a nonlinear increase in ripple spacing with excess shear velocity, as predicted by the model. It should be noted that the sensitive dependence of ripple spacing on excess shear velocity

predicted by the model and illustrated in Fig. 9A applies only to field conditions. In wind tunnels, the value of C_m is approximately an order of magnitude lower (Sherman and Farrell, 2008; but C_m will likely vary with the size of the wind tunnel), and hence the model predictions for ripple spacing in wind tunnels implies that larger excess shear velocities are required to achieve the same increase in ripple spacing compared to field conditions.

It should be noted that Eq. (15) is only one possible model of saltation induced roughness. Eq. (15) assumes that saltation induced roughness (i.e. the second term on the right side of Eq. (15)) is not an explicit function of grain size (i.e. except for the grain size dependence implicit in u_{*t}). For a given excess shear velocity, larger grains may exert more drag on the flow compared to smaller grains. In Sherman's (1992) analysis, he noted that a multivariate analysis of measured z_0 values versus both D and u_{*t} revealed that saltation induced roughness does, in fact, depend on grain size, but the data were inconclusive as to what particular form that dependence takes. One difficulty with determining the grain size dependence of saltation induced roughness is the relatively narrow range of grain sizes over which field and wind tunnel experiments have been performed. In Sherman's (1992) compilation, a large majority of measurements were collected for grain sizes between 0.2 and 0.4 mm, i.e. much smaller than the range of grain sizes studied by Wilson (1972).

Another complicating factor to consider is the potential correlation of grain size and excess shear velocity in the field. The model predictions plotted in Fig. 9A assume that grain size and shear velocity are independent variables. That is, each curve shows the trend in ripple spacing predicted by the model for different values of P_{20} or D assuming a uniform value of u_{*t} across the study area. In the field, however, it is possible that grain size and excess shear velocity are positively correlated. For example, areas characterized by higher average excess shear velocity conditions could transport a greater proportion of fine sand, leaving behind a locally coarse lag. As an illustration of the implications of such a correlation for ripple spacing, let's assume that grain size and excess shear velocity are linearly correlated in the field such that:

$$D = a(u_{*t} - u_{*t}) \quad (17)$$

where a is an empirical coefficient that varies from one dune field to the next but is constant within a given dune field. The dashed curve in Fig. 9A illustrates the ripple spacing predicted using Eq. (17) substituted into Eq. (15), with $a=0.00015$ s. The correlation represented by Eq. (17) is purely hypothetical, but it illustrates one hypothesis for the nonlinear grain size control documented in the Sahara by Wilson (1972). Similarly, if the saltation induced roughness is an increasing function of grain size, the model prediction for ripple spacing will also become a nonlinear function of grain size similar to the dashed curve in Fig. 9A. Although significant uncertainties exist in quantifying saltation induced roughness and potential correlations between grain size and excess shear velocity in the field, the model predicts values for ripple spacing that are similar to the range of values observed in the field and in wind tunnel experiments. In addition, the model reproduces the positive correlation between grain size, excess shear velocity, and ripple spacing observed in both field and wind tunnel measurements.

2.4. Application to transverse dunes

Once ripples form in areas with abundant sand supply, they become the dominant roughness elements on the surface, thus creating a larger effective roughness length. The scale independent nature of the bedform evolution model in this paper suggests that the creation of a new, larger, effective roughness length caused by ripple formation should trigger the same bedform instability that formed

ripples at a larger spatial scale. This conceptual model suggests a possible genetic linkage between ripples and dunes.

To apply this model to quantifying the spacing of dunes, it is necessary to estimate the effective aerodynamic roughness length of a rippled surface based on the roughness length of the initially flat surface and the ripple morphology. The oceanographic literature provides the necessary relationship to make this calculation (i.e. Jacobs, 1989). In the oceanographic case, wind generated water waves are the roughness elements analogous to ripples in the eolian case. Jacobs' (1989) analysis predicts that the effective aerodynamic roughness length, z_e , over sinusoidal topography is given by

$$\frac{z_e}{z_0} = \exp\left(\frac{1}{2} \left(\delta \ln\left(\frac{L}{z_0}\right)\right)^2\right) \quad (18)$$

where z_0 is the roughness length of the originally flat surface (calculated in Eq. (15)), L is the half length of the ripples at the half height position, and δ is the maximum slope of ripples. Eq. (18) is only accurate to approximately an order of magnitude, however, because ripples are not sinusoidal and the predictions of Eq. (18) are very sensitive to the maximum ripple slope, δ . Conceptually, the sensitivity of z_e/z_0 to δ is a consequence of the fact that, in the vicinity of the threshold slope for flow separation, small changes in the bed slope can result in large changes in the structure of boundary layer flow. Computational fluid dynamic (CFD) modeling of boundary layer flows over ripples of various shapes and sizes will be needed to more precisely quantify the value of z_e/z_0 for natural ripples. It should be emphasized that the "new" roughness length caused by ripple formation does not eliminate the roughness length of the initially flat surface. Rather, the velocity profile above a surface with two dominant scales of roughness is a composite velocity profile characterized by two roughness lengths, one that characterizes flow very close to the bed and one that characterizes flow at a larger spatial scale. It is the roughness length associated with this larger spatial scale that controls the flow convergence/expansion over dunes as they develop.

Fig. 9B plots measured spacings of transverse dunes from the Sahara Sand Seas (Wilson, 1972) and from the Skeleton Coast, Namib Sand Sea, and Gran Desierto (Lancaster, 1988). In focusing on these datasets I have intentionally left out dunes formed in areas of limited sand supply (i.e. barchan, star, and longitudinal dunes) for the reason that the aerodynamic roughness length over dunes formed in areas of limited sand supply will be controlled, in part, by the roughness elements of interdune or sand free areas rather than by grain size. Taken collectively, dune spacing in the Wilson and Lancaster datasets show a weak correlation with grain size. Within individual dune fields, however, the correlation is much stronger. The solid curves in Fig. 9B correspond to the model prediction for $u_{*t} \geq 0$, $L/z_0 = 750$ (i.e. assuming the model prediction for ripple spacing, i.e. $\lambda \approx 3000z_0$), and several values for the maximum ripple slope: $\delta = 0.53$ (i.e. the tangent of 28°), 0.58 (30°), and 0.63 (32°). Fig. 9B illustrate the extreme sensitivity of the model predictions to the maximum ripple slope, δ . Limited data exist for the maximum slope of ripples, but Sharp (1963) and Werner et al. (1986) put the range at between 25° and 30° . According to the model predictions, dunes formed with maximum ripple slopes of 28° have spacing values on the low side of measured values, while dunes formed with steep ripples (up to a maximum value of 33°) yield dunes with spacing values equivalent to the largest measured dunes. Although the model results are only illustrated for a single value of u_{*t} , the model predicts that dune spacing will increase with increasing u_{*t} in the same proportion as it does for ripple spacing in Fig. 9A. As such, an increase in excess shear velocity or maximum ripple slope results in larger dunes according to this model. The sensitivity of dune spacing to the maximum ripple slope provides one possible explanation for the variation in dune spacing between dune fields. Similarly, variations in shear velocity from one

dune field to another may also be responsible for variations in dune spacing between dune fields.

3. Discussion

The model of this paper clearly shows that ripples and dunes reach a steady state condition in which they migrate downwind without further growth. Using a broadly similar model of transverse dune formation (i.e. a mass conservative model of coupled boundary layer flow with erosion, deposition and avalanching), however, Schwammle and Herrmann (2004) concluded that bedform height and spacing increased proportionately to the square root of time indefinitely. This discrepancy is explained by the fact that Schwammle and Herrmann (2004) plotted their results over only one order of magnitude of time. Fig. 7 illustrates that the initial period of bedform growth takes place over two orders of magnitude in time prior to the attainment of steady state.

The model results of this paper provide a preliminary process based understanding of the grain size and wind velocity controls on the height and spacing of transverse eolian bedforms documented by Sharp (1963) and Walker (1981) for ripples, and Wilson (1972) and Lancaster (1988) for dunes in areas of abundant sand supply. The basis for this understanding is the numerical model prediction that the steady state height and spacing of transverse eolian bedforms scales with the aerodynamic roughness length. In the model, ripples form from a flat bed with a height and spacing that increase with increasing grain size and excess shear velocity, both of which control the aerodynamic roughness length z_0 via Sherman's relation (i.e. Eq. (15)). Once ripples form, they become the new dominant roughness element on the surface. The effective roughness length of the rippled surface triggers bedform creation at a larger scale, thus creating dunes. As a result, the spacing of dunes is also controlled by grain size and excess shear velocity in this model, because the effective roughness length of the rippled surface (i.e. Eq. (18)) is larger than the original roughness length of the flat surface by a constant scaling factor that depends on the detailed shape (i.e. maximum slope) of the ripples. It should be noted, however, that dune formation in nature and in the model does not require the existence of ripples. Instead, dunes can form on any surface with an aerodynamic roughness length similar to that of ripples, including gravel surfaces. For example, dunes are predicted to form in the model with a spacing of approximately 100 m if the aerodynamic roughness length is approximately 1/3000 of that value, i.e. 3 cm. Roughness lengths of this value are broadly consistent with roughness lengths of gravel surfaces without ripples.

Wilson (1972) argued that megadunes represent a distinctly different type of bedform from dunes, based on the fact that dunes and megadunes are distinct populations in his granulometric plot. Recent research, however, suggests that megadunes are composite bedforms that represent multiple periods of construction (e.g. Stokes and Bray, 2005; Bristow et al., 2007). The model of this paper, with its dependence on excess shear velocity, is broadly consistent with this composite bedform hypothesis for megadunes. Specifically, mega dunes with spacings of 1–3 km are predicted to form in the model under conditions of high average shear velocity (e.g. $u_* = u_{*c} = 0.25$ –0.4). Such conditions may have occurred over sufficiently long time periods during glacial climates for megadunes to form. According to this hypothesis, present conditions may be characterized by lower effective excess shear velocities. As a result, the dune forming instability may be concentrated at smaller spatial scales than those that were active when megadunes formed.

Although the numerical model of this paper represents the best compromise between computational speed and realistic boundary layer flow necessary to model ripples and dunes as they evolve over many time steps, it is important to emphasize that a complete numerical model for eolian bedforms will require a model that more accurately quantifies how steep slopes and flow separation impact the

entire boundary layer. In this paper, I incorporated the nonlinear effects of flow around steep topography by a local slope dependent correction term. This approach provides, I believe, the best compromise between computational speed and model realism given that more complex turbulence models are computationally far too intensive to be coupled to complex, evolving bed topography in 3D. A complete model for bedforms will also require a model that includes multiple grain sizes and the role of sorting on bedform morphology as bedforms develop.

Acknowledgements

This study was partially funded by the Army Research Office Terrestrial Sciences Program, grant W911NF 04 1 0266. I wish to thank Nick Lancaster and Gary Kocurek for critical reviews of an earlier draft of the manuscript that led to a significantly improved paper. I also wish to thank Takashi Oguchi for his careful editing of the manuscript.

References

- Anderson, R.S., 1987. A theoretical model for aeolian impact ripples. *Sedimentology* 34, 943–956.
- Anderson, R.S., Bunas, K.L., 1993. Grain size segregation and stratigraphy in aeolian ripples modelled with a cellular automaton. *Nature* 365, 740–743.
- Andreotti, B., Claudin, P., Pouliquen, O., 2006. Aeolian sand ripples: experiment study of fully developed states. *Physical Review Letters* 96 (L028001). doi:10.1103/PhysRevLett.96.028001.
- Ayotte, K.W., 2008. Computational modeling for wind energy assessment. *Journal of Wind Engineering and Industrial Aerodynamics* 96 (10–11), 1571–1590.
- Ayotte, K.W., Hughes, D.E., 2004. Observations of boundary-layer wind-tunnel flow over isolated ridges of varying steepness and roughness. *Boundary Layer Meteorology* 112, 525–556.
- Baas, A.C.W., 2007. Complex systems in aeolian geomorphology. *Geomorphology* 91, 311–331.
- Bagnold, R.A., 1936. The movement of desert sand. *Proceedings of the Royal Society of London Series A* 157, 594–620.
- Bagnold, R.A., 1941. *The Physics of Blown Sand and Desert Dunes*. Methuen & Co., London, United Kingdom.
- Bristow, C.S., Duller, G.A.T., Lancaster, N., 2007. Age and dynamics of linear dunes in the Namib Desert. *Geology* 35, 555–558.
- Elberhiti, H., Andreotti, B., Claudin, P., 2008. Barchan dune corridors: field characterization and investigation of control parameters. *Journal of Geophysical Research, Earth Surface* 113 (F02S15). doi:10.1029/2007JF000767.
- Folk, R.L., 1976. Rollers and ripples in sand, streams, and sky: rhythmic alteration of transverse and longitudinal vortices in three orders. *Sedimentology* 23, 649–669.
- Hanna, S.R., 1969. The formation of longitudinal sand dunes by large helical eddies in the atmosphere. *Journal of Applied Meteorology* 8, 874–883.
- Hardisty, J., Whitehouse, K.J.S., 1988. Evidence for a new sand transport process from experiments on Saharan dunes. *Nature* 332, 532–534.
- Howard, A.D., 1977. Effect of slope on the threshold of motion and its application to orientation of wind ripples. *Geological Society of America Bulletin* 88, 853–856.
- Howard, A.D., Morton, J.B., Gad-El-Hak, M., Pierce, D.B., 1989. Sand transport model of barchan dune equilibrium. *Sedimentology* 25, 307–338.
- Iversen, J.D., Rasmussen, K.R., 1999. The effect of wind speed and bed slope on sand transport. *Sedimentology* 46, 723–731.
- Jacobs, S.J., 1989. Effective roughness length for turbulent flow over a wavy surface. *Journal of Physical Oceanography* 19, 998–1010.
- Jackson, P.S., Hunt, J.C.R., 1975. Turbulent wind flow over a low hill. *Quarterly Journal of the Royal Meteorological Society* 101, 929–955.
- Lancaster, N., 1988. The development of large aeolian bedforms. *Sedimentary Geology* 55, 69–89.
- Lancaster, N., 1996. The role of field experiments in studies of dune dynamics and morphology. *Annals of Arid Zone* 35, 171–186.
- Mason, P.J., Sykes, R.I., 1979. Flow over an isolated hill of moderate slope. *Quarterly Journal of the Royal Meteorological Society* 105, 383–395.
- Mitha, S., Tran, M.Q., Werner, B.T., Haff, P.K., 1986. The grain-bed impact process in eolian saltation. *Acta Mechanica* 63, 267–278.
- Momiji, H., Carretero-Gonzalez, R., Bishop, S.R., Warren, A.W., 2000. Simulation of the effect of wind speedup in the formation of transverse dune fields. *Earth Surface Processes and Landforms* 25, 905–918.
- Ould Ahmedou, D., Ould Mahfoudh, A., Dupont, P., Ould El Mactar, A., Valance, A., Rasmussen, K.R., 2007. Barchan dune mobility in Mauritania related to dune and interdune sand fluxes. *Journal of Geophysical Research, Earth Surface* 112 (F02106). doi:10.1029/2006JF000500.
- Schwammle, V., Herrmann, H.J., 2004. Modelling transverse dunes. *Earth Surface Processes and Landforms* 29, 769–784.
- Seppala, M., Linde, K., 1978. Wind tunnel studies of ripple formation. *Geografiska Annaler* 60, 29–42.
- Sharp, R.P., 1963. Wind ripples. *Journal of Geology* 71, 617–636.

- Sherman, D.J., 1992. An equilibrium relationship for shear velocity and apparent roughness length in aeolian saltation. *Geomorphology* 5, 419–431.
- Sherman, D.J., Farrell, E.J., 2008. Aerodynamic roughness length over movable beds: comparison of wind tunnel and field data. *Journal of Geophysical Research* 113 (F02S08). doi:10.1029/2007JF000784.
- Stam, J.M.T., 1996. Migration and growth of aeolian bedforms. *Mathematical Geology* 28, 519–536.
- Stam, J.M.T., 1997. On the modeling of two-dimensional aeolian dunes. *Sedimentology* 44, 127–141.
- Stokes, S., Bray, H.E., 2005. Late Pleistocene eolian history of the Liwa region, Arabian Peninsula. *Geological Society of America Bulletin* 117, 1466–1480.
- Van Dijk, P.M., Arens, S.M., Van Boxel, J.H., 1999. Aeolian processes across transverse dunes. II. Modeling the sediment transport and profile development. *Earth Surface Processes and Landforms* 24, 319–333.
- Walker, J.D., 1981. An experimental study of wind ripples. M.S. Thesis, Massachusetts Institute of Technology, Cambridge, MA, 145 pp.
- Wasson, R.J., Hyde, R., 1983. A test of the granulometric control of desert dune geometry. *Earth Surface Processes and Landforms* 8, 301–312.
- Weng, W.S., Hunt, J.C.R., Carruthers, D.J., Warren, A., Wiggs, G.F.S., Livingstone, I., Castro, I., 1991. Air flow and sand transport over sand-dunes. *Acta Mechanica* 2, 1–22.
- Werner, B.T., 1995. Eolian dunes: computer simulations and attractor interpretation. *Geology* 23, 1107–1110.
- Werner, B.T., Gillespie, D.T., 1993. Fundamentally discrete stochastic model for wind ripple dynamics. *Physical Review Letters* 71, 3230–3233.
- Werner, B.T., Kocurek, G., 1997. Bed-form dynamics: does the tail wag the dog? *Geology* 25, 771–774.
- Werner, B.T., Kocurek, G., 1999. Bedform spacing from defect dynamics. *Geology* 27, 727–730.
- Werner, B.T., Haff, P.K., Livi, R.P., Anderson, R.S., 1986. Measurement of eolian sand ripple cross-sectional shapes. *Geology* 14, 743–745.
- Willetts, B.B., Rice, M.A., 1988. Effect of bedslope on desert sand transport. *Nature* 334, 302.
- Wilson, I.G., 1972. Aeolian bedforms: their development and origins. *Sedimentology* 19, 173–210.
- Wippermann, F., Gross, G., 1986. The wind-induced shaping and migration of an isolated dune: a numerical experiment. *Boundary Layer Meteorology* 36, 319–334.
- Wood, N., Mason, P., 1993. The pressure force induced by neutral, turbulent flow over low hills. *Quarterly Journal of the Royal Meteorological Society* 119, 1233–1267.
- Xu, D., Ayotte, K.W., Taylor, P.A., 1994. Development of a non-linear mixed spectral finite difference model for turbulent boundary layer flow over topography. *Boundary-Layer Meteorology* 70, 341–367.

The effects of interdune vegetation changes on eolian dune field evolution: a numerical-modeling case study at Jockey's Ridge, North Carolina, USA

Jon D. Pelletier,^{1*} Helena Mitsova,² Russell S. Harmon² and Margery Overton³

¹ Department of Geosciences, University of Arizona, Tucson, Arizona, USA

² Department of Marine, Earth, and Atmospheric Sciences, North Carolina State University, Raleigh, North Carolina, USA

³ Department of Civil, Construction, and Environmental Engineering, North Carolina State University, Raleigh, North Carolina, USA

Received 9 September 2008; Revised 22 January 2009; Accepted 9 February 2009

* Correspondence to: Jon D. Pelletier, Department of Geosciences, University of Arizona, 1040 East Fourth Street, Tucson, AZ 85721, USA.

E-mail: jdpellet@email.arizona.edu

ESPL

Earth Surface Processes and Landforms

ABSTRACT: Changes in vegetation cover within dune fields can play a major role in how dune fields evolve. To better understand the linkage between dune field evolution and interdune vegetation changes, we modified Werner's (*Geology*, 23, 1995: 1107–1110) dune field evolution model to account for the stabilizing effects of vegetation. Model results indicate that changes in the density of interdune vegetation strongly influence subsequent trends in the height and area of eolian dunes. We applied the model to interpreting the recent evolution of Jockey's Ridge, North Carolina, where repeat LiDAR surveys and historical aerial photographs and maps provide an unusually detailed record of recent dune field evolution. In the absence of interdune vegetation, the model predicts that dunes at Jockey's Ridge evolve towards taller, more closely-spaced, barchanoid dunes, with smaller dunes generally migrating faster than larger dunes. Conversely, the establishment of interdune vegetation causes dunes to evolve towards shorter, more widely-spaced, parabolic forms. These results provide a basis for understanding the increase in dune height at Jockey's Ridge during the early part of the twentieth century, when interdune vegetation was sparse, followed by the decrease in dune height and establishment of parabolic forms from 1953-present when interdune vegetation density increased. These results provide a conceptual model that may be applicable at other sites with increasing interdune vegetation cover, and they illustrate the power of using numerical modeling to model decadal variations in eolian dune field evolution. We also describe model results designed to test the relative efficacy of alternative strategies for mitigating dune migration and deflation. Installing sand-trapping fences and/or promoting vegetation growth on the stoss sides of dunes are found to be the most effective strategies for limiting dune advance, but these strategies must be weighed against the desire of many park visitors to maintain the natural state of the dunes. Copyright © 2009 John Wiley & Sons, Ltd.

KEYWORDS: eolian dunes; numerical modeling; biogeomorphology

Introduction

The evolution of many eolian dunes is strongly controlled by vegetation. Vegetation increases the aerodynamic roughness length of the surface, stabilizing the vegetation-covered portions of dunes (Sarre, 1989; Lancaster and Baas, 1998; Hugenholtz *et al.*, 2008). Conceptual models linking dune-field activity to climate change tend to treat dune fields as either wholly 'active' or 'inactive' depending on the threshold vegetation density (e.g. Hugenholtz and Wolfe, 2005). In detail, however, the evolution of partially-vegetated dune fields depends critically on the spatial distribution of vegetation within the dune field. Baas and Nield (2007), for example, explored the co-evolution of dune morphology and vegetation for partially-vegetated dunes using a numerical model. In this model, vegetation

growth is favored on the trailing arms of incipient dunes where the magnitude of erosion and deposition falls within a certain range conducive to vegetation growth. Vegetation growth, in turn, limits erosion and deposition on trailing arms. In this way, vegetation cover, rates of erosion and deposition, and dune morphology co-evolve under certain conditions to create parabolic dunes that migrate at a steady rate. Duran and Herrmann (2006) also developed a model that couples eolian transport and erosion/deposition with the growth and death of plants. Their model was capable of quantifying the transition from active to inactive dunes as a function of vegetation density.

The response of active dune fields to changes in vegetation density through time is less well understood, however. In the US, the Outer Banks of North Carolina has been a particularly

well studied area, but many questions remain. Dune mobilization due to loss of vegetation in the Outer Banks during the nineteenth century resulted in development of rapidly moving, destructive barchan dunes or médanos in many areas (Cobb, 1906). Some of these dunes were artificially stabilized, e.g. to construct the Wright Brothers Memorial. Unfortunately, the limited quality of early aerial photographs (1932 and 1949) does not allow clear identification of the barchans mentioned in the literature, although some can be inferred from aerial photographs acquired in 1949 (Mitasova *et al.*, 2005). After construction of protective dunes in the 1930s (Birkemeier *et al.*, 1984), interdune vegetation in the Outer Banks increased from sparse to dense over the following 50 years. Outside of the US, dune stabilization due to vegetation 'invasion' has been reported at other locations such as the Tottori sand dunes in Japan (Onishi, 2006) as well as dunes near Cresmina, Portugal (Rebello *et al.*, 2002). The goal of this paper is to better understand the cause-and-effect relationship between the density of interdune vegetation and dune field evolution.

Jockey's Ridge, North Carolina is the largest active dune complex on the east coast of the US and provides a suitable test case for our investigation. The recent evolution of this dune field is unusually well constrained following the work of Mitasova *et al.* (2005). These authors used airborne LiDAR surveys to map the dune field evolution at high spatial resolution (1.8 m/pixel) in 1999 and 2001. Historical aerial photographs and topographic maps enabled changes in dune height and vegetation cover to be constrained over the past century. Changes in dune area were quantified from 1974 to 2001. Jockey's Ridge is comprised of four major dunes, labeled (clockwise from left in Figure 1) west, main, east, and south dunes. Recent long-term net sand transport at Jockey's Ridge is approximately due south (Havholm *et al.*, 2004), leading to predominantly south-directed dune migration at relatively

steady rates of 3–6 m/yr. While the net sand-transport direction is to the south, southerly (i.e. north-directed) winds do occur, resulting in slipface reversals and episodic north-directed dune migration for short periods of time. Also, despite the southward net transport direction, the slip faces of the major dunes have migrated in complex ways (i.e. the white arrows in Figure 1), reflecting the possible impact of hurricanes with strong, rotating wind fields.

Mitasova *et al.* (2005) inferred a rapid increase in height of the main dune between 1915 and 1953 from approximately 20 to 40 m, followed by gradual decrease back to nearly 20 m from 1953 to the present. The recent dune deflation was accompanied by decrease in windward slope of the main dune from 5° to 2.5° between 1974 and 2005 and an increase in the area of the dune field by approximately 15% during that time period. Figure 2 illustrates the change in dune field morphology from 1974 to 1999. The results of recent surveys, up to and including 2008, show a continuation of this trend of decreasing dune height. Figure 2(A) illustrates the digital elevation model (DEM) of Jockey's Ridge in 1974, as constructed from historical topographic contour maps. The color map of change between 1974 (Figure 2A) and 1999 (Figure 1) illustrated in Figure 2(B) indicates the predominantly southward migration of dunes and the loss of peak elevation between 1974 and 1999. The transition from increasing to decreasing height of the main dune in the early 1950s coincided with an increase in interdune vegetation density documented in historical aerial photographs (Mitasova *et al.*, 2005). The establishment of dense interdune vegetation has been attributed to the construction of a linear foredune along the Outer Banks beaches in the 1930s (Birkemeier *et al.*, 1984). However, Havholm *et al.* (2004) argued that climate change is a major driver of dune evolution at Jockey's Ridge. The geological surveys conducted by Havholm *et al.* (2004) discovered two layers of soil within the dune indicating that the area changed from active dune to forest twice over the past 1000 years.

Dune migration has posed a persistent threat to the infrastructure in the vicinity of Jockey's Ridge in recent years, particularly along Soundside Road (Figure 1). In response, park managers have used sand redistribution and fencing to mitigate the southward migration and deflation of the dune field. Sand fencing installed at the south dune has slowed dune migration and triggered growth in the height of this dune but it did not stop the dune from exiting the park (Mitasova *et al.*, 2005). Approximately 125 000 m³ of sand was removed from the south dune and deposited along the northern edge of the park in the winter of 2003. Both of these techniques have been somewhat effective in limiting the amount of sand exiting the park, but questions remain as to how to manage the larger dunes to preserve the natural landforms while minimizing the export of sand from the park. For example, where should sand be relocated and where should fences be installed in order for these strategies to be the most effective? Are there other mitigation strategies that could be more useful? In this paper, we use numerical modeling to test the efficacy of alternative mitigation strategies in order to provide guidance to land managers at Jockey's Ridge and in similar areas where rapidly-migrating dunes threaten infrastructure. More broadly, our goal in this paper is to use numerical modeling to explore the relationships between dune evolution and the spatial distribution of vegetation using Jockey's Ridge as a type of example. The purpose of the modeling is not to reproduce the exact details of the recent evolution of Jockey's Ridge, but instead to gain a better conceptual and quantitative understanding of how dune fields respond to changes in the spatial distribution of vegetation and management intervention.

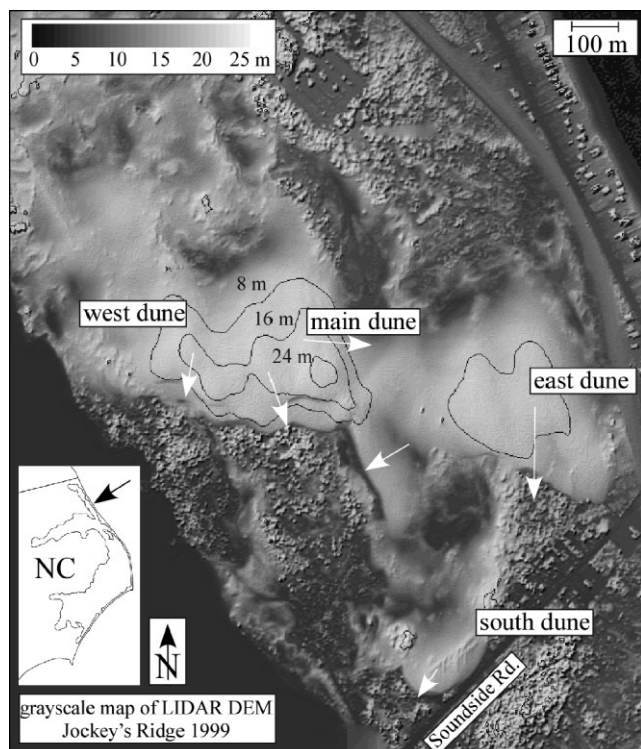


Figure 1. Grayscale map of elevations at Jockey's Ridge, North Carolina, in 1999, as determined from an airborne LiDAR survey. White arrows indicate direction and relative magnitude of recent (1974–2001) dune migration.

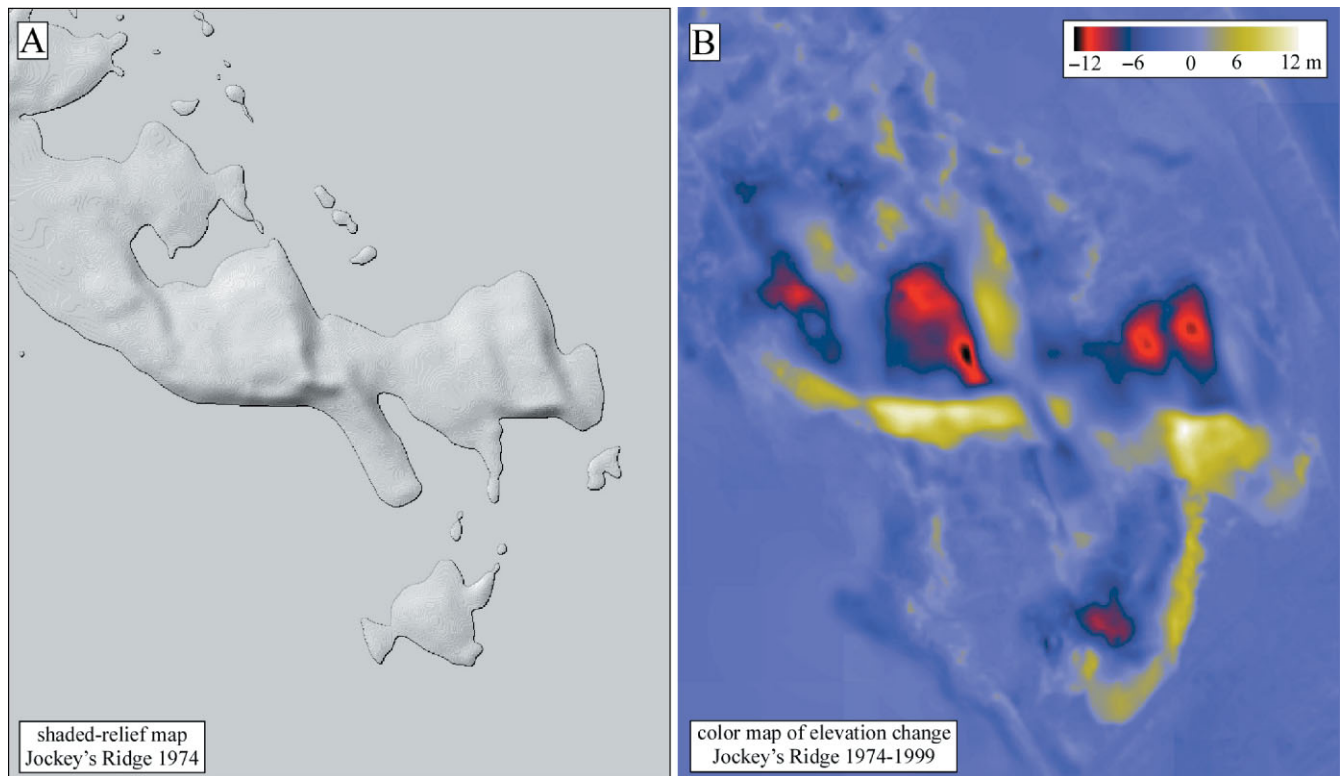


Figure 2. Maps illustrating change in Jockey's Ridge dune field from 1974 to 1999. (A) Grayscale map of Jockey's Ridge elevations in 1974 as determined from historical contour maps (Mitasova *et al.*, 2005). (B) Color map of change in elevations from 1974 to 1999. Areas of denudation appear in black and red, while areas of aggradation appear as yellow and white. This figure is available in colour online at www.interscience.wiley.com/journal/espl

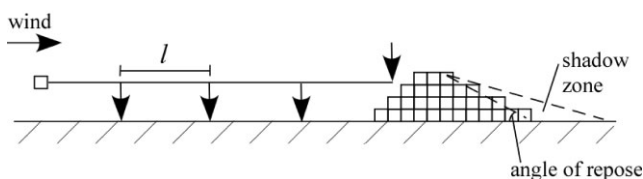


Figure 3. Schematic diagram of Werner's (1995) model of eolian dune evolution.

Model Description

The model we developed is a modified version of the dune field evolution model of Werner (1995). Werner (1995) was the first to model the formation of eolian dunes numerically from an initially flat surface. Werner's (1995) model (Figure 3) is based on the iterative entrainment, transport, and deposition of discrete units of sand that are picked up at random, transported a characteristic distance l downwind, and deposited back onto the surface with a probability p_s that is, by default, equal to 0.5. Sand units that are not deposited after the first 'jump' of distance l are transported repeatedly downwind until deposition occurs. In this way, the local sand flux depends on the values of l and p_s input into the model. In Werner's model, the effect of air flow over incipient dunes is included in a simplified way by defining 'shadow' zones where the probability of deposition is one. Shadow zones are defined to be areas located in shadow when the surface is illuminated by a sun angle of 15° from the horizontal and parallel to the wind direction. In Werner's model, shadow zones provide a simplified representation of the recirculation zone on the lee sides of incipient dunes where wind-driven sediment flux is low and deposition rates are high. Sand units deposited back

down on the bed in Werner's model roll down the direction of steepest descent if deposition causes an oversteepened condition (i.e. a slope angle greater than the angle of repose). Werner's model combines three basic elements that, taken together, are responsible for the complex self-organized behavior observed in the model. First, the stochastic model of entrainment generates structureless, multi-scale relief from an initially flat bed. Second, shadow zones provide a mechanism for a positive feedback between the topography of incipient dunes and the spatial pattern of erosion and deposition that enhances dune height and spacing over time. Finally, avalanching provides a limitation on dune slope and a mechanism for cross-wind sand transport. Werner's model is capable of reproducing the four principal dune types (transverse, barchan, star, and linear) by varying sand supply and wind direction variability.

Werner's model forms the basis for a recent numerical model that explores the co-evolution between dunes and vegetation (Baas and Nields, 2007; Baas, 2007). In the Baas and Nields' model, empirical curves are used to relate vegetation growth and decay to the local rate of erosion and deposition. Vegetation density, in turn, influences the probability of deposition, p_s , in the model. In this paper, we take an alternative approach. First, we introduce a probability of entrainment, p_e , that varies according to the local vegetation density. Second, rather than modeling vegetation growth and decay explicitly through time, vegetation density and its effect on sediment flux is included using a prescribed relationship between the probability of entrainment, p_e , and elevation above that of the lowest interdune areas. In the Werner (1995) model, sand units are entrained from the surface with an equal probability at each pixel. In the model of this paper, the probability of entrainment, p_e , varies spatially depending on the local elevation, which is used as a proxy for vegetation density. In the model, a sand unit chosen at random from all the pixels in the model is

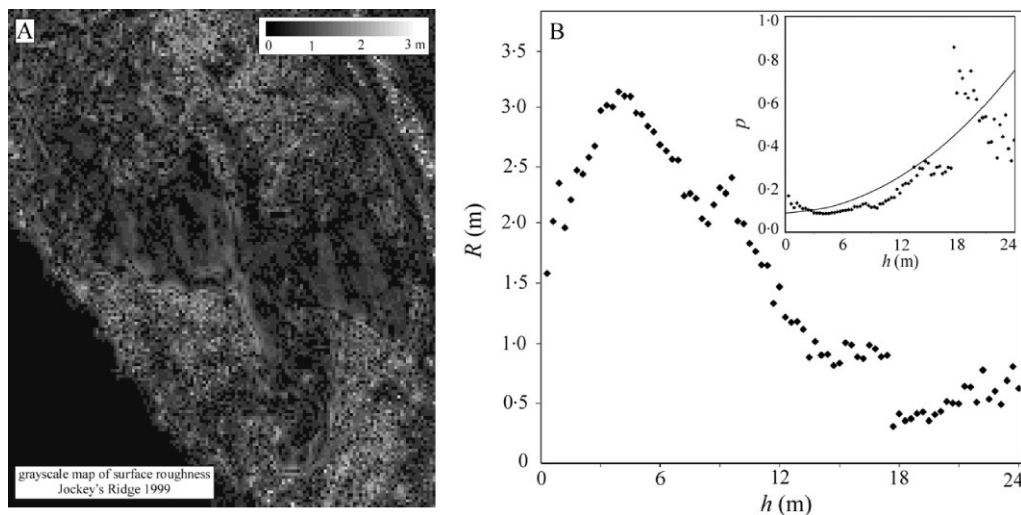


Figure 4. (A) Grayscale map of surface roughness of Jockey's Ridge in 1999, illustrating the relatively smooth dune surfaces in comparison to the rough interdune areas. (B) Plot of average surface roughness as a function of elevation. Areas of higher surface roughness (i.e. vegetation cover will have lower rates of particle entrainment. In the model, the probability of entrainment is assumed to be inversely proportional to roughness (inset). The solid curve in the inset graph illustrates the quadratic relationship between entrainment probability and elevation used in the model.

entrained if a random variable between zero and one is less than the local, elevation-dependent value of p_e , which also varies between zero and one. Otherwise, nothing happens during that time step. This elevation-dependent entrainment rule is calibrated specifically for the Jockey's Ridge site (calibration described later) using the relationship between surface roughness and elevation before and after the establishment of interdune vegetation beginning in the early 1950s. Prior to the early 1950s, the vegetation density at Jockey's Ridge was negligible (Mitasova *et al.*, 2005). As such, the original Werner (1995) model can be used to model dune evolution during this time period. After the early 1950s, the development of interdune vegetation stabilized low elevations but did not significantly affect sediment entrainment at higher elevations where vegetation density is negligible. For the post-1950s period, therefore, it is appropriate to vary p_e spatially according to elevation in order to represent the stabilizing effects of vegetation at low elevations.

In order to constrain the relationship between entrainment probability and elevation in the post-1950s era at Jockey's Ridge, consider Figure 4. Figure 4(A) illustrates a map of the surface roughness of Jockey's Ridge in 1999 computed from the 1.8 m/pixel resolution digital surface model (DSM) derived from the first return LiDAR data that include top of vegetation. This map represents the absolute value of the difference between the maximum and minimum elevations within a prescribed distance from each pixel, given here by 7.3 m or four pixels. In other words, Figure 4(A) plots the relief of the topography (including vegetation, man-made infrastructure, and all other roughness elements resolved in the DSM) at spatial scales of 7.3 m. In this paper we use the term surface roughness to describe the small-scale terrain relief measured in this way. This should not be confused with the aerodynamic roughness length. Figure 4(B) plots the relationship between the surface roughness mapped in Figure 4(A) and elevation above sea level, illustrating the inverse relationship between these two variables. In areas devoid of vegetation and other roughness elements, namely the areas with dunes that make up the high-elevation portions of the landscape, surface roughness values are typically between 0 and 1 m. Conversely, low-elevation zones (e.g. elevations between 0 and 6 m) are characterized by surface roughness values typically between 2 and 3 m.

Sediment flux is inversely correlated with the local surface roughness: areas of higher local-scale relief (e.g. taller and denser vegetation) will have correspondingly lower eolian sediment fluxes due to the sheltering effect of those roughness elements. The relationship between surface roughness and sediment flux is complex. In the model of this paper we assume a simple inverse proportionality between these two variables. The inset plot in Figure 4(B) plots the inverse of surface roughness as a function of elevation. The continuous solid curve in the inset graph is a parabolic fit to the data. This plot suggests that the probability of entrainment, p_e , can be modeled using a parabolic function of elevation, h , during the post-1950s era at Jockey's Ridge:

$$p_e \propto h^2. \quad (1)$$

More generally, one can assume that the relationship between p_e and h is a power-law relationship with exponent b : $p_e \propto h^b$. This power-law relationship is useful for understanding the transition between the different types of behavior exhibited by the model as the exponent b is varied continuously from zero (i.e. Werner's model) to two (Equation 1). In the model, the maximum probability is set to one for a reference elevation close to the highest elevation value in the model, i.e.

$$p_e = \left(\frac{h}{30 \text{ m}} \right)^2. \quad (2)$$

In Equation 2, the probability of entrainment is nearly zero for elevations close to zero and rises quadratically with elevation to a maximum value of one at an elevation of 30 m (i.e. close to the maximum elevation of the model at any time during the model runs presented in this paper).

In addition to the entrainment-elevation relationship represented by Equation 2, we also introduced an east-west gradient in entrainment probability into the model. The motivation for this model component is the mobility of the east dune, which in recent years has been (along with the south dune) the most active dune in the dune field. The east dune is the most susceptible to high bed shear stresses due to its proximity to the ocean. Dunes further inland experience lower shear stresses for the same far-field wind speeds due to the greater surface roughness (i.e. vegetation, infrastructure,

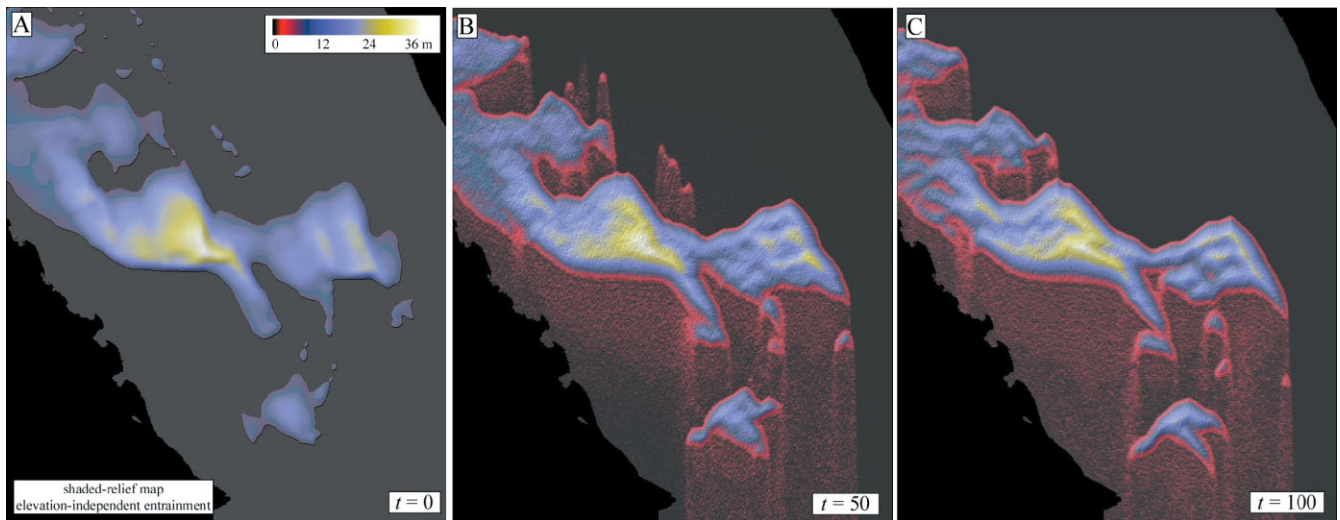


Figure 5. Color maps of dune evolution in the reference model with no vegetation (i.e. spatially uniform entrainment) for (A) $t = 0$ (Jockey's Ridge in 1974), (B) $t = 50$, (C) and $t = 100$. Units of time in the model are arbitrary but can be calibrated using measured and modeled dune migration rates. This figure is available in colour online at www.interscience.wiley.com/journal/espl

etc.) upwind from those dunes. In the model, we prescribed a higher entrainment probability on the east side of the study area using the relationship

$$p_e = \left(\frac{h}{30 \text{ m}} \right)^2 \left(\frac{x}{1200 \text{ m}} \right). \quad (3)$$

where x is the distance from the western boundary of the model. Equation 3 increases the entrainment probability from zero (along the western boundary of the model) to a maximum value close to one (along the eastern boundary of the model) as a linearly-increasing function of x .

Model Results

Figure 5 illustrates the results of the Werner (1995) model applied to Jockey's Ridge using the 1974 DEM of Jockey's Ridge constructed by Mitasova *et al.* (2005) as the initial condition for this model run. How the dune field evolves from this state provides insight into the potential trends in dune field evolution if all surrounding vegetation was removed and the initial dune was surrounded by a flat sheet of sand. In the model, areas that had no significant sand cover in 1974 were made equal to 0.3 m in the model. The model was run with input parameters $l = 9 \text{ m}$ (5 pixels) and $p_s = 0.5$. The values of l and p_s influence the average rate of dune migration and the wavelength of instabilities produced by the model, but otherwise the values of l and p_s do not influence the trends in dune modification with or without interdune vegetation documented in this paper. Time in the model is arbitrary (and depends on the values of l and p_s), but the model can be calibrated to real time by comparing measured and modeled migration rates for a given study site over a given interval of time. The units of time are normalized to the number of grid points, so $t = 1$ refers to the time at which transport has been attempted, on average, once in each of the pixels in the model. No sand entered the model domain from the northern boundary but sand was allowed to leave from the bottom boundary. Sand that was transported into the ocean or sound from within the model domain was also removed from the system. Sand transport in the model takes place in a due south direction, reflecting the northerly winds that contribute the most to sand transport according to Havholm *et al.* (2004).

The effects of variable substrate erodibility (e.g. soil horizons), changes in moisture (precipitation/evaporation) over time, and changes in the water table elevation over time were not considered in the model.

Over time, the model illustrated in Figure 5 develops more closely-spaced, barchanoid dunes that grow in height and decrease in total area, similar to those described for example by Cobb (1906). Over the example period illustrated in Figure 5, the main dune grows from 30 to 36 m and the total area of the dune field decreases from $4.36 \times 10^5 \text{ m}^2$ to $4.21 \times 10^5 \text{ m}^2$. The model also predicts that smaller dunes migrate somewhat faster than larger dunes (best illustrated in the change map of Figure 7A), but the east dune migrates the fastest due to the east–west gradient in flux imposed by Equation 3. The inverse correlation between dune height and migration rate in this model scenario (i.e. small dunes migrate faster than large dunes) is consistent with Bagnold's hypothesis that dune migration rate is inversely proportional to dune height assuming that sand transport rates are independent of dune height (Bagnold, 1941). Taller desert dunes are often observed to migrate at rates proportionately slower than shorter dunes because dune migration requires that the entire cross-section of the dune (which is proportional to height) be transported along the surface. Therefore, taller dunes will migrate more slowly than shorter dunes if sand transport rates are independent of dune height. The results illustrated in Figure 5 were obtained assuming no sand flux input from upwind of the study area. Introducing a constant influx of sediment along the upwind boundary has the effect of decreasing dune migration rates slightly, but the dune elevation does not change and the model results do not otherwise depend on the choice of boundary conditions.

Figure 6 illustrates the results of the model with elevation-dependent entrainment (i.e. Equation 3). Over time, this model develops paraboloidal dunes that decrease in height (the main dune decreases from 30 to 24 m) and increase in total area (from $4.36 \times 10^5 \text{ m}^2$ to $4.51 \times 10^5 \text{ m}^2$). Also, large dunes in this model migrate at rates comparable to that of smaller dunes (Figure 7B). This tendency can be understood as a result of the relationship between entrainment probability and elevation. In this model, sand transport rates over smaller dunes are lower than those over larger dunes because of the positive relationship between p_e and elevation. In the absence of this effect, small dunes migrate faster as described earlier. The lower sand transport rates of smaller dunes in this

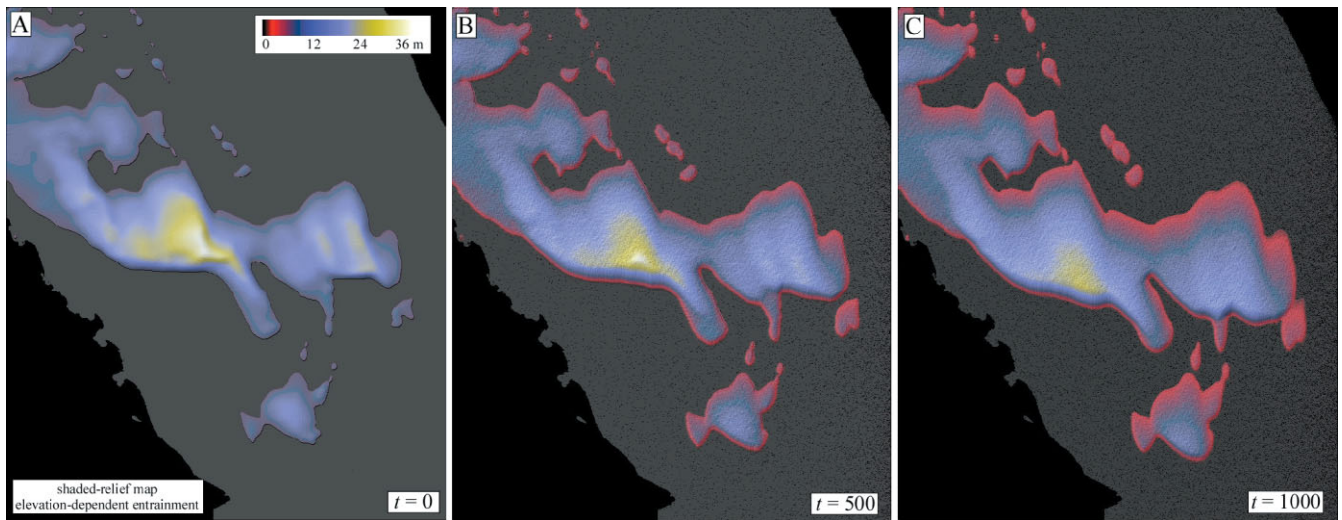


Figure 6. Color maps of dune evolution in the revised model with interdune vegetation (i.e. elevation-dependent entrainment) for (A) $t = 0$ (Jockey's Ridge in 1974), (B) $t = 500$, (C) and $t = 1000$. This figure is available in colour online at www.interscience.wiley.com/journal/esp

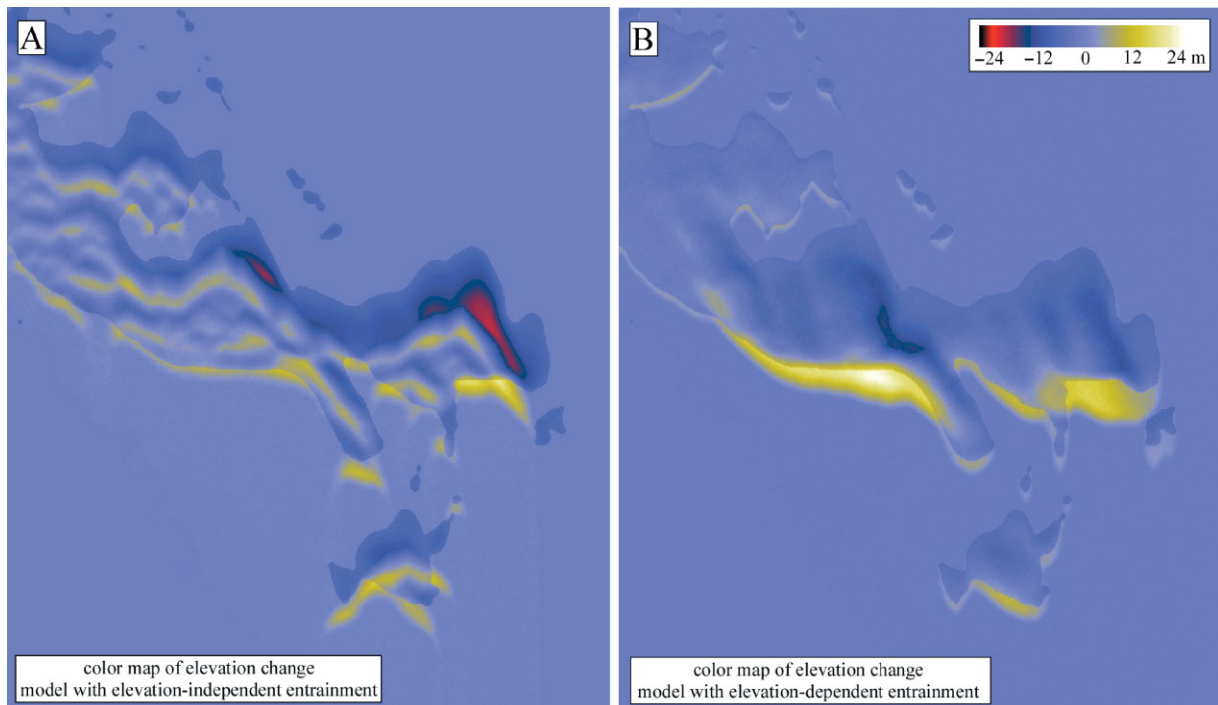


Figure 7. Color maps of elevation change between the beginning and end of the models illustrated in (A) Figure 5 and (B) Figure 6, highlighting the spatial distribution of erosion/deposition and dune migration. This figure is available in colour online at www.interscience.wiley.com/journal/esp

vegetation-controlled system offsets the geometric effect that causes large dunes to migrate more slowly in areas with sparse or no vegetation cover, thereby causing large dunes to migrate at rates similar to small dunes. Note that in Figure 5 (no vegetation), dune migration of approximately 100 m requires only a fraction of the time (i.e. $t = 100$ versus $t = 1000$) required in the model of Figure 6. The lower average rate of dune migration in Figure 6 reflects the stabilizing effects of vegetation (i.e. the overall lower probability of entrainment) in this model relative to that of Figure 5.

Figures 5 and 6 suggest that dune field evolution in the presence of interdune vegetation cover can be characterized by two alternative states. In the absence of interdune vegetation, dune fields develop taller, barchanoid-shaped dunes with small dunes migrating faster than larger dunes (although the east-west gradient in transport adds additional complexity to the

relationship between dune size and migration rate in this case). In the presence of interdune vegetation, dune fields evolve towards shorter, paraboloidal dunes with large dunes migrating at rates comparable to those of smaller dunes. The transition between these two end-member states can be investigated within the model framework by using the power-law relationship between p_e and h (i.e. $p_e \propto h^b$) with different values of b . Model results with this generalized entrainment-elevation relationship (not shown) illustrate that the transition between these two end-member states occurs at $b = 1$. Dunes grow in height and develop barchanoid dunes for all values of b less than one and decrease in height and develop paraboloidal dunes for all values of b greater than one. Therefore, the essential criterion for determining dune morphology and evolution is not the presence or absence of interdune vegetation, but rather the functional form of the relationship between vegetation

density and elevation. If sediment flux decreases rapidly with elevation (if, for example, a 50% increase in elevation results in a 90% decrease in sediment flux), then the system will be in the $b > 1$, deflating-dune regime. In contrast, if sediment flux decreases more slowly with increasing elevation (e.g. a 50% increase in elevation results in a 30% decrease in sediment flux), then the system will be in the $b < 1$, growing-dune regime.

Approximately 125 000 m³ of sand was removed from the leading (southern) edge of the Jockey's Ridge dune field and deposited at its northern edge in the year 2003. This redistribution of sand, in and of itself, is a useful strategy for protecting the nearby infrastructure from dune encroachment. Indeed, given the volume and migration rate of the dune field, it is possible to estimate the mean annual volume of sand that must be redistributed in order to balance the action of the wind. Given the current dune-field volume of approximately 3×10^6 m³ (Mitasova *et al.*, 2005), a migration rate of 5 m/yr, and a transported distance of 1000 m, and northerly prevailing winds, it would be necessary to relocate approximately 15 000 m³ of sand each year in order to achieve a long-term balance between anthropogenic transport to the north and natural eolian transport to the south. Ideally, however, the sand would be relocated in such a way as to minimize the subsequent dune migration and encourage the development of taller dunes.

Figure 8 illustrates the results of numerical experiments aimed at quantifying the effect of sand redistribution on subsequent dune advancement and growth/deflation. We modeled the anthropogenic transport of sand by removing 6 m of sand from all pixels where the slope angle exceeded 20° (i.e. dune slip faces, labeled as 'sources' in Figure 8A). This hypothetical source distribution is not meant to represent the actual redistribution of sand that has occurred at Jockey's Ridge. In fact, redistributed sand has been sourced from the south dune only. Nevertheless, slip faces provide one possible source region for sand redistribution generally, as slip faces are the leading edge of dunes and hence the sand that most immediately threatens infrastructure. Removing a fixed thickness of sand from all slip faces and redistributing that sand upwind represents one possible strategy for mitigating dune field advance. Sand removed from slip faces in the model was deposited north of the crestline of the main dune complex by a fixed 'relocation

distance' (360 m in the example of Figure 8A). Figure 8B plots the subsequent relative migration rates of the dune field as a whole as a function of the relocation distance. Sand that was relocated onto the dune crestline (i.e. equal to a 'relocation distance' of zero from the crestline) had the greatest impact on subsequent migration rates in the model, causing a decrease of approximately 6.5%. Sand that was relocated at progressively greater distances from the crestline had a correspondingly lower effect on subsequent migration rates. Sand redistribution had no significant effect on dune height: maximum dune height with and without sand redistribution and for different distances of sand redistribution differed by less than 0.5 m in simulations of the dune-field evolution following sand redistribution. Over all, these results indicate that sand redistribution has only a marginal effect on subsequent dune migration and growth. However, the effect of sand redistribution can be maximized by relocating the sand as close as possible to the crestline.

The installation of sand-trapping fences has also been used at the south dune of Jockey's Ridge. Repeat LiDAR surveys indicate that these fences have slowed the rate of migration and promoted an increase in the height of this dune (Mitasova *et al.*, 2005). In the model, the effect of sand-trapping fences was simulated by lowering the probability of entrainment to zero within a prescribed 'trapping' distance upwind and downwind from each fence. Sand can still be transported past the fence, but only by depositing sand until the angle of repose is achieved and subsequent transport occurs by avalanching. Figure 9(A) illustrates the dune field evolution following the installation of three fences placed 9 m apart along the crestline of the main dune complex with a trapping distance of 1.8 m for each fence. Figure 9(B) illustrates that the migration rate following fence installation decreased by 12%. Fences located upwind and downwind of the crestline had a progressively smaller effect on subsequent migration rates in the model. The magnitude of the relative decrease in migration rates depends on the number, spacing, and height (i.e. trapping distance) of the fences. Therefore, the 12% reduction in migration rates is only illustrative. The maximum height of the main dune height increases in these cases, but this effect is associated primarily with the buildup of sand in the immediate vicinity of the fences. The results in Figure 9(B) illustrate that fence installation has a greater effect on subsequent dune

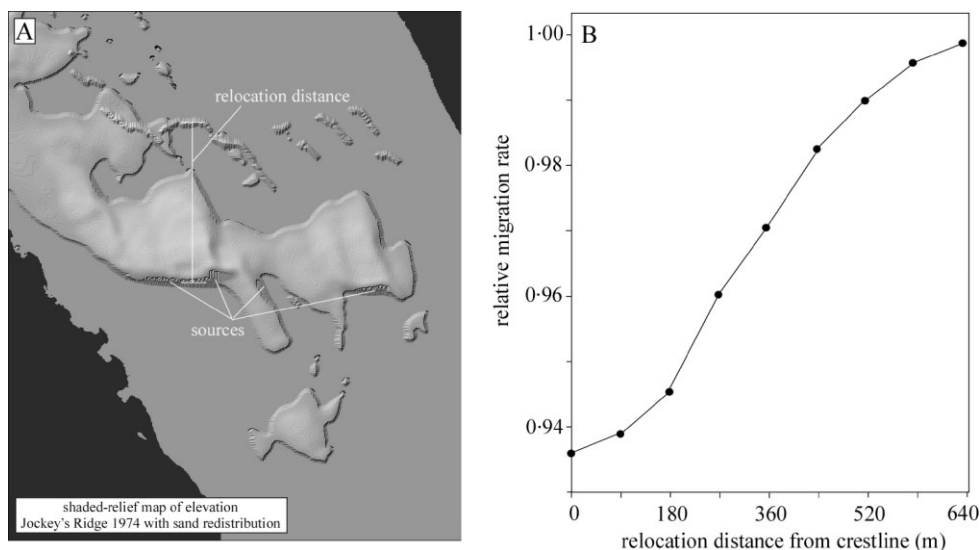


Figure 8. Illustration of the effect of sand redistribution on subsequent dune migration rates. (A) Shaded-relief map of elevations input into the model immediately following sand redistribution at $t = 0$. Sand was removed from slip faces and transported by a characteristic relocation distance upwind from the peak. (B) Plot of the relative migration rate following sand redistribution as a function of the relocation distance, illustrating that the greatest reduction in migration rates occurs for sand redistributed to the crestline.

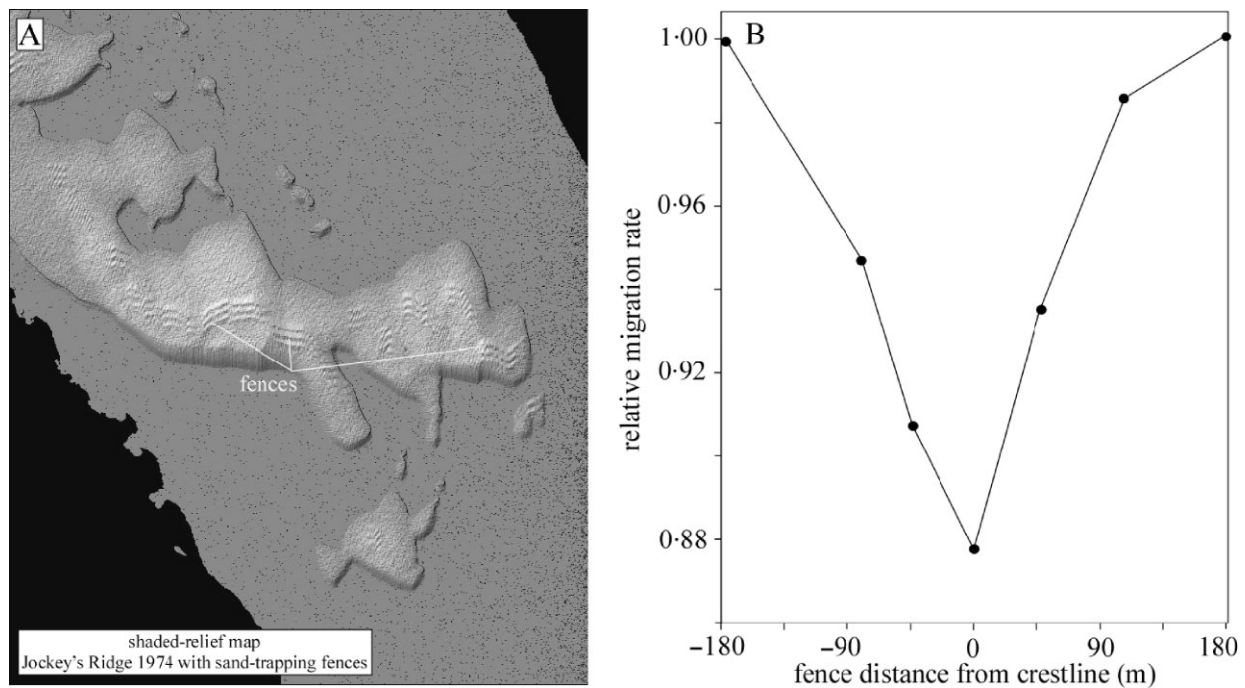


Figure 9. Illustration of the effect of fence installation on subsequent dune migration rates. (A) Shaded-relief map of elevations input into the model immediately following fence installation at $t = 0$ for the case with fences placed along the dune crestline. (B) Plot of the relative migration rate following fence installation as a function of the distance from the peak, illustrating that the optimal fence location is along the dune crestline.

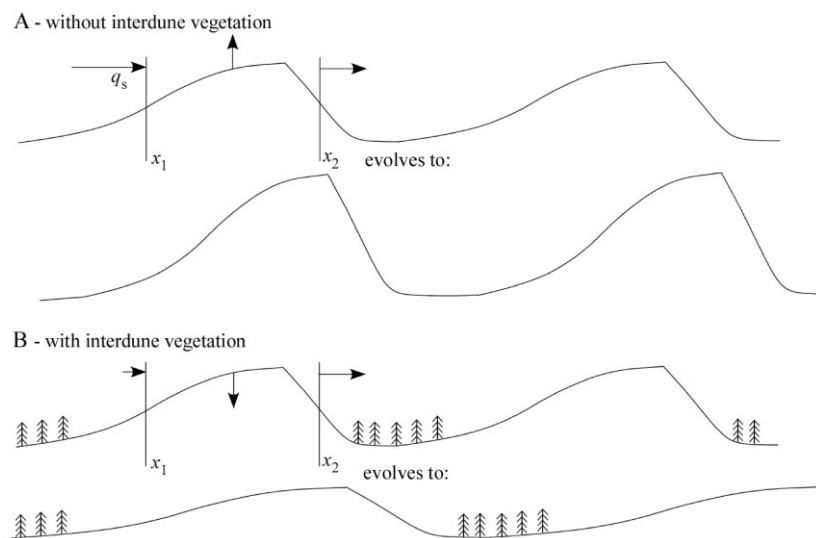


Figure 10. Schematic diagram of the conceptual model for the effect of interdune vegetation on dune evolution.

migration compared to the sand redistribution mitigation strategy.

Discussion

The relationship between dune growth/deflation and interdune vegetation illustrated in Figures 5 and 6 can be best understood using a conceptual model based on mass conservation principles. Consider Figure 10, which illustrates this conceptual model as it applies to dunes with and without interdune vegetation. In Figure 10(A), a dune segment is identified with upwind and downwind cross-sections located at x_1 and x_2 , respectively. Conservation of mass applied to that segment implies that any difference in the volumetric sediment flux entering the section from upwind and leaving the section downwind must be accompanied by a change in the average

elevation of the segment. Mathematically, conservation of mass along the sediment flux direction is quantified by Exner's equation, which states:

$$\frac{\Delta h}{\Delta t} = \frac{q_s(x_1) - q_s(x_2)}{x_2 - x_1} \quad (4)$$

where h is the average elevation of the segment between and x_1 and x_2 and q_s denotes the sediment flux. Equation 4 simply states that if the flux of sand is greater coming into the segment than the flux of sand leaving the segment, that difference must be stored within the segment, thereby causing aggradation. Conversely, if the flux of sand is greater leaving the segment than entering it, that difference must be supplied from sand within the segment, thereby causing surface lowering or denudation. In Figure 10(A), which represents the case with little or no interdune vegetation, the sediment flux

entering the top portion of the dune will be greater than the sand leaving the lee side of the dune by avalanching. In this case, conservation of mass implies that the dune must grow in height. Figure 10(B) illustrates the alternative end-member scenario with relatively dense interdune vegetation. In this case, sediment flux entering the top of the dune will be relatively low due to the stabilizing effect of interdune vegetation upwind. As a result, more sand will leave the dune downwind than will enter the dune from upwind. The result in this case is dune deflation. Conservation of mass also implies that as dunes grow in height they must decrease in area, assuming that the dune field remains constant in volume. Conversely, deflating dunes will spread out and increase in area. The decrease in dune height and increase in dune area predicted by this model is consistent with the recent dune evolution at Jockey's Ridge from 1974 to present documented by Mitasova *et al.* (2005).

Earlier studies concluded that dune deflation at Jockey's Ridge was the result of nearby source depletion. Runyan and Dolan (2001) argued that the original source for the Jockey's Ridge sand probably came from a 'deflation' area immediate northeast of the dune field. This hypothesis implies that conditions favorable to dune growth (i.e. a plentiful supply of sand from the northeast) was disrupted by land management practices beginning in the 1930s, especially the construction of a protective barrier dune along the shore, and further increased with urban development in the 1960s, resulting in significantly lower sand supply. The model results of this paper, however, in addition to the conceptual model illustrated in Figure 10, suggest that dune growth and deflation is primarily the result of the redistribution of sand between dunes and interdune areas. Indeed, from 1974 to the present, Mitasova *et al.* (2005) documented that the maximum dune height decreased by 40% (from approximately 35 to 25 m) and that dune area increased by 15% (from 4.5 to $5.3 \times 10^5 \text{ m}^2$), while the change in total volume of the dune field was less than 10%. If dune deflation were a direct result of lower sand supply, it is reasonable to expect that dune height and volume would change in similar proportions. The fact that dune height decreases in far greater proportion than the dune-field volume implies that deflation is not primarily a result of a diminishing sand supply. Rather, dune deflation is primarily the result of sand redistribution within the dune field from dunes to interdune areas.

The mass conservation framework illustrated in Figure 10 has additional implications for land management strategies. This framework implies that increased dune height can be promoted by any change that increases the difference between the rate of sand flux entering and leaving the top sections of dunes. For example, the installation of fences or vegetation at or near the dune crestline serves to lower the flux of sand leaving the dune while having relatively limited impact on the rate of sand entering the dune from upwind. The mass conservation framework implies that stabilizing the topmost portions of dunes using vegetation or sand-trapping fences is perhaps the single most effective strategy for promoting taller dunes and limiting dune advancement. However, this strategy has a negative impact on the dunes as natural landforms and is more suitable for lower sections of the dunes to prevent their migration outside the park. Sand redistribution, in contrast, has little lasting effect on the spatial distribution of sediment fluxes, and hence has a lesser effect on subsequent dune growth and migration rates. Taller dunes could also be formed by revegetating interdune areas, but this measure would likely increase the overall rate of dune migration because of the uniformly higher rates of transport in a landscape with no vegetation cover. Dune-field revegetation has been carried

out in the Netherlands as a management strategy, with the goal of enabling natural vegetative succession to occur in order to maximize species diversity, and, perhaps, minimize long-term dune migration. In such cases, sand 'drifts' analogous to the growing dunes in Figures 5(B) and 5(C) have developed over the short term, resulting in landscape destabilization and rapid dune migration in previously stabilized dune-field areas (van der Hagen *et al.*, 2008).

The Outer Banks of North Carolina are subject to intense hurricanes, and future research to quantify the impact of hurricanes specifically is needed. Hurricanes in this area generate both more intense winds and a shift from northerly to southerly winds. The effects of hurricanes are not captured by the LiDAR data of Mitasova *et al.* (2005) precisely, because immediate before and after surveys are not available, but data suggests that hurricanes flatten the dunes. The geomorphic effectiveness of these events is limited due to the significant rainfall that occurs during hurricanes. Northerly winds without rainfall have a much more significant impact (Havholm *et al.*, 2004). Mitasova *et al.* (2005) identified all major hurricanes and attempted to identify changes in evolution pattern or morphology. They found little evidence of major long-term impact, however; dunes generally flatten after hurricanes but rebuild relatively soon thereafter.

The model of this paper is limited and several caveats should be noted. First, a steady single wind direction was used representing winds that, on average, showed the most impact due to their frequency and intensity (Havholm *et al.*, 2004). In reality, the prevailing winds from March through August are from the southwest [9.9–12.8 miles per hour (m.p.h.)] while those from September through February are slightly stronger and from the northeast (10.8–13.4 m.p.h.). There are anecdotal observations of dunes shifting back and forth in north–south direction as a result of this change in wind direction. Nevertheless, the long-term data presented by Mitasova *et al.* (2005) as well as the unpublished 2007 and 2008 data show steady southerly migration. Seasonal data would be needed to confirm quantitatively the impact of changing wind direction. Single storm effects can be simulated by using the wind direction and intensity for the modeled storm as well as adjusting the entrainment probability function to the state of vegetation during the storm (depending on seasons and previous weather patterns). Second, the relationship between surface roughness and elevation (Figure 4) represents an average for the study area. Some areas of low elevation within the dune field, however, have lower vegetation density than others. In these areas of lower-than-average vegetation density the model will underpredict the rate of dune activity downwind because the model is based on a study-area-wide average vegetation–elevation relationship. It should be noted that interdune areas within the Jockey's Ridge dune field are also ephemerally influenced by ponded water (Mitasova *et al.*, 2005). Ponds can trap sand during wet periods and later act as local sources of sand during dry periods. The limitations of the model are most apparent when comparing the observed evolution of the south dune from 1974 to 1999. This dune evolved from a dome-shaped dune to a classic parabolic dune over this period. The model with elevation-dependent entrainment reproduces the basic parabolic character of this dune but does not reproduce the detailed shape or relative migration rate. Additional model complexity, including spatially-explicit vegetation growth/decay and a variable sand transport rate and direction (e.g. to represent the episodic nature of transport during hurricanes), would be needed to refine the model behavior and better understand the short-term evolution of this dune field.

Despite these caveats, the methods used in this paper may help to unravel the complex forcing mechanisms of recent

dune field evolution in both coastal and inland dune systems. There is abundant evidence for the role of vegetation changes in controlling the evolution of dune fields on the Israeli coast (Tsoar and Blumberg, 2002), southern Africa (Bullard *et al.*, 1997), and in Canada (Hugenholtz *et al.*, 2008), for example. In particular, the dunes studied by Tsoar and Blumberg (2002) have undergone a change from predominantly barchan and transverse dunes to parabolic dunes during a shift from relatively low to high vegetation density in the latter half of the twentieth century that closely mirrors the evolution at Jockey's Ridge. One key difference, however, between the Israeli and Jockey's Ridge cases is that the switch from barchan to parabolic dunes in the Israeli case was due to an increase in vegetation on the crests while at Jockey's Ridge it was due to an increase in interdune vegetation. In the Israeli case, vegetation growth on the crest led to an increase in the peak dune elevation, consistent with the conceptual model illustrated in Figure 10. Further work is needed to identify the range of conditions under which dunes may shift from barchan to parabolic types and from growing to deflating dunes.

For applications of the model to other dune fields, the relationship between surface roughness and elevation (Equation 2) must be derived based on the local data although the general assumption that roughness decreases with elevation is likely to be applicable to many other dune fields. Soil moisture reduces sand transport and supports vegetation growth, and its effect could be incorporated into the model as a control on entrainment using a similar function as Equation 2. However, soil moisture data are more temporally variable and harder to derive from remote sensing or on-ground measurements than vegetation cover. The model could also be used to simulate scenarios of increased drought and desertification as well as impact of increased rainfall sea level rise (increased wetness) leading to increased vegetation and dune stabilization by modification of the entrainment probability function.

Conclusions

Numerical modeling of dune evolution has advanced greatly in the past decade, primarily in response to the development of Werner's (1995) model. Here we modified Werner's model to account for the stabilizing effect of vegetation in dune fields in which there is a systematic relationship between vegetation density and elevation. We applied this model to the dune field at Jockey's Ridge, North Carolina, in order to better understand the trends in dune field evolution with and without interdune vegetation. The model illustrates the strong control that interdune vegetation can exert on dune field morphology and evolution. In the absence of interdune vegetation, dunes evolve towards closely-spaced, barchanoid dunes that increase in height and decrease in area through time, with smaller dunes migrating faster than larger dunes. The presence of interdune vegetation causes dunes to evolve towards more widely-spaced, parabolic dunes that decrease in height and increase in area through time, with small and large dunes migrating at roughly comparable rates. The recent evolution of dunes at Jockey's Ridge can best be understood within a mass-conservative framework that links local fluxes to vegetation density and the rate of change of surface elevation to the spatial variation in those fluxes. Finally, numerical modeling of alternative mitigation strategies underlines the effectiveness of introducing roughness elements (i.e. vegetation or fences) near the dune crestline; however, this strategy conflicts with the mission of the state park to conserve its natural features and is thus limited to the borders of the park. Although the model has been developed using the data

from the Jockey's Ridge state park the model can be applied to coastal dunes evolving under similar conditions in different regions of the world. Modifications in the equation for entrainment probability function can be used to simulate impacts of increased subsurface water levels, sea water level rise or extended drought and change in vegetation.

Acknowledgements—The authors wish to thank reviewers Chris Hugenholtz and Karen Havholm for helpful reviews that greatly improved the paper. We also wish to thank chief editor Stuart Lane and the associate editor for additional helpful suggestions.

References

- Baas ACW. 2007. Complex systems in aeolian geomorphology. *Geomorphology* **91**: 311–331.
- Baas ACW, Nield JM. 2007. Modeling vegetated dune landscapes. *Geophysical Research Letters* **34**: L06405. DOI: 10.1029/2006GL029152
- Bagnold RA. 1941. *The Physics of Blown Sand and Desert Dunes*. Methuen: London.
- Birkemeier W, Dolan R, Fisher N. 1984. The evolution of a barrier island: 1930–1980. *Shore and Beach* **52**: 2–12.
- Bullard JE, Thomas DSG, Livingstone I, Wiggs GFS. 1997. Dunefield activity and interactions with climatic variability in the southwest Kalahari Desert. *Earth Surface Processes and Landforms* **22**: 165–174.
- Cobb C. 1906. Where the wind does the work. *National Geographic Magazine* **17**: 310–317.
- Duran O, Herrmann HJ. 2006. Vegetation against dune mobility. *Physical Review Letters* **97**: L188001. DOI: 10.1103/PhysRevLett.97.188001
- Havholm KG, Ames DV, Whittecar GR, Wenell BA, Riggs SR, Jol HM, Berger GW, Holmes MA. 2004. Stratigraphy of back-barrier coastal dunes, northern North Carolina and southern Virginia. *Journal of Coastal Research* **20**: 980–999.
- Hugenholtz CH, Wolfe SA. 2005. Biogeomorphic model of dunefield activation and stabilization on the northern Great Plains. *Geomorphology* **70**: 53–70.
- Hugenholtz CH, Wolfe SA, Moorman BJ. 2008. Effects of sand supply on the morphodynamics and stratigraphy of active parabolic dunes, Bigstick Sand Hills, southwestern Saskatchewan. *Canadian Journal of Earth Sciences* **45**: 321–335.
- Lancaster N, Baas ACW. 1998. Influence of vegetation cover on sand transport by wind: field studies at Owens Lake, California. *Earth Surface Processes and Landforms* **23**: 69–82.
- Mitasova H, Overton M, Harmon RS. 2005. Geospatial analysis of a coastal sand dune field evolution: Jockey's Ridge, North Carolina. *Geomorphology* **72**: 204–221.
- Onishi N. 2006. In the shrinking dunes, stalking a creepy green enemy. *The New York Times*, 23 August. <http://travel2nytimes.com/2006/08/23/world/asia/23japan.html> [accessed 1 October 2008].
- Rebello LP, Brito PO, Monteiro JH. 2002. Monitoring the Cresmina dune evolution (Portugal) using differential GPS. *Journal of Coastal Research* **18**: 591–604.
- Runyan KB, Dolan R. 2001. Origin of Jockey's Ridge, North Carolina: the end of the highest sand dune on the Atlantic Coast? *Shore and Beach* **69**: 29–32.
- Sarre R. 1989. The morphological significance of vegetation and relief on coastal foredune processes. *Zeitschrift für Geomorphologie Supplementband* **73**: 17–31.
- Tsoar H, Blumberg DG. 2002. Formation of parabolic dunes from barchan and transverse dunes along Israel's Mediterranean coast. *Earth Surface Processes and Landforms* **27**: 1147–1161.
- Van der Hagen HGJM, Geelen LHWT, de Vries CN. 2008. Dune slack restoration in Dutch mainland coastal dunes. *Journal for Nature Conservation* **16**: 1–11.
- Werner BT. 1995. Eolian dunes: computer simulations and attractor interpretation. *Geology* **23**: 1107–1110.
- Wilson IG. 1972. Aeolian bedforms: their development and origins. *Sedimentology* **19**: 173–210.